Modeling the spatio-temporal evolution of fracture networks and fluid-rock interactions in GPU: Applications to lithospheric geodynamics

Dissertation

zur

Erlangung des Doktorgrades (Dr. rer. nat.)

der

Mathematisch-Naturwissenschaftlichen Fakultät

der

Rheinischen Friedrich-Wilhelms-Universität Bonn

vorgelegt von

Boris Galvan

aus

Panama Stadt, Republik Panama

Bonn 2012

Angefertigt mit Genehmigung der Mathematisch-Naturwissenschaftlichen Fakultät
der Rheinischen Friedrich-Wilhelms-Universität Bonn
am Steinmann-Institut für Geologie, Mineralogie und Paläontologie

1. Referent: Prof. Dr. Stephen A. Miller
2. Referent: Prof. Dr. Andreas Kemna

Tag der Promotion:
Erscheinungsjahr: 2013

Diese Dissertation ist auf dem Hochschulschriftenserver der ULB Bonn
http://hss.ulb.uni-bonn.de/diss_online elektronisch publiziert.

Contents

Abstract **1**

I INTRODUCTION **5**

Introduction **7**

1 Introduction **7**
1.1 Theoretical Background 11
1.1.1 Poro-elasto-plastic Model 11
1.2 Graphical Processing Units (GPUs) in Scientific Numerical Modeling 16
1.2.1 GPU implementation of Poro-elasto-plastic Media 16
1.2.2 GPU Architecture and Programing 19
1.3 Summary of the Scientific Articles 21
1.3.1 A full GPU simulation of evolving fracture networks in a heterogeneous poro-elasto-plastic medium with effective-stress-dependent permeability 21
1.3.2 GPU numerical reproduction of hydrofracture experiments in Poro-elasto-plastic material 21
1.3.3 Simulation of fluid induced seismicity accelerated in GPU. Application to Enhance Geothermal Systems 21
1.3.4 A poro-elasto-plastic model to simulate earthquake-volcano interaction dynamics in Central Chile 22

II PAPERS **23**

Paper I **25**

2 A full GPU simulation of evolving fracture networks in a heterogeneous poro-elasto-plastic medium with effective-stress-dependent permeability **25**
2.1 Abstract 25
2.2 Introduction 26
2.3 Model equations 27
2.3.1 GPU implementation 28

2.3.1.1 GPU nonlinear diffusion implementation 30
2.3.1.2 GPU elasto-plasticity implementation 30
2.4 Results 32
2.4.1 Nonlinear diffusion benchmark 32
2.4.2 Elasto-plastic benchmark 32
2.4.3 Poro-elasto-plastic modeling 33
2.5 Conclusions 37
2.6 Acknowledgments 39

Paper II **40**

3 GPU numerical reproduction of hydrofracture experiments in Poro-elasto-plastic material **41**
3.1 Abstract 41
3.2 Introduction 41
3.3 Theoretical Model 43
3.4 GPU implementation 44
3.5 Numerical Model of Hydrofracturing in Triaxial Experiments 45
3.6 Results and Discussion 46
3.7 Conclusions 48
3.8 Acknowledgments 52

Paper III **53**

4 Simulation of fluid induced seismicity accelerated in GPU. Application to Enhance Geothermal Systems **53**
4.1 Abstract 53
4.2 Introduction 53
4.3 Poro-elasto-plastic model 56
4.4 GPU implementation 57
4.5 Fluid injection in heterogeneous fractured rock 58
4.6 Modeling the Deep Heat Mining Project in Basel 60
4.7 Discussion and Conclusion 65
4.8 Acknowledgments 65

Paper IV **66**

5 A poro-elasto-plastic model to simulate earthquake-volcano interaction dynamics in Central Chile **67**
5.1 Abstract 67
5.2 Introduction 67
5.3 Geodynamic setting 69
5.4 Two-dimensional model 69
5.4.1 Conceptual model 69
5.4.2 Numerical model 71
5.5 Conclusions 78

5.6 Acknowledgments 78

III CONCLUDING REMARKS 79

Conclusions 81

6 Concluding Remarks and Future Work 81

List of Figures 98

List of Tables and Listings 105

Acknowledgments 107

Abstract

In this thesis, I present the theory and modeling of poro-elasto-plastic rheology coupled to a non-linear diffusion equation with a step increase in permeability at the onset of slip. This theoretical model is implemented in the graphic processing unit (GPU) architecture and programmed using the nVidia CUDA programming language. The numerical models are benchmarked by investigating fracture orientation for the solid-mechanical aspects, and by using the Method of Manufactured solutions for the diffusion part.

I find that the GPU platform is ideal for these models because very high resolution simulations can be performed on an explicit finite difference algorithm using a single GPU card, outperforming CPU by a factor of at least five. The inherent problem with these coupled systems is the wide range of time and length scales that needs to be considered, and the advantage of GPU is its inherent parallel architecture that allows to do so.

In these models, numerical fractures develop and evolve in response to prevailing far-field stresses, to local stress heterogeneity and pore-elastic stresses resulting from fracture growth, dislocation slip and fluid pressure diffusion within the domain.

The numerical models, once benchmarked, are used to understand a variety of important and diverse lithospherical geodynamical problems, including enhanced geothermal systems (EGS), volcano-tectonic interactions and aftershocks. Envisaged future applications include hydro-fracture ('Fracking'), CO_2 sequestration, earthquake nucleation and nuclear waste isolation.

The potential of this model is far-reaching, and future developments in 3 dimensions will open up countless new avenues of insight and understanding of fluid-rock interactions and lithospheric dynamics.

Zusammenfassung

In dieser Arbeit präsentiere ich die Theorie und die Modellierung von poro- elastisch-plastischer Rheologie gekoppelt mit einer nicht-linearen Diffusionsgleichung und mit einer schrittweisen Erhöhung der Permeabilität bei dem Auftreten eines Bruches. Dieses theoretische Modell ist implementiert mit der Technologie von graphischen Prozessor Einheiten (GPU) und programmiert in der nVidia CUDA Programmiersprache.

Das numerische Modell ist benchmarked mit der Untersuchung von Orientierungen von Brüchen für gesteinsmechanische Aspekte und unter Verwendung der Methode der "Manufactured solutions" für den diffusiven Anteil.

Ich denke, dass die GPU Plattform ideal für diese Modelle ist, da Lösungen mit sehr hoher Auflösung mit einem expliziten Finite Differenzen Algorithmus mit nur einer einzeln GPU Karte berechnet werden können und dabei CPU um den Faktor Fünf übertreffen.

Das inhärente Problem dieser gekoppelten Systeme ist die große Spannweite von Zeit- und Längenskalen, die analysiert werden müssen und der Vorteil von GPU ist die inhärente parallele Struktur, die dies ermöglicht.
In diesen Modellen entstehen und entwickeln sich Brüche in Antwort auf dominierende Fernfeld- Spannungen, lokale Spannungsheterogenität, poro- elastische Spannungen resultierend aus dem Bruchwachstum, Versetzungsstufen und der Diffusion von Fluiddruck.

Die numerischen Modelle werden, nach dem Benchmarking, verwendet um eine Vielzahl von wichtigen und verschiedenen lithosphärischen geodynamischen Problemen zu verstehen, zum Beispiel Enhanced Geothermal Systems (EGS), vulkanisch-tektonische Interaktion und Nachbeben. Vorstellbare zukünftige Anwendungen beinhalten Hydro- Fracturing ('Fracking'), CO_2 Sequestration, das Auslösen von Erdbeben und nukleare Endlagerung.

Das Potential dieses Modells ist weitreichend und zukünftige Entwicklungen in drei Dimensionen werden zahlreiche neue Einblicke und ein tieferes Verständnis von Fluid- Stein Interaktionen sowie der lithosphärischen Dynamik ermöglichen.

Part I

INTRODUCTION

Chapter 1

Introduction

The last 20 years of geophysical fluid dynamics has focused on mantle convection and solving the Navier-Stokes equations with increasing complexity of chemistry, viscosity, etc (Kaus et al., 2008; Gerya, 2011). Lithospheric geodynamics, usually treated as a thermal boundary layer, is controlled by fluid-rock interactions that are very difficult to simulate because of the large range of timescales involved, and the strong coupling between fracture creation and the concomitant changes in hydraulic and elastic properties. Modeling these processes is complicated, and few models exist that are fast, high-resolution and still include the dominant physics. Most codes to date are CPU-based, which requires expansive and expensive computational resources if high resolution simulations are required. The purpose of the research in this thesis was to develop a GPU-based code, with the goal of using this new computational platform for fast and high resolution simulations while allowing for accurate modeling of fluid-rock interaction in the lithosphere.

Fluid-rocks interaction play a key role in many different phenomena, for example, aquifers exploitation, fossil fuel reservoirs, geothermal energy, earthquakes and aftershocks triggering, dike intrusion, volcanic systems, mud volcanoes, CO_2 sequestration, etc. Although extensive research has been conducted in all these areas, there are still many questions to be answered. For example, although fluids are suspected to be an important part of earthquake dynamics and aftershocks sequences, the role of high pressure fluids is difficult to quantify because of a lack of models capable of simulating their importance.

The important players is real fluid-rock systems are stress, temperature, chemical compositions, phase transitions, and changes in the mechanical, hydraulic or electrical properties. Simplifications are always necessary while respecting the underlying physics are necessary to understand the problem under investigation.

This work centers in the fluid-rock interactions in the brittle field, i.e., time scales from microseconds to Millenia. Many earth processes that directly affect human activities occur over short timescales, but their evolution takes generations or more. A primary motivation of this thesis is understanding the influence of fluids on earthquakes, but the results of this thesis have application in other regimes of geody-

namics, including volcanic eruptions and geothermal systems.. This work present studies of different problems with different scales, in time and space, from laboratory triaxial experiments with time scales of minutes to aftershocks sequences modeling with duration of weeks and months, to volcanic systems with timescales of centuries.

We approach these problems using continuum mechanics, in particular, the poro-mechanics formulation. The combined behavior of rock infiltrated by water was initially studied for engineering applications, and Karl von Terzaghi was the first to analyze fluid saturated rocks from the point of view of poro-mechanics. He developed a one dimensional model of consolidation using a conceptual model of water-saturated soil grains forming an elastic porous skeleton(Terzaghi, 1923). This conceptualization proved to be useful for successfully predicting settlement of structures for many types of soils and set the basis for poro-mechanics.

Later, Maurice A. Biot generalize the theory to three dimensions. This theory became what is now known as poro-elasticity (Biot, 1941). The primary two mechanisms affecting porous media are increasing fluid pressure that causes the rock to dilate, and rock compression that causes the fluid pressure to rise if the fluid cannot drain. If the fluid pressures dissipate, the solid skeleton deforms. When part of the pressure exerted over the porous media is carried by the fluid, then undrained porous media is stiffer than a drained one. The Biot formulation was the first theory to be consistent with these observations.

If porous rock is subjected to further deformation, it yields and fractures. This irreversible deformation is called plasticity. Most natural rocks are porous and fractured. Fractures can be modeled using the porous media approach by changing the hydraulic and elastic properties in a localized way.

We model the complex mechanics of the fully couple poro-elasto-plastic media giving special attention to the initiation and evolution of fracture networks as they are created and propagate in response to the evolving stress field.
The physics involved in these processes are not amenable to analytical solutions, so numerical methods are necessary to study realistic problems.

There are many different code available to simulate rock-fluid interactions. For example, GEOCRACK is a 2D simulator of fluid flow through fracture media that couples deformation, fluid flow and heat flow. UDEC is 2D simulator that couples deformation and fluid flow, while ROCMAS is a 3D finite element simulator of two phase flow , poroelasticity and thermoelasticity (Rutqvist and Tsang, 2003). FRACture is a finite element poro-elastic, thermo-elastic simulator (Kohl et al., 1995), and GeoSys/Rockflow is a finite element 3D, multiphase flow, fracture flow, heat transport, chemical processes, poro-elastic, thermo-elastic and elasto-plastic simulator (Kolditz and Chen, 2005; Wang and Kolditz, 2007). MOTIF (Model Of Transport In Fractured porous media) is a 3D finite element thermomechanical-groundwater flow-heat flow simulator (Guvanasem and Chan, 1995), and FRANCON is finite

element based 3D simulator of thermo and poroelasticity. TOUGH-FLAC a heat flow-fluid flow-mechanical simulator with capabilities for elasto-plastic deformation (Rutqvist, 2011), and is widely used in the field. Beside these codes, there is a vast number of ad-hoc university programs available. However all these codes, although the degree of sophistication of many of them is quite advanced, lack of the necessary resolution or speed to deal with irregular evolutionary fracture networks.

Fracture networks are the primary fluid flow channels controlling the fluid pressure profile and which affect the overall stress state. It is clear that fracture networks could have a very complex geometry at different scales. In processes like fluid induced fracturing for geothermal applications, CO_2 sequestration or hydrofracturing ('fracking'), an accurate description of the network development and geometry is crucial. A realistic description of the evolving system could help reduce cost, maximize recovery, assess seismic hazard, and maximizes productivity and efficiency in the reservoir exploitation or storagevity of CO_2. For example, in exploitation of fossil fuel reservoirs, it is necessary to simulate the behavior of the reservoirs to estimate the best points to drill the extraction and injection wells. Currently this is done solving a flow equation in 3D and neglecting the deformation of the reservoir, which clearly will considerably change the state of the reservoir . This could lead to a poor usage or to more investment to drill more wells. In modeling CO_2 sequestration and geothermal systems, the poro-elasto-plastic equations are solved but no mechanism exists to simulate fracture creation and evolution, which is the essence of understanding these systems. The case of Enhanced Geothermal Systems (EGS) and fracking is of particular interest because the main point in these two new technologies is to create fracture networks, which by definition, evolve. Any prescribed fracture geometry at the start of the simulation is null and void once new fractures are formed.

Another important factor in fluid-rock interaction processes is the effect of fluid localization within the fractures. Gradients of fluid pressure introduce seepage forces that can promote further rock fracturing and the consequent extension of the network. When seepage forces are considered, the effect is that fluids can became a primary driving mechanism for earthquake nucleation and might also be important in earthquake-induced volcanic eruptions.

In this thesis, I develop a poro-elasto-plastic simulator that allows heterogeneities in all parameters of the system, nonlinearities in the model, high resolution simulations, and fracture network evolution and short computational times. This is accomplished using Graphical Processor Units (GPU) technology, which is the ideal platform for efficiently handling the complex physics driving the of the problem. This code is named *eFrackTurbo*, to emphasize that it is a very fast *e*volving *frac*tures simulator.

This thesis is organized in six chapters. First, we give a general introduction to the theoretical background, GPU programming and a summary of the scientific articles. In the second chapter, the poro-elasto-plastic media implementation in GPU is dis-

cussed and its application to aftershocks sequences is presented. The third chapter deals with hydrofracturing at laboratory scales, and how this model simulates at the grain-scale using a continuum code. I compare the results of the code to real laboratory hydrofracture experiments for calibration, and demonstrate that this code reproduces the essential aspects of the laboratory experiments. In Chapter 4, the model is applied to the real-world Deep Heat Mining project in Basel, Switzerland. Chapter 5 attempts to expand this model from the laboratory scale of Chapter 3 and the field scale of Chapter 4 to the tectonic scale of earthquake triggered volcanic eruptions. Chapter 6 presents conclusions of this thesis and suggests potential avenues for future study.

This thesis is organized as a series of papers to be submitted for publication in International Journals, so each Chapter is written as a self-contained article. The result of this format is some repetition of the Methods and Approach.

1.1 Theoretical Background

1.1.1 Poro-elasto-plastic Model

The evolution of the excess of fluid pressure is given by the equation of hydraulic diffusion. We follow a similar derivation as presented in (Wong et al., 1997). The continuity equation for fluid mass in a rigid solid skeleton is given by

$$\frac{\partial q_i}{\partial x_i} + \dot{m} = 0 \tag{1.1}$$

where q is the fluid mass flux and m is the fluid mass per unit volume of the porous medium. Fluid flux is related to pressure gradients through the Darcy's flow equations

$$q_i = \rho_o \frac{\kappa}{\eta} \frac{\partial P_f}{\partial x_i} \tag{1.2}$$

where κ is the permeability, ρ_o is the reference fluid density, η is the viscosity and P_f is the fluid pressure. The time evolution of the fluid mass is

$$\dot{m} = \rho_f \dot{\phi} + \phi \rho_f \beta_f d\dot{P}_f \tag{1.3}$$

with porosity ϕ and fluid compressibility $\beta_f = (1/\rho)(\partial\rho/\partial P_f)$. In a similar way, a pore compressibility can be defined as $\beta_\phi = (1/\rho_f)(\partial\phi/\partial P_f)$, using $\dot{\phi} = \phi\beta_\phi \dot{P}_f$ and introducing a plastic component of the porosity evolution $\phi_{plastic}$, equation 1.3 gives

$$\dot{m} = \rho_f \left(\phi(\beta_f + \beta_{phi}) d\dot{P}_f + \dot{\phi}_{plastic} \right). \tag{1.4}$$

Substituting 1.4 and the continuity equation 1.1 in the Darcy's flow equation 1.2 leads to

$$\frac{\partial P_f}{\partial t} = \frac{1}{\phi(\beta_f + \beta_\phi)} \left[\frac{\kappa}{\eta} \nabla^2 P_f + \dot{\Gamma}(P_f, T) \right] \tag{1.5}$$

where (P_f, T) is a source term that incorporates $\dfrac{\dot{\phi}_{plastic}}{\phi(\beta_f + \beta_\phi)}$.
Permeability in the crust can be approximated as a exponential function of the normal stress (Zhang et al., 1999; David et al., 1994). Different studies (Rice, 1992; Miller et al., 2004) shows that diffusion of fluid pore pressure in the crust can be modeled by the modified equation

$$\frac{\partial P_f}{\partial t} = \frac{1}{\phi(\beta_f + \beta_\phi)} \left[\nabla \frac{\kappa_o \cdot \exp\left(-\dfrac{\bar{\sigma_n}}{\sigma^*} \right)}{\eta} \nabla P_f + \dot{\Gamma}(P_f, T) \right] \tag{1.6}$$

where $\bar{\sigma_n}$ is the effective normal stress given by

$$\bar{\sigma_n} = \frac{\sigma_1 + \sigma_3 - 2(P_f + \varrho_f g z)}{2} + \frac{\sigma_1 - \sigma_3}{2} \cdot cos(2\theta) \tag{1.7}$$

and κ_o is the permeability at zero normal stress, σ^* is a constant related to the degree of fracturing of the rock and θ is the dip angle.
Equation 1.6 has been used to relate pore fluid pressure profiles to match aftershocks sequences in (Miller et al., 2004). Equation 1.6 is a reaction diffusion equation which might have very complex dynamical behavior. The σ^* parameter controls how step is the change of the permeability due to changes in normal stress. If σ^* is a lower value the difference between permeabilities for small changes in the normal stress is greater than with higher values of σ^*. Besides, the permeability could increase orders of magnitude due to failure (Mitchell and Faulkner, 2008; Zang et al., 1996). However, the effect of the normal stress dependency could "lock" fractures if the normal stress is higher, like in compressional environments. The source term in equation 1.6 could account for increase/decrease in the pore fluid pressure due compression/extension. In that case, it could be explicitly written introducing the volumetric stress change as in (Maillot et al., 1999). Another pore fluid pressure source could be dehydration due to heating of the rock. (Famin et al., 2008) reports of high amounts of CO^2 produced in just a few seconds for the magnitude M=7.9 Kobe earthquake in 1995. This process could be important in many other earthquake settings.

From linear theory of poro-elasto-plasticity, the full strain tensor is given as

$$\dot{\epsilon}_{ij} = \dot{\epsilon}^{pe}_{ij} + \dot{\epsilon}^{pl}_{ij} \tag{1.8}$$

where $\dot{\epsilon}^{el}_{ij}$ is the poro-elastic strain tensor and $\dot{\epsilon}^{pl}_{ij}$ is the plastic strain tensor.
The poro-elastic strain tensor is given by

$$\epsilon^{pe} = \frac{1}{2G}\sigma_{ij} - \frac{\nu}{2G(1+2\nu)} tr(\epsilon^{pe})\mathbf{I} - \frac{\alpha}{3K} P_f \mathbf{I} \tag{1.9}$$

where α is the Biot-Willis constant, G is the shear modulus, ν is Poisson's ratio and K is the porous medium bulk modulus. The equations for the poro-elastic stresses can be found inverting 1.9. In a compact form, the are

$$\sigma_{ij} = 2G\epsilon^{pe}_{ij} + 2G\epsilon^{pe}_{kk}\frac{\nu}{1-2\nu}\delta_{ij} + \alpha P_f \delta_{ij}. \tag{1.10}$$

It is clear that this equation is equal to the equation for the drained rock if an "effective stress" is defined as $\sigma_{ij} - \alpha P_f \delta_{ij}$, (Jaeger et al., 2007),(Detournay and Cheng, 1993). Then, the poro-elastic strains ϵ^{pe} can be computed from the usual elastodynamic equations in their velocity-stress formulation, replacing the total stresses by the "effective stresses"

$$\frac{\partial V_x}{\partial t} = \frac{1}{\rho}\left(\frac{\partial \sigma^{eff}_{xx}}{\partial x} + \frac{\partial \sigma_{xy}}{\partial y}\right) \tag{1.11}$$

$$\frac{\partial V_y}{\partial t} = \frac{1}{\rho}\left(\frac{\partial \sigma^{eff}_{yy}}{\partial y} + \frac{\partial \sigma_{xy}}{\partial x} + \rho g\right). \tag{1.12}$$

with μ and λ are the Lamé constants, ρ is the density, v_x and v_z is the velocity vector and σ_{xx}, σ_{zz}, τ_{xz} is the stress tensor. This results was first presented by Terzaghi

and states that in saturated porous rock, where the pores form a connected network, deformation is controlled by the effective stress

$$\sigma_{ij}^{eff} = \sigma_{ij} - P\delta_{ij}. \tag{1.13}$$

Plastic yielding can be visualize using the idea of two frictional surfaces in contact: sliding (yielding in this context) will occur only if the force parallel to the surface overtake the frictional resistance. In solid materials there is a second resistive factor called cohesion. This conceptualization is the base of the Mohr-Coulomb yield criteria which represent the shear failure of the material. A second failure mode is the tensile mode, described by the Griffith failure criteria. The yield function F ,that represents the closeness to failure, can be computed taking the maximum value between the Mohr-Coulomb and Griffith yield criteria

$$\begin{aligned} F_{tension} &= \tau - \sigma_m - \sigma_t & (1.14)\\ F_{shear} &= \tau - \sigma_m \cdot sin(\varphi) - C \cdot cos(\varphi) & (1.15)\\ F &= max(F_{tension}, F_{shear}). & (1.16) \end{aligned}$$

Here σ_t is the tensile strength of the rock, φ is the internal frictional angle, τ is the stress deviator and σ_m is the mean stress given as

$$\tau = \sqrt{\frac{1}{4}(\sigma_{xx} - \sigma_{yy}^2) + \sigma_{xy}} \tag{1.17}$$

$$\sigma_m = \frac{1}{2}(\sigma_{xx} + \sigma_{yy}) \tag{1.18}$$

for the planar stresses case.
The plastic strain rates are computed using the yield function

$$\dot{\epsilon}_{ij}^{pl} = 0 \text{ for } F < 0 \text{ or } F = 0 \text{ and } \dot{F} < 0 \tag{1.19}$$

$$\dot{\epsilon}_{ij}^{pl} = \lambda \frac{\partial q}{\partial \sigma_{ij}} \text{ for } F = 0 \text{ and } \dot{F} = 0. \tag{1.20}$$

Here q is the flow rule of the material, i.e. the way in which the material will deform in the plastic regime and λ is the so-called plastic multiplier. We use non-associative plastic flow rules (Vermeer and Borst, 1984)

$$\begin{aligned} q_{tension} &= \tau - \sigma_m & (1.21)\\ q_{shear} &= \tau - \sigma_m \cdot sin(\psi) & (1.22) \end{aligned}$$

where ψ is the dilatancy angle.
If we consider undrained porous materials, the effect of the fluid pressure is to shift the Mohr circle close to the failure envelop 1.1a. Then, undrained rocks could reach failure at lower stresses than drained rocks. Using the idealization of two contact frictional surfaces, it is clear that the fluid pressure push the surfaces apart, diminishing

the normal stress and promoting failure at lower stresses. When failure occurs in porous rocks, hydraulic parameters, mainly permeability, changes drastically (David et al., 1994; Zhang et al., 1999; Mitchell and Faulkner, 2008). This lead to localized pore-fluid pressure increase and seepage forces become significant,(Rozhko et al., 2007). Then, the combine effect of seepage forces and the pore-fluid pressure increase is to change the radius of the Mohr circle while shifting it near to the failure surface 1.1b. If nonlinear permeability is included, this effect is strong enough to create failure at lower pore-fluid pressures.

This mechanism is a principal factor in earthquakes triggering. It is known that the Earth crust is critically stressed and fluids can be in overpressurized pockets at depth. If these fluids are allow to scape, they will promote failure and failure creates fluid paths allowing further fluid mobilization which may trigger more failure. This might generate a self-sustained cycle of rock failure and fluid mobilization, an aftershock sequence.

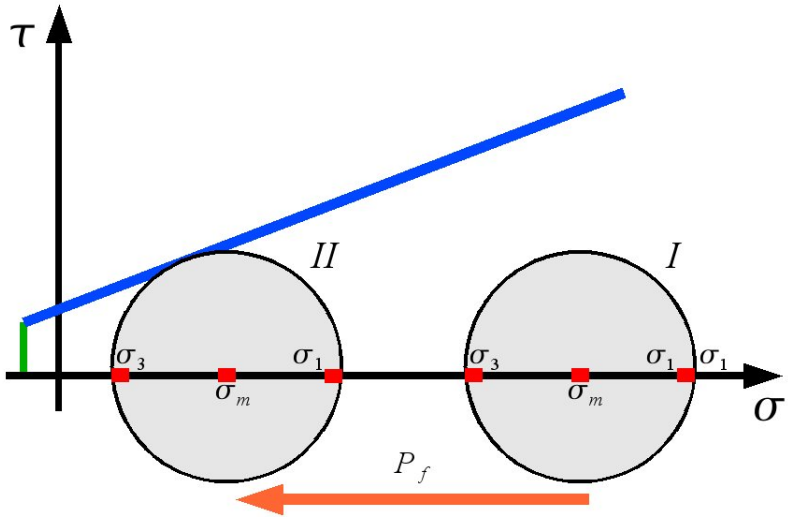

(a)

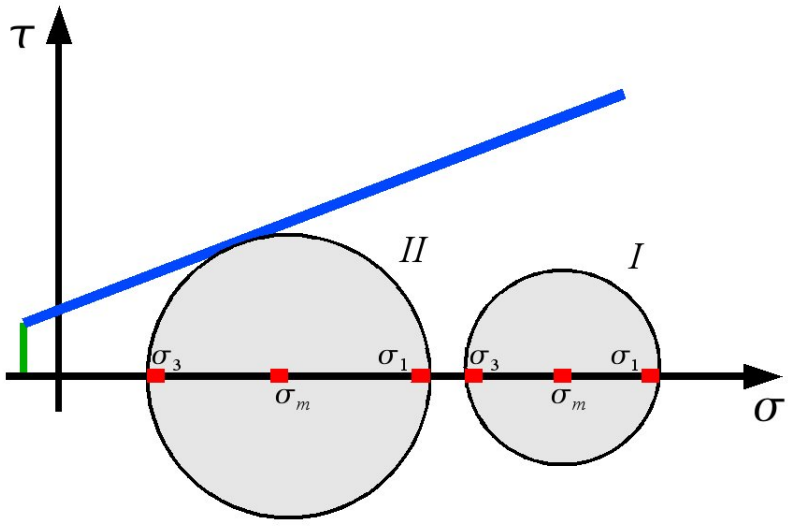

(b)

Figure 1.1: Mohr-Coulomb diagram. The blue line represent the Mohr-Coulomb failure envelop (shear failure). Green line is the Griffith cut off (tensile failure). (a) Homogeneous fluid pressure decreases the normal stress, moving the circle from initial position *I* to failure position *II*. (b) Localized pore fluid pressure changes the radius of the Mohr circle while shifting it near to the failure surface (position II). Lower pore fluid pressures might cause failure.

1.2 Graphical Processing Units (GPUs) in Scientific Numerical Modeling

1.2.1 GPU implementation of Poro-elasto-plastic Media

In nature, fracture networks are multiscale systems. Fractures lengths range from centimeters to kilometers long. Short fractures affects the background permeability of the rock, while large fractures, faults for example, work as main flow paths or flow channels. The correct simulation of the fracture porous media should cast different fracture length scales. This multiscality post problems from the point of view of numerical modeling. There are two main problems. First, the minimum fracture length in numerical models is given by the minimum length of the grid discretization, i.e. there is an "intrinsic fault length" introduced by the numerical resolution and not by the physics of the problem. All faults shorter than this "intrinsic fault length" are consider affecting only the background permeability. It is clear that the numerical resolution must be enough to resolve the minimum physical fractures length of the flow channels for the problem at hand. Second, if modeling of the fracture network evolution is intent, then the numerical grid must be able to follow the development of new fractures and their propagation. A way to overcome this difficulty, could be to increase the numerical resolution in a specific "interesting area" or to remesh when new fractures develop. In realistic modeling of fractured porous media, many factors controls the fracture development. To determine an specific "interesting area" is problematic because nonlocalize fractures might develop creating unattached networks. Under this circumstances, previous numerical zooming can not be accurately prescribed and constant remeshing is extremely computing expensive.

The approach that I use in this work is to fill the numerical domain with enough points to resolve fractures down to a minimum length, which is small enough compared to the global scale of the problem. By doing so, the model is able to follow the evolution of the fracture network in the whole domain at every iteration. The main drawback in this approach is the increment on the computation time. Implicit methods would require the inversion of very large matrices and heavy matricial operations that require long computational time. I solved the problem using explicit finite difference methods. Explicit methods has the advantage of being computationally light but time steps are very restrictive, increasing again the overall computation time. Parallel computation allows fast computation over large data sets. In particular Graphical Processor Units (GPU's) have become a paradigm in parallel computing during the last ten years.

The video games industry moves billions of dollars every year. Video games companies race to capture the favor of consumers introducing more realistic graphics to increase the reality feeling in their products. This requires better software and hardware to be able to manage the amount of information per frame and the high velocity frame rates. Real time, high resolution 3D graphics rendering, requires parallel intensive computation over large data sets. In order to deal with this, GPU's

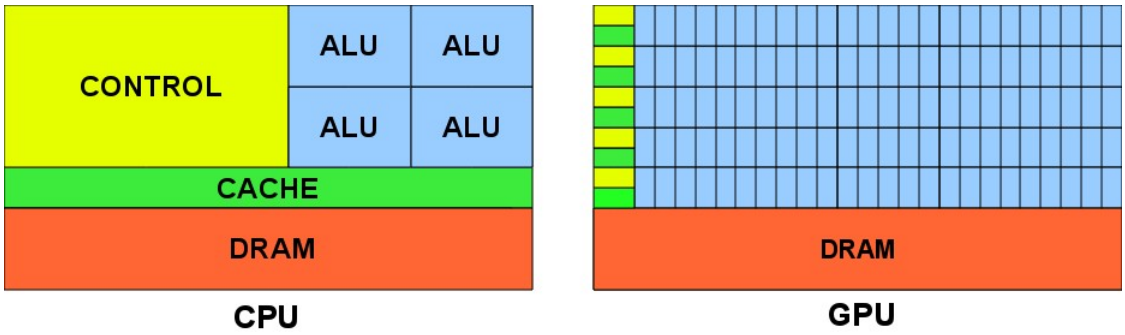

Figure 1.2: CPU architecture is designed for serial computations. For this reason it dedicates more chip space to flow control and memory operations. GPUS architecture gives priority to arithmetic intensive operations. Much more Arithmetic Logic Units (ALUs) are build in GPU chips.Cache memory for memory operations and flow control units are limited causing GPUs to be inefficient in comparison to CPUs for serial processes. From (NVIDIA, 2011).

architecture give more importance to data processing than to data catching or control flow. This is done by including many of so called *streaming processor cores*, that execute the same instruction stream in parallel. Therefore, just a limited flow control capacity is needed. Furthermore, *streaming processor cores* perform light weight arithmetic operations over the data in an intensive way, i.e., much more arithmetic operations are performed as memory operations, making necessary just a limited cached memory. Figure 1.2 presents a comparison of the CPU vs GPU architectures. Then, GPU's are well suited for problems that can be described in a parallel way in which single instructions operate over the whole data or large parts of the data.

The difference in the performance of GPU vs CPU during the last year has grown exponentially. The number of floating points operations (FLOPs) per second in a GPU is orders of magnitude higher than a CPU Figure 1.3. This difference will not decrease in the near future. Then, GPU's can be efficiently used to accelerate numerical applications if the most computing expensive parts of the code are processed on them while the memory management and control parts are executed using CPU's.

These capabilities were not overlook by the scientific community. Since its introduction in 1999, Graphics Processor Units (GPU) have been successfully applied to accelerate non-graphical computations. Its applicability was strongly limited by the complexity and limitations of the graphical programing languages available at the moment. The use of these languages, as OpenGl, to nongraphical purposes was a very difficult task. Nonetheless, some scientific applications were implemented.

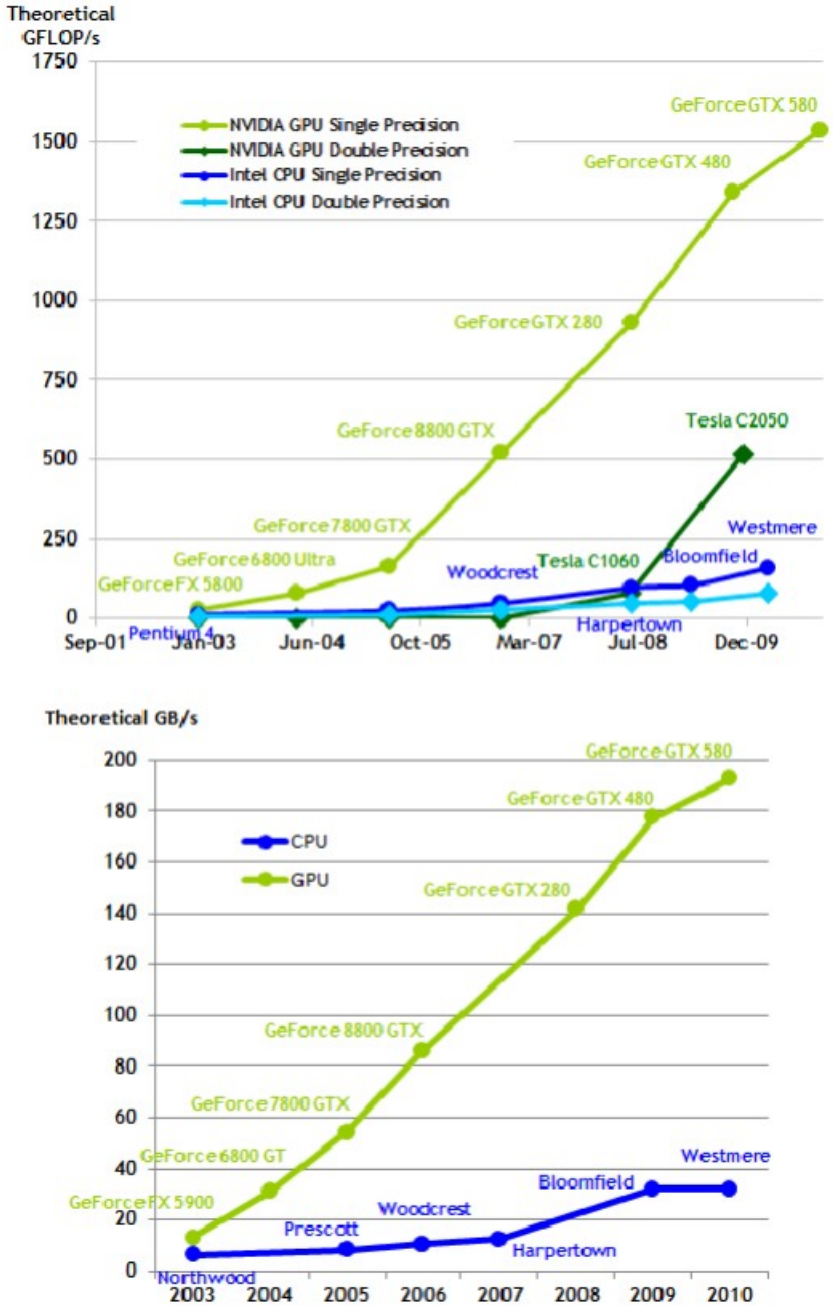

Figure 1.3: Comparison of the floating point operations (FLOPs) per second and memory band width for GPUs and CPUs. From (NVIDIA, 2011)

The NVIDIA company released at the end of 2006 the CUDA massive parallel architecture and programming language based in a C-like programming model that facilitates GPU usage in physical modeling, (NVIDIA, 2011). Since then, the amount and variety of GPU base scientific modeling has increase over the years (Griebel and Zaspel, 2010; Nageswarana et al., 2009; Sorensen and Mosegaard, 2006; Michéa and Komatitsch, 2010)).
The introduction of the CUDA architecture boosted the GPU usage for multipurpose computing. During the last years most of the computers in the top five of the list of the 500 fastest computers of the world are GPU based. GPU cluster present different advantages over CPU clusters: they are more energy efficients, they consume less electrical power and they require less cooling and they are smaller than CPU clusters.
It can be expected that in the near future, GPU based programing will be the main tool for high resolution real world scientific and general purpose computations.

1.2.2 GPU Architecture and Programing

GPU programs written with CUDA will run part of the code in the CPU and parts in the GPU. The CUDA functions that run in the GPU, called kernels, are executed as blocks of threads. Threads within the same block execute the same instructions. Every thread in a block has access to its own memory register and to a cached shared memory accessible by all threads of the block. Reading and writing of the shared memory is very fast. There is a non-cached global memory available to all threads, of the same block or not, but it access is very slow compared to shared memory. Registers, shared memory and global memory are read/write memories accessible by the GPU threads. Blocks are subdivided in groups of 32 threads called warps to be executed. Figure 1.4 shows a scheme of this. There are other read-only memories available to the threads: constant memory and texture memory. These are use to pass data from CPU to the GPU device.

CUDA programs controls data traffic between CPU and GPU. First, space in the GPU device memories is allocate. Then, data stored in the memory of the CPU, or host, is transfer to the GPU device read-only memories or the GPU global memory. The device operate on this data and save the results in global memory. The data stored in the global memory is passed to the host memory. Data within the device can be copied and operated using fast shared memory. This increases GPU efficiency. Finite differences methods are easy to parallelize in GPU's. We take advantage of this and implement the 2D poro-elasto-plastic media using shared and global memory. Due to the limitations of GPU's for flow control, plasticity implementation is not straightforward. We develop so called switch functions to implement plasticity in a GPU efficient way. Until this moment and at best of our knowledge, this is first poro-elasto-plastic rheology implementation in GPU's.

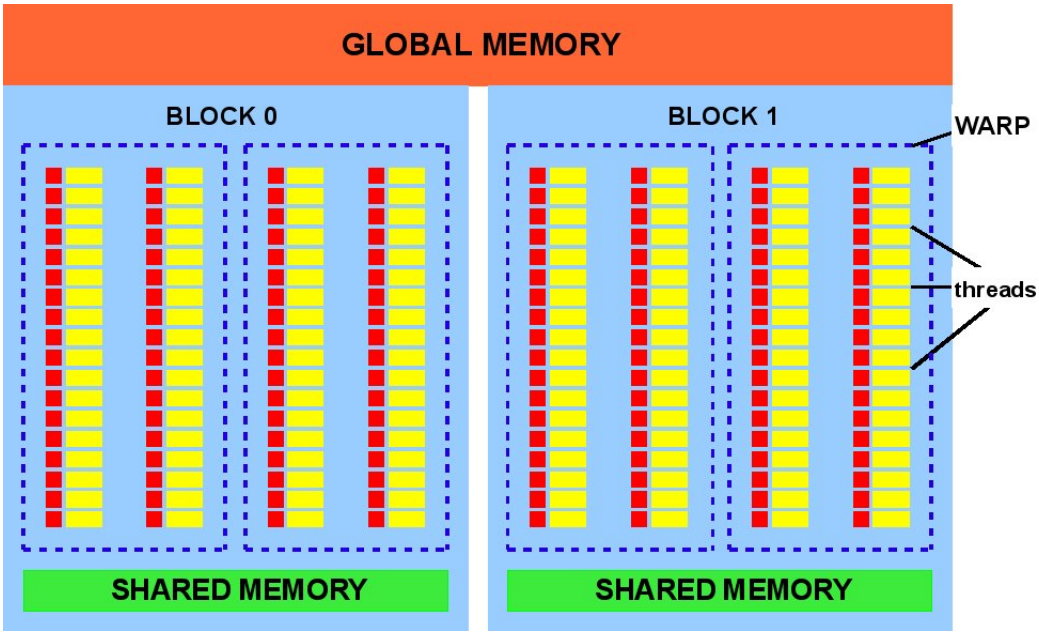

Figure 1.4: Every thread (yellow rectangles) has it own local (red squares). A warp is a set of 32 threads. All threads within a warp execute the same commands. Warp are grouped in Blocks. All threads of the same block have access to a common fast cached shared memory. All threads, independently of their block, have simultaneous access to global memory.

1.3 Summary of the Scientific Articles

In this section we present a resume of the three scientific articles produced during this work.

1.3.1 A full GPU simulation of evolving fracture networks in a heterogeneous poro-elasto-plastic medium with effective-stress-dependent permeability

In the first paper I introduce the equations of poro-elasto-plastic media and the numerical schemes used to solve them. Then, GPU programming is introduced and the different aspect for the poro-elasto-plastic media implementation in GPU are presented. The main problem arise in the plasticity implementation. GPU's have a very limited capacity to handle point by point operations and conditions. The plasticity computation requires to evaluate the yield function and apply the computation of plastic stresses for the specific points that fulfill the yield criteria. I develop so-called switch functions to handle the program branching. We present benchmarks of the different parts of the code. The nonlinear diffusion solver is benchmarked using the Method of Manufactured Solution (MMS) and is compared to a CPU implementation. Then the elasto-plastic solver benchmarks are presented. Finally, we apply the code to model fluid migration from a overpressurized layer at depth. Compressional and extensional cases are analyzed. Extensional environments enhance the fluid mobilization and consequent failure. The results of this paper shows that aftershocks sequences can be triggered and sustained due to fluid mobilization.

1.3.2 GPU numerical reproduction of hydrofracture experiments in Poro-elasto-plastic material

The main goal of this paper is to reproduce laboratory experiments of induced hydrofracturing in critically stressed rocks. Simulation of laboratory experiments of fluid infiltration in sandstone are used to calibrate the model. Using GPU technology we are able to model the system up to grain scales. It is shown that permeability plays and important role. We show an excellent correlation between model and experiment of the evolved fracture topology, as an indication that the model encompass the underlaying physics.

1.3.3 Simulation of fluid induced seismicity accelerated in GPU. Application to Enhance Geothermal Systems

In this paper, I focus in the effects of fluid injection in highly fractured rock in relation to Enhanced Geothermal Systems (EGS). I simulate a highly fractured rock matrix in the vicinity of the borehole. Results of the simulation show that the usual assumption of keeping fluid injection pressure below the minimum compressive stress is not an adequate constraint to restrict hydrofracturing. We show that high damage occurs far below this threshold.

1.3.4 A poro-elasto-plastic model to simulate earthquake-volcano interaction dynamics in Central Chile

Here I applied the poro-elasto-plastic model to investigate earthquake-volcanic interactions in the Central Chile volcanic arc. The influence of the inter-seismic and post-seismic regimes on the crust below the volcanic arc were modeled. It is shown that the static extensive stresses of the post-seismic regime encourage the upward mobilization of fluid through fractures. This process explains the time gap between earthquakes and volcanic erruptions.

Part II

PAPERS

Chapter 2

A full GPU simulation of evolving fracture networks in a heterogeneous poro-elasto-plastic medium with effective-stress-dependent permeability

2.1 Abstract

The wide range of timescales and underlying physics associated with simulating poro-elasto-plastic media present significant computational challenges. GPU technology is particularly advantageous to overcome these problems because even though the physics are the same, computational times are orders of magnitude faster. Poroelasticity could be implemented in GPU, however GPU implementation of plastic stresses pose problems because branching is introduced into the program and thus introduces efficiency penalties. In general, any element by element evaluation to deal with branching in GPU is very inefficient. In this paper, we describe fracture evolution in a poro-elasto-plastic medium and use a switch on- switch-off function to avoid branching, allowing efficient computation of plasticity in GPU. We benchmark for the elasto-plastic part by investigating the angles of developed shear bands, and benchmark the non-linear diffusion part of the code using the method of manufactured solutions. Model results are presented for fluid pressure propagation through an elasto-plastic matrix subjected to compression, and another for extension. The results demonstrate how fluid flow is restricted in the compression case because of the load-induced low permeability, while fluid flow is encouraged in the extensional case because of the extension-induced high permeability. Code performance is excellent in GPU, and we are able to runs months of simulation using time steps of a few seconds within a few hours. With this new algorithm, many problems of couple fluid flow and the mechanical response can be efficiently simulated at very high

resolution.

2.2 Introduction

Triggering of earthquakes by high pressure fluids is well documented in enhanced geothermal systems ((Häring et al., 2008),(Shapiro and Dinske, 2009),(Audin et al., 2002)) and natural environments ((Miller et al., 2004),(Bols and Nur, 2002),(Ohtake, 1974)). Injection of over-pressurized fluids into fault zones reduces the frictional resistance, thus lowering of the shear stress necessary to failure (Terzaghi, 1923; Nur, 1971). Documented cases of fluid-triggered or fluid-assisted earthquake sequences include the Mw=6.3 1997 Colfiorito (Miller et al., 2004) and Mw=6.3 L'Aquila (Terakawa et al., 2010) earthquake sequences in Italy, and the 2004 Mw=6.8 Niigata earthquake in Japan (Sibson, 2007). Observations of direct fluid generated by earthquake slip have been reported for the 1995 Mw=7.2 Kobe (Japan) earthquake (Famin et al., 2008) where large volumes of CO_2 were produced from temperature-induced decarbonization.

Although fluids and faulting have long been known to be an important part of the earthquake process, modeling the spatio-temporal evolution of such systems is computationally challenging primarily through the dynamical property of intrinsic permeability. Namely, permeability can change by orders of magnitude over short timescales because of the switch to high permeability at the onset of slip (Miller and Nur, 2000). Here we take a modeling approach that combines poro-elasto-plastic model of (Rozhko et al., 2007) with a non-linear diffusion model ((Rice, 1992; Miller et al., 2004)), where the non-linearity arises through an effective-stress dependence of the permeability. The solid deformation is modeled using the FLAC (Fast Lagrangian Analysis of Continua) algorithm with density scaling (Cundall, 1982), which is coupled to the non-linear diffusion model using an explicit finite difference algorithm with adaptive time-stepping.

In general, simulations over time scales of months (relevant for modeling fluid-driven aftershock sequences) takes many hours to days of computation time. Reducing the numerical resolution is the typical strategy to reduce the computational time, but in our case this would mean introducing unrealistically large intrinsic length scales for the fractures. More importantly, natural fracture networks occur over a wide range of size scales, from centimeters to kilometers, so reduced resolution is not an affordable sacrifice. The advantage of Graphics Processor Unit (GPU) technology is that it allows much faster computations due to its inherent parallel architecture, allowing much shorter computational times while also increasing numerical resolution. GPUs are particularly powerful for solving governing equations that can be formulated into explicit finite difference algorithms, like for example our full GPU poro-elasto-plastic model with adaptive time stepping discussed below.

2.3 Model equations

Different studies ((Rice, 1992),(Miller et al., 2004)) shows that diffusion of fluid pore pressure in the crust can be modeled using a nonlinear equation with permeability being an exponential function of stresses ((Zhang et al., 1999),(David et al., 1994)) of the form

$$\frac{\partial P_f}{\partial t} = \frac{1}{(\beta_f + \beta_\phi)} \nabla \left[\frac{\kappa_o \cdot \exp\left(-\frac{\bar{\sigma_n}}{\sigma^*}\right)}{\phi \cdot \eta} \nabla P_f + \dot{\Gamma}(P_f, T) \right] \tag{2.1}$$

where $\bar{\sigma_n}$ is the effective normal stress given by

$$\bar{\sigma_n} = \frac{\sigma_1 + \sigma_3 - 2(P_f + \varrho_f g z)}{2} + \frac{\sigma_1 - \sigma_3}{2} \cdot cos(2\theta) \tag{2.2}$$

and P_f is the fluid overpressure, κ_o is the permeability at zero normal stress, σ^* is a constant related to the degree of fracturing of the rock, ρ_f is the fluid density, η is the viscosity, ϕ is the porosity, β_f is the fluid compressibility, β_ϕ is the pore compressibility and $\dot{\Gamma}(P,T)$ is the source term.

The elastodynamic equations in their velocity-stress form describe the elastic response of the rock skeleton

$$\frac{\partial V_x}{\partial t} = \frac{1}{\rho}\left(\frac{\partial \sigma_{xx}^{eff}}{\partial x} + \frac{\partial \sigma_{xy}}{\partial y}\right) \tag{2.3}$$

$$\frac{\partial V_y}{\partial t} = \frac{1}{\rho}\left(\frac{\partial \sigma_{yy}^{eff}}{\partial y} + \frac{\partial \sigma_{xy}}{\partial x} + \rho g\right) \tag{2.4}$$

$$\frac{\partial \sigma_{xx}}{\partial t} = (\lambda + 2\mu)\frac{\partial V_x}{\partial x} + \lambda \frac{\partial V_y}{\partial y} \tag{2.5}$$

$$\frac{\partial \sigma_{yy}}{\partial t} = \lambda \frac{\partial V_x}{\partial x} + (\lambda + 2\mu)\frac{\partial V_y}{\partial y} \tag{2.6}$$

$$\frac{\partial \tau_{xy}}{\partial t} = \mu \left(\frac{\partial V_x}{\partial x} + \frac{\partial V_y}{\partial y}\right) \tag{2.7}$$

with μ and λ are the Lamé constants, ρ is the density, v_x and v_z is the velocity vector and σ_{xx}, σ_{zz}, τ_{xz} is the total stress tensor. In saturated porous rock, where the pores form a connected network, deformation is controlled by the Terzaghi effective stress

$$\sigma_{ij}^{eff} = \sigma_{ij} - P\delta_{ij}. \tag{2.8}$$

Plastic deformation of rocks is modeled using Mohr-Coulomb and Griffith criteria

$$F_{tension} = \tau - \sigma_m - \sigma_t \tag{2.9}$$

$$F_{shear} = \tau - \sigma_m \cdot sin(\varphi) - C \cdot cos(\varphi) \tag{2.10}$$

$$F = max(F_{tension}, F_{shear}) \tag{2.11}$$

where F is the yield function, φ is the internal frictional angle, τ is the stress deviator, σ_m is the mean stress, σ_t is the tensile strength of the rock. The plastic strain rates are given by

$$\dot{\epsilon}_{ij}^{pl} = 0 \text{ for } F < 0 \text{ or } F = 0 \text{ and } \dot{F} < 0 \tag{2.12}$$

$$\dot{\epsilon}_{ij}^{pl} = \lambda \frac{\partial q}{\partial \sigma_{ij}} \text{ for } F = 0 \text{ and } \dot{F} = 0. \tag{2.13}$$

We use non-associative plastic flow rules (Vermeer and Borst, 1984)

$$q_{tension} = \tau - \sigma_m \tag{2.14}$$

$$q_{shear} = \tau - \sigma_m \cdot sin(\psi). \tag{2.15}$$

In this report the dilatancy angle is $\psi = 0$. From linear theory of poroelasticity the full strain tensor is given by

$$\dot{\epsilon}_{ij} = \dot{\epsilon}_{ij}^{pe} + \dot{\epsilon}_{ij}^{pl} \tag{2.16}$$

where $\dot{\epsilon}_{ij}^{el}$ is the poroelastic strain tensor. The poroelastic stress tensor is given by

$$\sigma_{ij} = 2G\epsilon_{ij}^{pe} + 2G\epsilon_{kk}^{pe}\frac{\nu}{1-2\nu}\delta_{ij} + \alpha P_f \delta_{ij} \tag{2.17}$$

where α is the Biot-Willis constant, G is the shear modulus and ν is Poisson's ratio ((Jaeger et al., 2007),(Detournay and Cheng, 1993)).

2.3.1 GPU implementation

Since its introduction in 1999, Graphics Processor Units (GPU) have been successfully applied to accelerate non-graphical computations due to it highly parallel architecture. GPU implementations have been reported, to name a few, in fluid dynamics ((Griebel and Zaspel, 2010),(Zaspel and Griebel, 2011)), medical sciences ((Nageswarana et al., 2009),(Sorensen and Mosegaard, 2006)) , geophysics ((Michéa and Komatitsch, 2010),(Lastra et al., 2009)), quatum chemistry (Vogt et al., 2008), molecular dynamics (Yang et al., 2007) and biology (Stivala et al., 2010). The CUDA programming language, develop by NVIDIA and based in a C-like programming model, facilitates GPU usage in physical modeling, (NVIDIA, 2011).

GPU programs written with CUDA runs part of the code in the CPU and parts in the GPU. The CUDA functions that run in the GPU are called kernels. The CPU, also refered as "host" in GPU literature, handles the passage of the data to the GPU, called "device" in GPU literature. The host has access to different memories of the GPU as the global memory, texture memories and constant memory. From these memories the device can read the data and operate over it. The texture and constant memories are read only memories for the device. The global memory is read/write memory type for the host and the device. The device has a second fast cached memory called shared memory. The global memory is non-cached and, in consequence, slower. To increase the efficiency of a GPU code is preferable to use

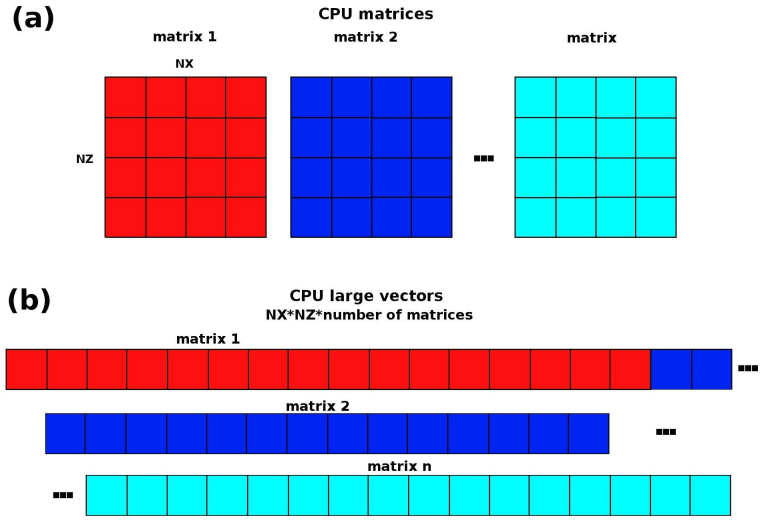

Figure 2.1: Initial data matrices (a) of size $nx \times nz$, are grouped together in large one dimensional vectors (b) of size *number of matrices* $\cdot nz \cdot nx$ to be passed to GPU.

shared memory for most of the computations. However , shared memory is very limited in GPUs. To overcome this problem, the initial matrix of dimension $nx \times nz$ saved in the global memory is subdivided in shared memory tessels and the device operate with them.
Kernels admit only a limited number of parameters. To avoid reaching this limit, the initial data matrices (stresses, velocities, rheological properties, hydraulic properties, etc.) of size $nx \times nz$, are grouped together into large one-dimensional vectors of size *number of matrices* $\cdot nz \cdot nx$ to be passed to GPU. To access correctly different data segments within the GPU matrices, we use the index expression:

$$index = x + z * nx + (position\ of\ the\ matrix\ in\ the\ large\ vector - 1) * nz * nx \quad (2.18)$$

where $x = 0$ to $nx - 1$ and $z = 0$ to $nz - 1$.
Figure 2.1 shows and sketch of this procedure.

We divide the problem in four main steps:

- solution of the nonlinear diffusion equation (2.17),
- computation of the effective stresses (2.8),
- solution of the velocities equations (3,4) and
- computation of the total stresses(5-7),
- evaluation of the yield function (2.9) and computation of plastic stresses using (2.12).

2.3.1.1 GPU nonlinear diffusion implementation

We use a first order in time, fourth order in space finite difference scheme to solve the nonlinear diffusion equation. Boundary conditions are zero flux boundary conditions at the left, right and bottom edges and Dirichlet boundary conditions at the top, $P_f = 0$.
We compute the solution of the nonlinear diffusion equation using shared memory for the center of the domain and global memory for the boundary conditions. Two kernels perform the computation of the nonlinear diffusion: *non_lin_diff* and *fluid_diff_write*. First, nonlinear permeability is computed using equation 2.2 and the new permeability is written to global and shared memories to be used in the equation 2.17. The inner part of the fluid pressure solution is computed using shared memory and the boundary conditions using global memory. The new fluid pressure profile solution is written to a new position on the large GPU global memory matrices. We call this vector P_{fnew}. If the program tries to write the result directly to the initial memory position, let us call it P_{finit}, errors appears due to the fact that GPU tries to read and write the same memory address at the same time. For that reason, a second kernel fluid_diff_write writes the solution back to the initial row vector P_{finit}. A pseudocode of the kernels *non_lin_diff* and *fluid_diff_write* is presented in algorithm tables 1 and 2.

Algorithm 1 *non_lin_diff*

Copy $P_{fold}, k_{fo}, \theta, \eta, \sigma^*$, ϕ,σ_{xx} and σ_{zz} on shared memory
Use shared memory variables to compute k_f and save in global memory
Save new value of k_f in shared memory
Use shared memory variables to compute P_{fnew} for the center of the domain and save in global memory
Compute P_{fnew} at the boundaries using global memory

Algorithm 2 *fluid_diff_write*

Copy P_{fnew} in global memory to P_{fold} in global memory

At the end of every iteration, porosity, σ^*, bulk modulus and Poisson's ratio are updated to be used in the next time step. The drained values of the rheological properties (bulk modulus, Poisson ratio) are taken if P_f = hydrostatic, and undrained values for P_f = maximum overpressure. For intermediate values of P_f, we use a linear function to update rheological properties. The same procedure is used to update porosity and σ^*: porosity is maximum and σ^* is minimum if P_f is maximum and porosity is minimum and σ^* maximum if P_f equal to hydrostatic.

2.3.1.2 GPU elasto-plasticity implementation

Solutions of elasto-dynamic equations using standard staggered grids introduce instabilities when the domain contains heterogeneities, e.g. cracks, density or rheol-

ogy changes. To overcome this we use a staggered grid scheme with centered cells. Stresses were located in the cell centers and velocities on its corners. In the program, stresses have a size $(nx+1)*(nz+1)$ and velocities $nx*nz$. However, all matrices are rearranged in the GPU to have size $(nx+1)*(nz+1)$ by filling extra positions with zeros. Boundary conditions for stresses are zero slip at the right, left and bottom edges and free surface boundary condition at the top. Velocity boundary conditions are $v_x = V$ and $v_z = 0$ at the right edge, $v_x = -V$ and $v_z = 0$ at the left edge and $v_z = 0$ at the bottom.
The kernel *effective_stresses* computes equation 2.8. As in the case of the diffusion, the central part of the effective stress matrices is computed using shared memory and boundary conditions using global memory. Table 3 present the pseudocode of this kernel. Velocities are computed in the kernel *velocity_computation* using the

Algorithm 3 *effective_stresses*

Copy P_{fnew}, σ_{zz} and σ_{xx} on shared memory
Perform equation (2.3) using shared memory variables and save results on global memory
Apply boundary conditions using global memory

same procedure. Table 4 shows the pseudocode for this kernel.
Elastic and plastic stresses are computed in the kernel *elasto_plasticity_computation*.

Algorithm 4 *velocity_computation*

Copy effective stresses σ_{zz}^{eff}, σ_{xx}^{eff}, σ_{xz}^{eff}, velocities v_x, v_z and displacements U_x, U_z on shared memory
Compute equations 2.8 for the central part of the effective stresses matrices using shared memory variables and save results on global memory
Apply boundary conditions using global memory

Plastic stresses are applied in the specific points where failure conditions 2.12 are fulfilled. This step introduces program branching, which is a major problem for the GPU implementation. CPU can easily perform an element by element search and testing using the if or else logical controllers. Although GPU can compile these logical controllers, program branching introduces a performance penalty due to its inherent parallel architecture. In NVIDIA GPUs, threads within a block are grouped in 32 elements called warps. Within a warp, all threads perform the same instruction at the same time. If warp divergence occurs some threads will take one branch and others the other branch. The first threads to finish the computation must wait until all threads from all different branches finish their computations, thus significantly decreasing the overall performance. In general, GPU will be much slower than CPU when performing element by element operations.
There are different techniques to deal with branching in GPU (Harris and Buck, 2005), and we developed a new and easy technique, called switch functions, to handle GPU branching. The details of this implementation will be presented in future communications.

2.4 Results

2.4.1 Nonlinear diffusion benchmark

The nonlinear diffusion algorithm was benchmarked using the *Method of Manufactured Solutions* (MMS),(Salari and Knupp, 2000). The MMS has been applied to different problems of computational fluid dynamics ((Bond et al., 2004),(Roy et al., 2004),(Shunn and Ham, 2007)). In this method, an artificial solution G is proposed. This solution does not need to be physically meaningful, but it must be smooth enough to be differentiable within the domain at the higher order of the differential equation. The function G must not be a trivial solution of the differential equation and it must be complicated enough to test the accuracy of the numerical solution. A symbolic calculus software is used to differentiate the manufactured solution and this result is compared to the numerical solution.
The manufactured solution function is:

$$P_f = \exp\left(-\left(\frac{(x-a)^2}{b}+\frac{(z-a)^2}{b}\right)\right) \tag{2.19}$$

$$k_{fo} = (0.1 - 1^{-2}\cdot z)\cdot \exp\left(-\frac{0.5\left(\sigma_{xx}+\sigma_{zz}-2\cdot P_f\right)+0.5\left(\sigma_{xx}-\sigma_{zz}\right)cos\left(2\cdot\theta\right)}{\sigma^*}\right) \tag{2.20}$$

with $a = 5$, $b = 25$, $\sigma_{xx} = \sigma_{zz} = 10\cdot z$, $\sigma^* = 20$ and $\theta = 60$ and the domain of the function is $\Omega = x \times z$ for $x = [0, 10]$ and $z = [0, 10]$. These two functions are smooth and their derivatives are continuous over this domain. We use the MATLAB symbolic calculus toolbox to compute the derivatives. We evaluate the equation

$$\nabla\frac{\kappa_o\cdot\exp\left(-\frac{\bar{\sigma_n}}{\sigma^*}\right)}{\eta} = \mathrm{RHS} \tag{2.21}$$

with $\eta = 1$, using the MATLAB symbolic calculus toolbox a CPU implementation and the GPU implementation. The L_2 norm measures the global error between the analytical, MATLAB symbolic solution, and numerical RHS . For all computational experiments grid points in X direction where equaled to grid points in Z, i.e. $n = nx = nz$. Grid points number per axis n was varied from 100 to 2000. Figure 2.2 shows the results. Both implementations, CPU and GPU, converge to the analytical solution in the same way when the numerical resolution is increased.

2.4.2 Elasto-plastic benchmark

Elasto-plastic model benching is done by checking the formation of localized shear zones, shear bands, with the correct angle. There are three different theories that describe the orientation of the shear bands: Coulomb, Roscoe and Arthur ((Arthur et al., 1977),(Bardet, 1990)). For a material with frictional angle φ and dilation angle ψ, shear bands form with dip angles θ between Rosco-Coulomb range,

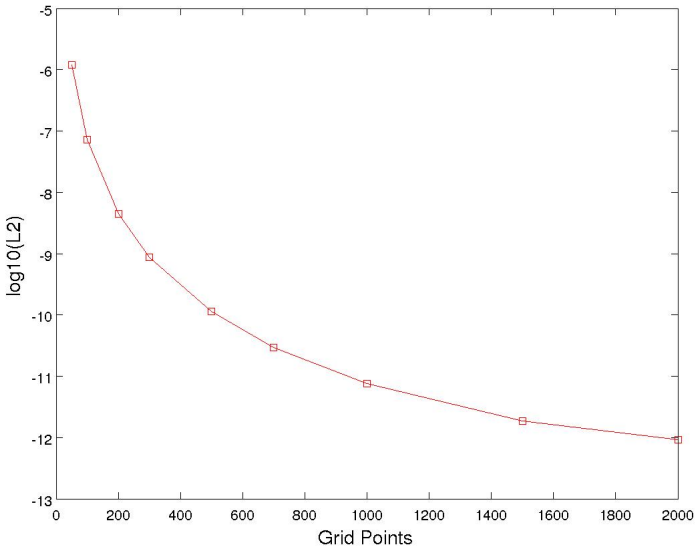

Figure 2.2: $log_{10}(L_2)$ vs. grid points per axis. Numerical resolution is grid points per axis squared, i.e. $nx = nz$. L_2 error norm decrease when the number of grid points is increased. GPU results correspond to CPU ones.

$45° - \frac{\varphi}{2} < \theta < 45° - \frac{\psi}{2}$, ((Kaus, 2010),(Poliakov et al., 1994)).
We perform extension and compaction experiments. The domain is a 100 km^2 crust square with free surface boundary condition at the top, zero tangential velocity at the bottom and Dirichlet boundary conditions for the X direction velocity at the sides accounting for extension or compression. To improve shear band formation, we use a high v_x velocity at the sides of 1 $m/year$. We varied internal frictional angles, $\varphi = 20°$, $30°$ and $40°$.
Figure 2.3 and Figure 2.4 shows the second invariant of the strain tensor for compressional and extensional cases respectively. Compressional experiments shows dip angle values very close to Coulomb angles. (Kaus, 2010; Popov and Sobolev, 2008) reported similar results for elasto-visco-plastic rheology materials and Hansen et. al. reported dip angles near to Coulomb values for elasto-plastic rheology using a mesh-free finite element method, (Hansen, 2003). For extensional cases, the upper part of the domain shows effects due to boundary conditions where tensile failure seems to play a principal role. The reason for the long tensile fractures is the fast extensional velocity. In the bottom part clear shear bands are present at angles that lie between Roscoe and Coulomb angles for all cases.

2.4.3 Poro-elasto-plastic modeling

The model domain is a section of crust of 10×10 km under compression or extension with an over-pressurized region at 6 km depth. Model parameters are listed in table 2.1. The fluid overpressure is 100 MPa. First, a fast compression/extension is applied to create a system of fractures. During this stage a network is create that avoiding any artificial introduction of fractures using, for example, stochastic

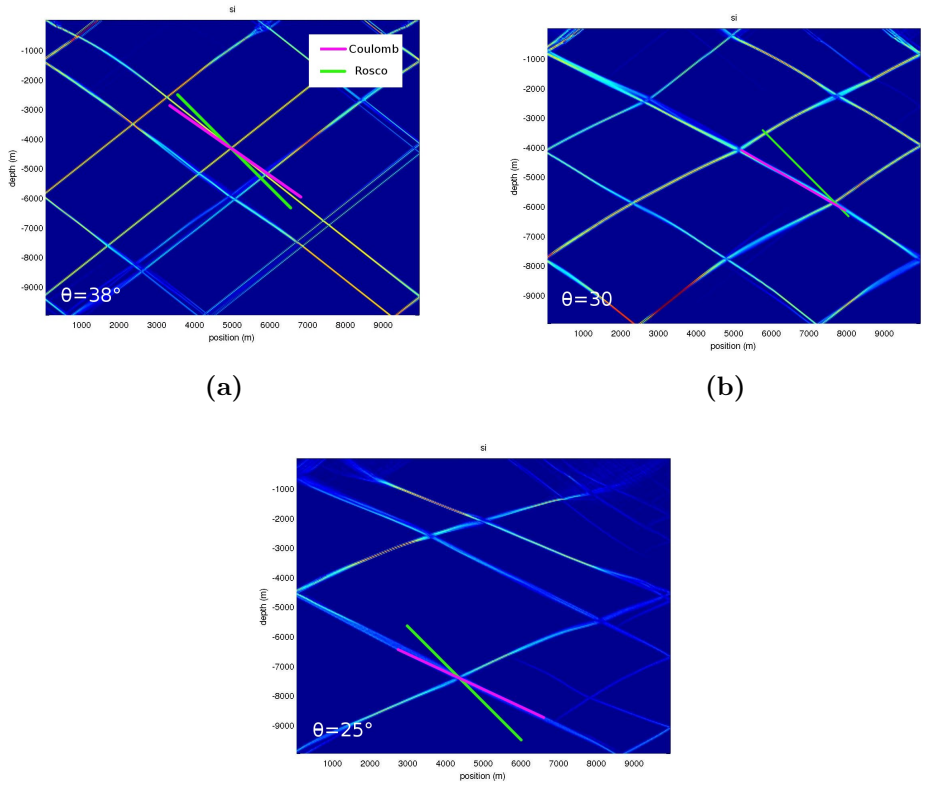

Figure 2.3: Second invariant of strain tensor (si) showing shear bands formation and dip angles θ for elasto-plastic media under compression with internal frictional angles (a) $\varphi = 20°$, (b) $\varphi = 30°$ and (c)$\varphi = 40°$. For all numerical experiments dilation angle was set equal to zero, $\psi = 0$. Pink lines are the Coulomb angles and green lines are Rosco angles. In all cases θ is very close to the Coulomb value. Numerical resolution: 300×300.

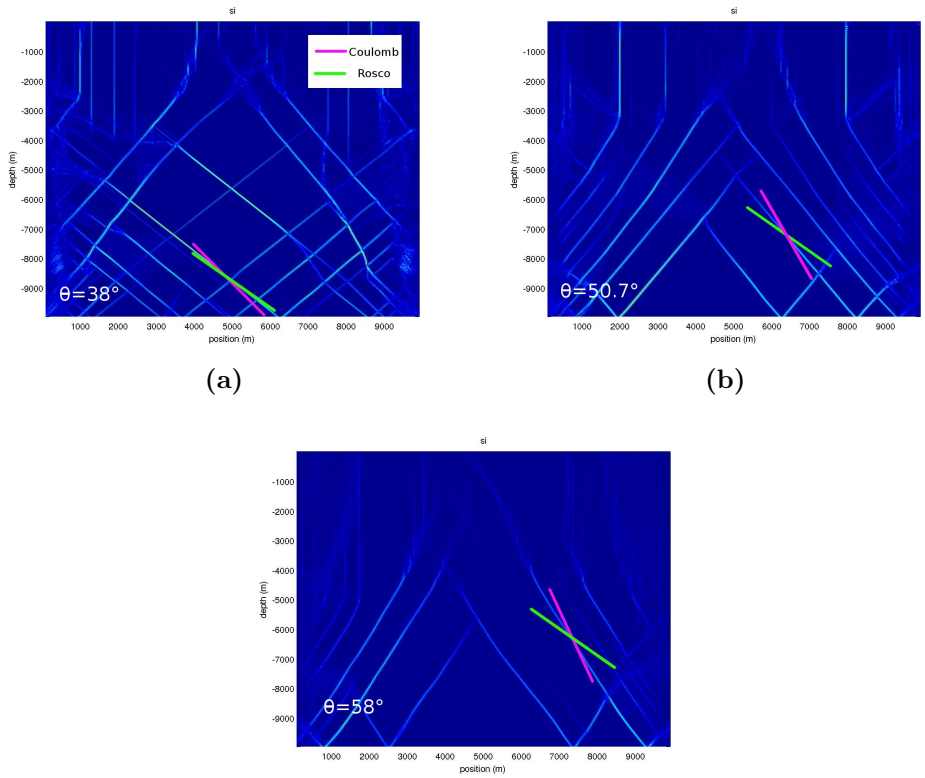

Figure 2.4: Shear band formation and dip angles θ for elasto-plastic media under extension cases. Dilation angle $\psi = 0$ and frictional angles (a) $\varphi = 20°$, (b) $\varphi = 30°$ and (c)$\varphi = 40°$. For all cases, dip angle θ lays between Roscoe (green line) and Coulomb (pink line) angles. In the upper part of the domain tensile fracturing is appreciated. Numerical resolution: 300×300.

Parameter	Hydrostatic pressure layer	Overpressurized layer
Cohesion (MPa)	20	20
Poisson ratio	0.27	0.3
Bulk modulus (GPa)	35	41
Porosity ϕ	0.01	0.10
Intrinsic permeability κ_o (m^2/s)	10^{-17}	10^{-16}
σ^* (MPa)	33	35
Pore compressibility β_ϕ (Pa^{-1})	10^{-8}	10^{-8}
fluid compressibility β_f (Pa^{-1})	10^{-10}	10^{-10}

Table 2.1: Model parameters

methods. Fractures are created in response to the regional stress field with frictional angles distributed randomly around 30°.

During the fracture network formation time, cohesion of failed points is set to zero. If the point fails in tensile mode the permeability is set to two orders of magnitude higher than the intrinsic permeability of the intact rock. In case of shear fracturing, permeability increases one order of magnitude from the intact rock value. Following this fast compression or extension stage, boundary velocities are set to zero and the system relax until steady state is achieved. During this relaxation time, energy is released by fracturing and deformation, thus allowing further growth of the network, and relaxing much of the localized stressed points. When stress relaxation is complete, cohesion of the failed points is set to a value lower than the background cohesion to simulate healing of the fractures. In our numerical experiments, cohesion of the cracks after relaxation is set to a fourth of the background cohesion. Time is set to zero and diffusion is initiated. Figure 2.5 and Figure 2.6 shows the permeability, yield function and fluid pressure at time = 180 days after the onset of diffusion for compressional and extensional case respectively. Figure 2.5 presents the permeability (a), yield function (b) and fluid pressure profiles (c) (d), (e) at time =30, 60 and 180 days after the diffusion release. Maximum values of the fractures permeability is around $1e^{-8}$ m/s^2 in the overpressurized layer. However, permeability drops in the hydrostatic layer locking the fluid pressure. Even for high permeabilities in the overpressurized part, the contrast of the permeability between the overpressurized layer at the bottom and the hydrostatic layer produces "lock up" of the fluids. Yield function (b) shows the closeness to failure (dark red). Fractures are critically stressed and about to fail. High resolution allows development of complex fracture networks with damage zone surrounding the main faults. Figure 2.6 shows the permeability (a) and yield function (b) and fluid pressure profiles (c) ,(d),(e) at time=30, 90 and 180 days after the diffusion release for the extensional case. Beside shear bands, non-localized tensile fractures can be appreciated. Extension enhance fluid pressure migration through the fractures on the hydrostatic pressurized layer. Large damage zones are appreciated developing from the edges of the domain. The reason of these damage is the fast extensional velocity applied

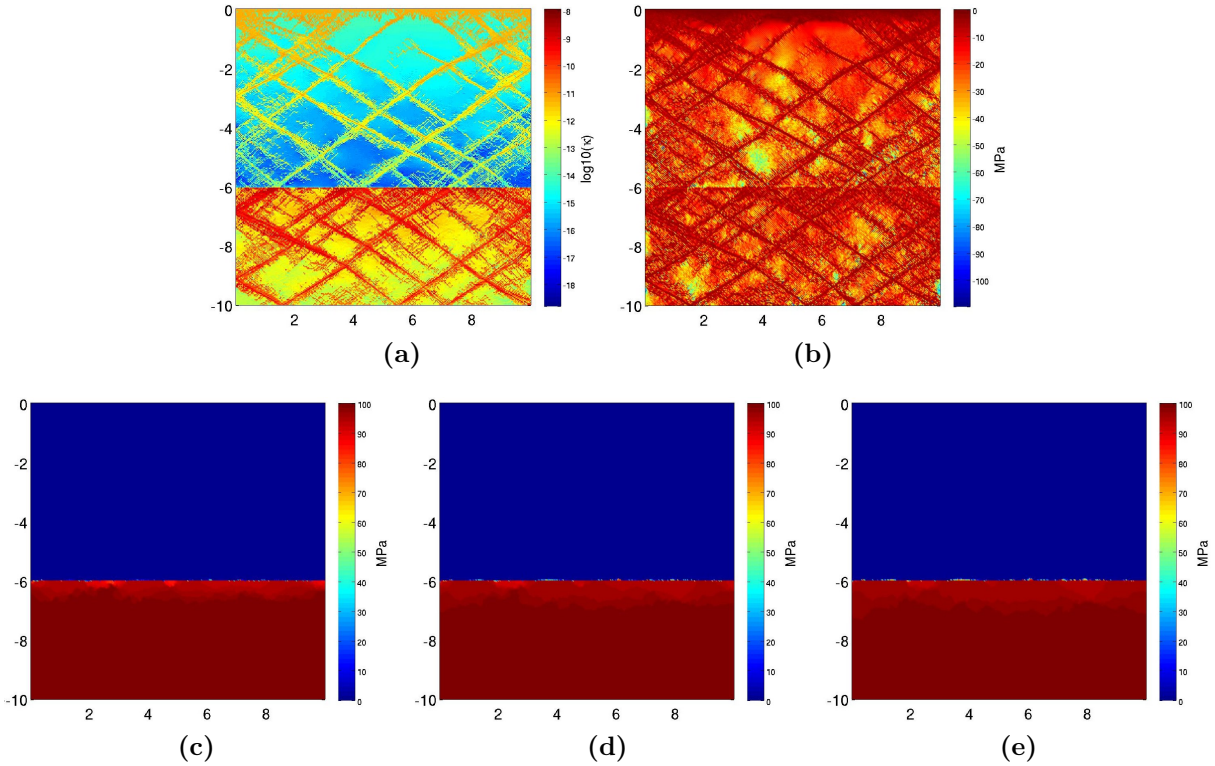

Figure 2.5: Permeability (a), yield function (b) and fluid pressure profile (c), (d), (e) at time =30, 60 and 180 days after the diffusion release for the compressional case. Numerical resolution: 300×300, 33m. Maximum values of the fractures permeability is around $1e^{-8}$ m/s^2 in the overpressurized layer. However, permeability drops in the hydrostatic layer locking the fluid pressure. Even for high permeabilities in the overpressurized part, the contrast of the permeability between the overpressurized layer at the bottom and the hydrostatic layer produces "lock up" of the fluids. Yield function (b) shows the closeness to failure (dark red). Fractures are critically stressed and about to fail. High resolution allows development of complex fracture networks with damage zone surrounding the main faults.

during the fracture creation time. Tensile failure, vertical faults, are present in the overpressurized and the hydropressurized sections of the domain.

2.5 Conclusions

We developed a poro-elasto-plastic model coupled to non-linear diffusion and implemented in GPU. The model is completely explicit so its computation is very efficient using the GPU architecture. GPU-based modeling offers significant advantages and allows fast, high resolution simulations of the underlying process. Nonlinear diffusion equations and elasto-plastic equations have been implemented with von-Neumann and Dirichlet boundary conditions. The introduction of switch functions allows implementing plasticity in GPU and, in general, to handle program branching in a

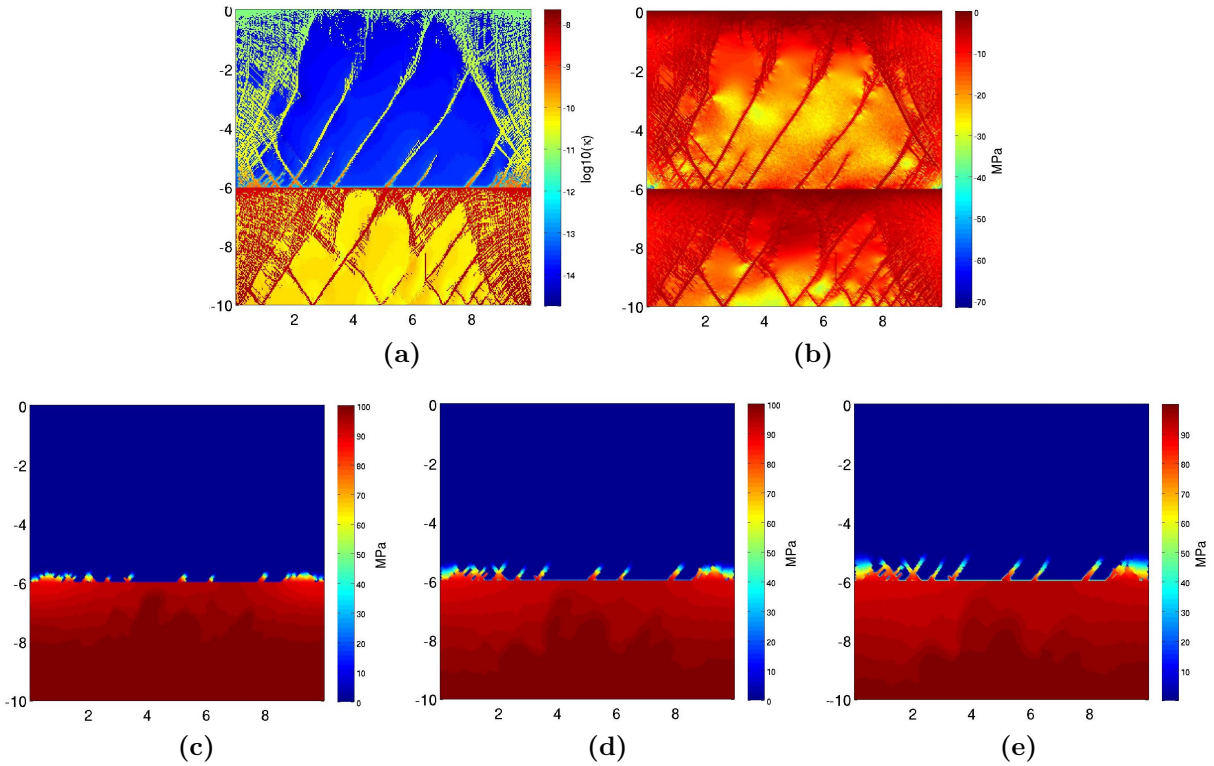

Figure 2.6: Permeability (a) and yield function (b) and fluid pressure profiles (c) ,(d),(e) at time=30, 90 and 180 days after the diffusion release for the extensional case. Numerical resolution: 300×300, 33m. Beside shear bands, non-localized tensile fractures can be appreciated. Extension enhance fluid pressure migration through the fractures on the hydrostatic pressurized layer. Large damage zones are appreciated developing from the edges of the domain. The reason of these damage is the fast extensional velocity applied during the fracture creation time. Tensile failure, vertical faults, are present in the overpressurized and the hydropressurized sections of the domain.

GPU efficient way.

Results of the code benchmarking are in accordance with previous studies. The results of the dip angles of shear bands of our model agrees with other numerical models. The Method of Manufactured Solutions (MMS) was used to benchmark the nonlinear diffusion equation giving accordance between CPU and GPU double precision implementations.

The case of the full poro-elasto-plastic system under extension and compression were presented. Complex fracture networks naturally develop from the stress conditions. Delocalized fractures, shear and tensile fractures can be appreciated. In the case of compression the fluids are "lock" due to the decrease of the permeability. Extension is favorable for fluid mobilization. Some of the aftershock sequences related to fluid like the Colfiorito case (Miller et al., 2004) and L'Aquila (Terakawa et al., 2010) are extensional environments. This unlocking of the fluids has been proposed as a trigger factor in earthquake induced volcanic eruptions (Walter and Amelung, 2007). Due to the fast compressional and extensional velocities applied during the fracture creation large damage zones develop at the edges of the domain. Fracturing begins at the edges. This effect can be diminished lowering the compressional and extensional velocities. A detail analysis of the evolution of the fracture network, its geometry, the permeability of the networks and behavior of the related parameters, will be done in the future. However, this work presents a model capable of develop and handle very complex fluid-rock interactions.

This model can be used in different problems in geodynamics, e.g. effect of earthquakes on permeability and fluid migration or to analyze hydrofracturing in engineering applications such as geothermal systems or oil and gas reservoir simulations.

To the best of our knowledge, this is the first implementation of poro-elasticity or plastic rheology in GPU. Due to complexity of our system its correct implementation in GPU architecture opens by itself a new area of application for GPU based modeling. Developments of a 3D implementation of our model using GPU clusters will be presented in the future.

2.6 Acknowledgments

We thank the German Research Foundation, Deutsche Forschungsgemeinschaft (DFG) for the financial support through the project no. MI 1237/2-1.

Chapter 3

GPU numerical reproduction of hydrofracture experiments in Poro-elasto-plastic material

3.1 Abstract

Modeling laboratory data at the scale of the experiment is extremely important because if the model matches the observations at this small scale, then it means that the model captures the dominant underlying physics. Here I apply a numerical model of a pore-elastic plastic rheology coupled to non-linear diffusion to compare with laboratory fluid injection experiments. The model is computed on the GPU platform, allowing very high resolutions simulations of a continuum formulation at the scale of the grain. We show an excellent correlation between model and experiment of the evolved fracture topology, providing strong indication that the dominant physics are respected and modeled. I expect that additional future simulations of wave propagation through the numerical samples will show equally good correlations with measured changes in seismic velocities, or at least lead the way to further model improvements.

3.2 Introduction

Hydrofracturing is a common procedure for enhancing production of geothermal systems or fossil fuel reservoirs. Tensile and shear fracturing can be achieved by injecting high pressure water in the rock, which enhances permeability and thus the fluid flow within the hydrological system. If the rock is fractured, the injection of high pressure fluids into fault zones reduces the frictional resistance, thus lowering of the shear stress necessary for failure (Terzaghi, 1923; Nur, 1971) and inducing seismic events. High pressure fluid-induced seismicity is well documented in enhanced geothermal systems and hydrocarbon reservoirs (Majer et al., 2007; Häring et al., 2008; Shapiro and Dinske, 2009; Phillips et al., 2002; Audin et al., 2002; Glowacka et al., 1999), but modeling the underlying physics is complicated by the complex

interactions between fluid flow, shear slip and changes in hydraulic properties at the onset of slip.
In Enhanced Geothermal Systems (EGS), earthquakes are necessary to produce the permeability enhancement, but these systems are typically near cities to make this energy source economically viable, so the magnitude of induced earthquakes is of significant concern. The public response and/or acceptance to induced seismic events is, in the end, a primary factor for the success or viability of a sustainable operation. Two large European EGS projects, Soulz in France and the Deep Heat Mining Project Basel in Switzerland, were either suspended or cancelled because of public outcry to induced earthquakes (Häring et al., 2008; Majer et al., 2007). In the Basel experiment, the strongest event had a magnitude of M_L=3.4, which resulted in some structural damage and ended that project.

Part of the problem with convincing the public is that few models exist that accurately describe these systems, so projections of what might be expected from inducing seismicity are restricted to statistical analyses or 'educated guesses' of what will happen. The purpose of this study is to develop a model that captures the dominant processes acting, namely fracture, pore-elastic stresses, and fluid flow and fluid pressure propagation associated with fluid injection. Our approach is to numerically model well-constrained laboratory experiments, and use those results to scale to the larger EGS system.
There are a vast literature on laboratory experiments to analyze hydrofracturing. In a study of hydraulic fracturing in Weber sandstone (Lockner and Byerlee, 1977), where fluids were injected until sample failure, it was found that injection rate controls the failure mode of either shear or tensile failure. Typically geothermal reservoir systems are critically stressed to some degree, so particular efforts were made in laboratory experiments under similar stress conditions. (Mayr et al., 2011; Stanchits et al., 2011) studied acoustic emissions (AE) in triaxial experiments of critically stressed Flechtingen sandstone during fluid injection, and showed that recorded cloud of acoustic emissions strongly correlated to the position of the water front.

Simulating geothermal reservoirs at the field scale requires that numerical models have been tested and calibrated at the high resolution scale of the laboratory. That is, numerical models should be able to reproduce laboratory scale experiments before those same models can be used at the larger scale.
In this paper, we present numerical results of a new, high resolution 2D poro-elastoplastic code to reproduce recent experimental results of fluid injection into sandstone (Stanchits et al., 2011). Our model includes the effects of the deformation of the rock on the hydraulic properties and the fluid pressure feedback on the elastic properties of the rock, and we model the development, propagation, and interactions between evolving shear and tensile fractures. The following couplings are introduced: changes in the intrinsic permeability and cohesion due to fracturing, changes in the porosity, bulk modulus and Poisson's ratio due to changes in the pore fluid pressure. Some proxies has been used to introduce this couplings. The numerical and experimental

results show an excellent match between them.

We use CUDA programming of an explicit finite difference formulation of the governing equations, and implement it on the Graphical Processing Unit (GPU) platform. GPU allows much faster computations due to its inherent parallel architecture at high numerical resolution, and is particularly powerful for solving governing equations that can be formulated into explicit finite difference algorithms, like for example our full poro-elasto-plastic model with adaptive time steppin discussed below. In this paper, we first review the equations of poro-elasto-plastic media, followed by a brief explanation of the numerical model and its GPU implementation. The numerical experiments are discussed and show a very good correlation with experimental observations.

3.3 Theoretical Model

Fluid pore pressure in the crust can be modeled using a nonlinear equation with an effective stress dependent permeability (Zhang et al., 1999; David et al., 1994; Rice, 1992; Miller et al., 2004). For laboratory scales the effective-stress-dependent permeability and source terms can be negleted. With these assumptions the flow equation reduces to

$$\frac{\partial P_f}{\partial t} = \frac{1}{\eta \cdot (\beta_f + \beta_\phi)} \nabla \frac{\kappa_o}{\phi} \nabla P_f. \tag{3.1}$$

where P_f is the fluid pressure, κ_o is the permeability intrinsic, η is the fluid viscosity, ϕ is the porosity, β_f is the fluid compressibility and β_ϕ is the pore compressibility. Thi equation accounts for changes int the porosity and intrinsic permeability. As discussed later, the diffusivity κ_o increases by some amount when the failure occurs. The poro-elastic stress tensor is given by

$$\sigma_{ij} = 2G\epsilon_{ij}^{pe} + 2G\epsilon_{kk}^{pe} \frac{\nu}{1-2\nu} \delta_{ij} + \alpha P_f \delta_{ij} \tag{3.2}$$

where α is the Biot-Willis constant, G is the shear modulus and ν is the Poisson's ratio ((Jaeger et al., 2007),(Detournay and Cheng, 1993)). These equations can be linked together using the Terzaghi effective stress as

$$\sigma_{ij}^{eff} = \sigma_{ij} - \alpha P \delta_{ij}. \tag{3.3}$$

Plastic deformation of rocks can be modeled using Mohr-Coulomb and Griffith criteria

$$F_{tension} = \tau - \sigma_m - \sigma_t \tag{3.4}$$

$$F_{shear} = \tau - \sigma_m \cdot sin(\varphi) - C \cdot cos(\varphi) \tag{3.5}$$

$$F = max(F_{tension}, F_{shear}) \tag{3.6}$$

where F is the yield function, φ is the internal frictional angle, τ is the stress deviator, σ_m is the mean stress, σ_t is the tensile strength of the rock and C is the

rock cohesion. The plastic strain rates are given by

$$\dot{\epsilon}_{ij}^{pl} = 0 \text{ for } F < 0 \text{ or } F = 0 \text{ and } \dot{F} < 0 \tag{3.7}$$

$$\dot{\epsilon}_{ij}^{pl} = \lambda \frac{\partial q}{\partial \sigma_{ij}} \text{ for } F = 0 \text{ and } \dot{F} = 0. \tag{3.8}$$

We use non-associative plastic flow rules (Vermeer and Borst, 1984)

$$q_{tension} = \tau - \sigma_m \tag{3.9}$$

$$q_{shear} = \tau - \sigma_m \cdot sin(\psi). \tag{3.10}$$

In this report the dilatancy angle is $\psi = 0$.

3.4 GPU implementation

Computation in graphical cards or Graphics Processor Units (GPU's) has proven advantageous for non-graphical purposes (Griebel and Zaspel, 2010; Zaspel and Griebel, 2011; Nageswarana et al., 2009; Sorensen and Mosegaard, 2006; Michéa and Komatitsch, 2010; Lastra et al., 2009; Vogt et al., 2008; Yang et al., 2007; Stivala et al., 2010). The CUDA programming language, introduced at the end of 2006 by NVIDIA, has facilitated GPU usage in physical modeling, (NVIDIA, 2011).
GPU's substantially accelerate physical modeling because its architecture allows intensive parallel computation over large data sets by giving more importance to data processing than to data cacheing or data control. This is accomplished by including many so-called *streaming processor cores*, that execute the same instruction stream in parallel. The *streaming processor cores* perform easy arithmetic operations intensively, i.e., it performs many more arithmetic operations than memory operations, limiting the amount of cached memory necessary. GPU's are well suited for problems that can be described in a parallel way, in which single instructions operate over the whole data or large parts of the data. Finite difference methods fall within this classification.
GPU's have three main write/read memory types: register, fast cached shared memory and global uncached memory. We take advantage of this and implement the 2D poro-elasto-plastic media using shared and global memory. To accelerate our code we compute the central part of the domain using fast shared memory and boundary conditions are computed using global memory. The correct memory management result in a fast, high-resolution efficient implementation.
We use a first order in time, fourth order in space finite difference scheme to solve the nonlinear diffusion equation **??**. To solve the elastodynamic equation 3.2 we use a staggered grid scheme with centered cells. Stresses are located in the cell centers and velocities on its corners. At the end of every iteration, porosity, bulk modulus and Poisson's ratio are updated using a linear function dependent on pore-fluid pressure.

3.5 Numerical Model of Hydrofracturing in Triaxial Experiments

We test our numerical model by comparing our results to triaxial hydrofracture experiments in Flechtingen sandstone reported by Stanchits et.al. and Mayr et.al. (Mayr et al., 2011; Stanchits et al., 2011). In their experiments, samples of 50 mm diameter and 105-120 mm in length were subjected to confining pressures from 40-50 MPa and loaded axially from 260 MPa until the critical stress of about 290 MPa was reached.
We modeled two of their experiments, numbered Fb20 and Fb24. To be consistent with their experiment names, we call our simulations NFb24 and NFb20 (N for numerical). In experiment Fb24, distilled water was injected from the bottom area of the sample with a pressure of 5.5 MPa, while in experiment Fb20, a borehole was drilled to approximately half the sample length into which fluid pressure of 5MPa was injected.

We use the viscosity at 25 ℃, $\eta = 8.9 \times 10^{-4}$ Pa/s and an the intrinsic permeability value for the intact rock is $\kappa_o = 1 \times 10^{-17}\ m^2$. To approximate the permeability change due to fracturing, permeability was increased by one or two orders of magnitude for shear and tensile fractures (David et al., 1994; Zhang et al., 1999; Mitchell and Faulkner, 2008). Because the model is pore-elastic, both drained and undrained elastic constants are needed. Young's moduli for drained Flechtingen sandstones are in the range E=23.0-29.0 GPa with Poisson's ratio $\nu = 0.12$ (Backers, 2004). Undrained elastic constants are not available for Flechtingen sandstone, so we use the undrained elastic constant values determined for Ruhr sandstone because these have similar drained properties as the Flechtingen sandstone, $E_u = 30$ GPa , $\nu_u = 0.31$, (Jaeger et al., 2007). The internal frictional angle is assumed being φ =35 degrees, and a tensile strength of $\sigma_t = 6$ MPa (Backers, 2004). We introduce some initial heterogeneity by choosing cohesion values normally distributed around 20 MPa. Strain weakening was modeled reducing the cohesion of the failed points to zero. We assume porosity increases linearly from 0.055 at zero pressure to 0.15 at 5MPa with fluid pressure $2 \times 10^{-8} Pa^{-1}$, with constant pore compressibility, therefore resulting in a range of storitivities. Additional detail of the laboratory experiments are found in (Mayr et al., 2011; Stanchits et al., 2011). Model parameters are listed in Table 3.1

Our mesh resolution is 150×315 in the horizontal and vertical direction, respectively, resulting in a finite difference cell length of 0.333×10^{-3} m. The mean quartz grain size of the Flechtingen sandstone is about 0.1^{-3} to 0.5^{-3}m, so our continuum simulation has the resolution of approximately the grain scale. The simulation time is about 2 hours, and although we can not state the simulation time if this were run on CPU's instead of GPU's, our guess is that those simulations at this resolution would be on the order of 24 hours.
We set the numerical confining pressure to 50 MPa and increase the the axial stress until the numerical rock is about to fail rock is about to fail by checking the maximum value of the yield function 3.4. For the simulation NFb20 the critical axial stress

Experiment	E (GPa)	G (GPa)	K (GPa)	ν	K_u(GPa)	ν_u	κ_o m^2	φ	ϕ	ϕ_u
NFb20	29	12.946	12.719	0.12	30	0.31	1×10^{-17}	35°	5.5%	15%
NFb24	23	10.268	10.088	0.12	30	0.31	1×10^{-17}	35°	5.5%	15%

Table 3.1: Model parameters for numerical experiments. Young's modulus are the same as in (Stanchits et al., 2011). Drained Poisson's ratio for Flechtingen sandstone is taken from (Backers, 2004). Undrained parameters are taken form Ruhr sandstone (Jaeger et al., 2007). The drained parameter of Ruhr and Flechtingen sandstones are very similar to each other. We introduce an undrained porosity ϕ_u to account for expansion of the pores and changes due to fracturing. Flechtingen sandstone tensile strength $\sigma_t = 6$ MPa. Cohesion was set to 20 MPa

was 261.31 MPa and for simulation NFb24 the critical stress was 266.166 MPa. A sketch of the numerical model is shown inFigure 3.1.
For the diffusion, we impose a Dirichlet boundary condition at the bottom and determined by the injection pressure, and a zero flux boundary condition for the remaining edges. The sample is considered frictionless on the top and bottom boundaries and free to deform along the right and left boundaries.

3.6 Results and Discussion

The results of the numerical experiment NFb24 are shown in Figures Figure 3.2 and Figure 3.3. The upper row shows the yield function (closeness to failure), where the darker red means that this part of the sample is closer to failure. The lower row shows the pore fluid pressure profile.

We first investigate the effects of changes in the fracture permeability. In Figure Figure 3.2, the permeability of the fractures were increased by one order of magnitude higher than the background permeability. At time=30 s, acoustic emissions (AE), shown as black dots, distribute over the sample following the formation of micro-cracks (a). At time=240 s, small cracks develop and AE's occur in the neighborhood (b)-(c). After 500 s, no clear shear fracture is observed(d).

In figure Figure 3.3, we increased fracture permeability by two order of magnitude higher than the background permeability. At time= 30s microcracks form in the sample (a) as in the previous case. At time=240 s, a clear long fracture and three small fractures develop (b), and total failure of the sample occurrs at approximately 360 seconds after the start of injection (c). From the three secondary fractures just one continues to grow, and at time=500 s, secondary fractures at the end points of the main fracture develop (d), which we attribute to the influence of boundary conditions, or as "reflections" of the main fracture on the boundaries. The laboratory experiment would end at total failure, time=360 s.

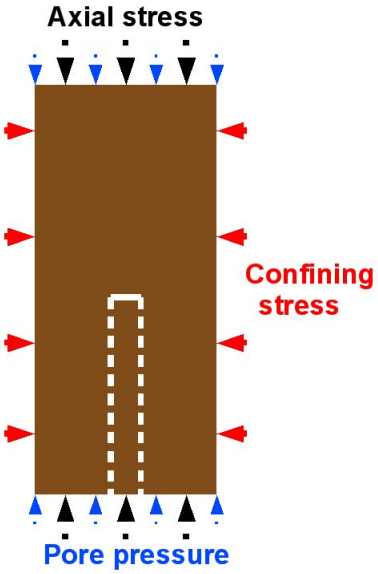

Figure 3.1: Setup for numerical hydrofracture experiments. Confining stress is set at 50 MPa for both numerical experiments. The borehole in numerical experiment NFb20 is designated by the white lines. Axial stress for NFb20=261.31 MPa and pore fluid pressure P_f=5 MPa. For numerical experiment NFb24: axial stress was 266.166 MPa and fluid injection pressure P_f=5.5 MPa. Samples are considered frictionless at the top and bottom edges and at left and right edges are free to deform.

Figure 3.4 presents the results of the numerical experiment NFb20. At time=30 s tensile fractures develop from the walls of the borehole (a). At time=240 s a clear shear fracture develop from the top of the borehole (b). Secondary fractures are observed at time=360 s (c). These fractures develop from the walls of the borehole and the corners of the sample. The sample fails at between time=420-500 s (d). Our results shows good agreement with the laboratory experiments. A picture of the laboratory experiment is presented for comparison (e) (taken from (Stanchits et al., 2011)).
Injection of fluid pressure changes the overall stress state of the sample, creating micro-fractures and manifested as AE's of the growing fracture. Our results show that the evolving permeability of the micro-fractures is the primary driver in their propagation. This is clear by the differences in behavior between increasing permeability by either one or two orders of magnitude when a region reaches the failure condition. When the fracture permeability is set two orders of magnitude higher than the background permeability, clear long shear fractures develop and the material fails very similar to the laboratory experiments. The principal cause for this is that fluids localize in the fractures and pore-elastic stresses (seepage forces) dominate and promote additional fracture growth (Rozhko et al., 2007).
Permeability has been pointed out as a main factor in crustal geodynamics (Miller and Nur, 2000). In geothermal systems and induced seismicity fluid pressure localization could be a main driving factor. Even for laboratory scale experiments, where fluid pressure are considerably smaller compared to crustal processes, permeability effects are appreciable. The correct treatment of permeability for large scale processes is one of the main issues in fluid-rock interaction simulators. At the crustal scale, both large permeability increases at the onset of failure and an effective stress dependent permeability are important. For laboratory scales increasing the permeability of the fractures by two orders of magnitude gives qualitatively good results, and although this educated guess for increasing permeability is intuitive, other permeability functions might also be used. For example, permeability can be made a function of strain or a function of the porosity (Cappa and Rutqvist, 2011). We will address these points in future research. One limitation of our model is how porosity changes, and in a future version of our simulator, porosity will be explicitly computed from the elastic and plastic strains (Chin et al., 2000).

3.7 Conclusions

We reproduced laboratory experiments using a new poro-elasto-plastic GPU simulator with our continuum code at the resolution of the grain scale. The formation of microcracks and their evolution was modeled, and we achieved a very good comparison to small-scale laboratory experiments. The most important effect and result from our simulations is the step-wise increase in permeability when a crack is formed. Our comparison with the laboratory experiments show that increasing permeability two-orders of magnitude give the best results. Fast pressure diffusion from the increases induces seepage forces and localization that promotes further failure. The

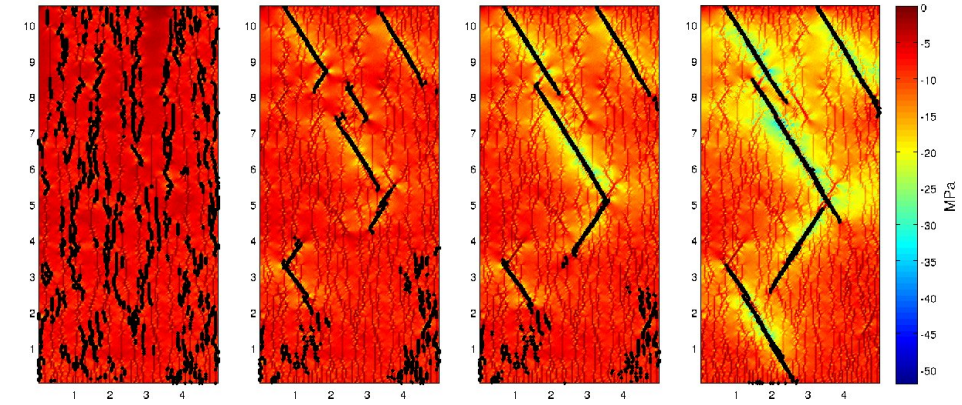

(a) time=30 s **(b)** time=240 s **(c)** time=360 s **(d)** time=500 s

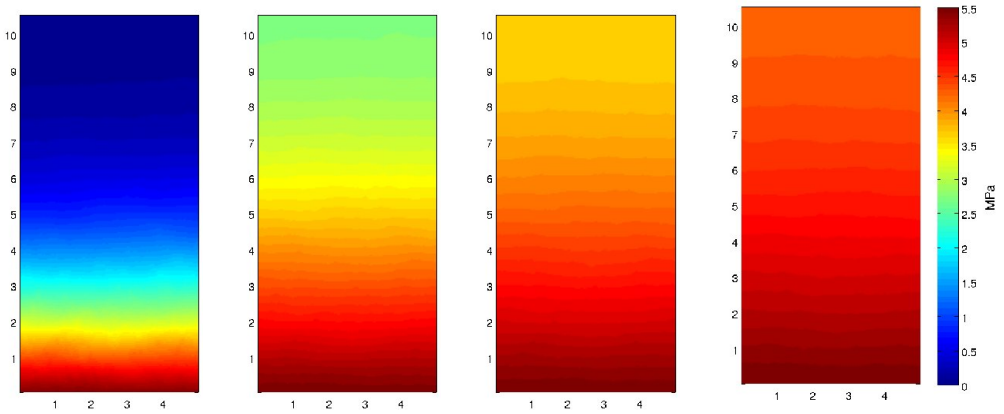

(e) time=30 s **(f)** time=240 s **(g)** time=360 s **(h)** time=500 s

Figure 3.2: Results of the numerical experiment NFb24 with fracture permeability one order of magnitude higher than background permeability. First row shows the yield function or closeness to failure. Failure occurs at yield function=0. Black dots are the acoustic emissions (AE's). Second row is the pore fluid pressure profile. At time=30 s , AE's (black dots) of microcracks formation (a). At time=240-360 s shear cracks develop and AE's occur around them (b)-(c). After 500 s there is no total failure but 5 long cracks are appreciable(d).

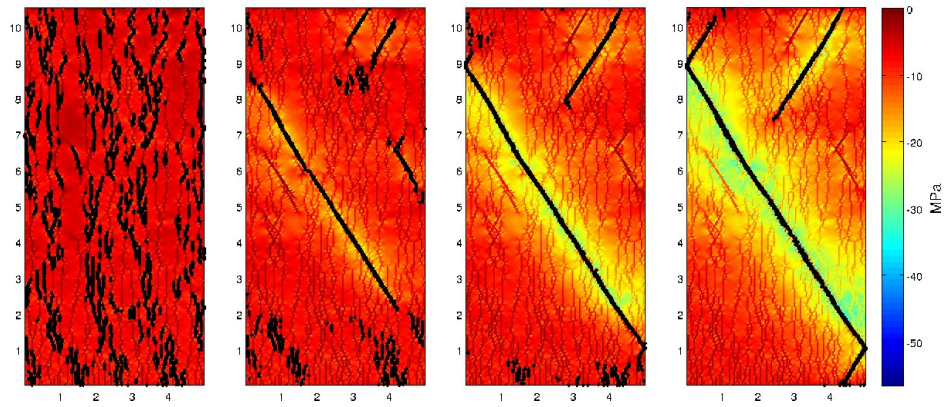

(a) time=30 s **(b)** time=240 s **(c)** time=360 s **(d)** time=500 s

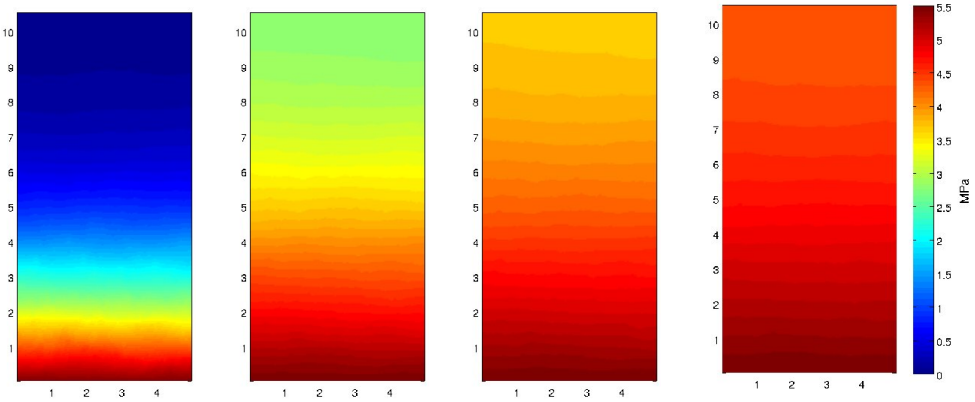

(e) time=30 s **(f)** time=240 s **(g)** time=360 s **(h)** time=500 s

Figure 3.3: Numerical experiment NFb24 with fracture permeability two order of magnitude higher than background permeability. At time= 30s microcracks develop in the sample . At time=240 s a clear long fracture and three small fractures developed . Total failure of the sample occurred at approximately 360 seconds after injection is started .

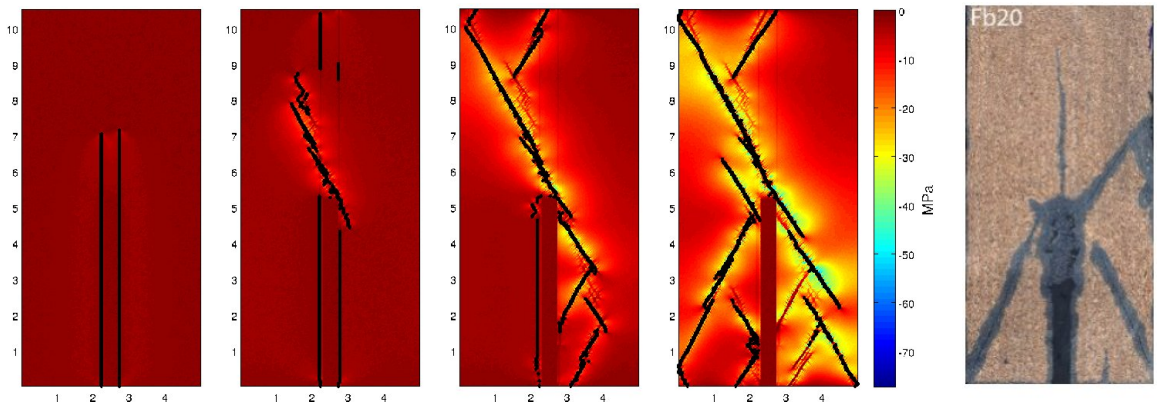

(a) time=30 s **(b)** time=240 s **(c)** time=360 s **(d)** time=500 s **(e)**

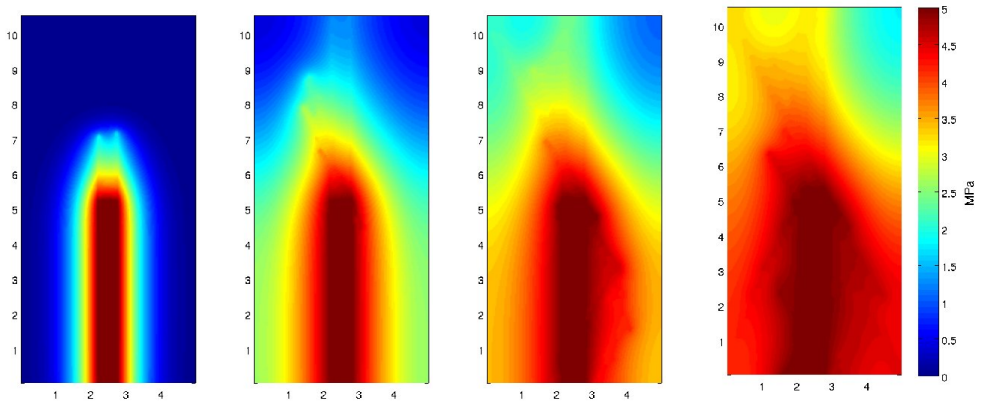

(f) time=30 s **(g)** time=240 s **(h)** time=360 s **(i)** time=500 s

Figure 3.4: Numerical experiment NFb20. Fracture permeability two orders of magnitude higher that background permeability. tensile fractures develop from the walls of the borehole (a). At time=240 s a clear shear fracture develop from the top of the borehole (b). Different secondary fractures can be appreciated at time=360 s (c). These fractures develop form the walls of the borehole and the corners of the sample. The sample fails at between time=420-500 s (d). For comparison (e) shows the final state of the laboratory sample. From (Stanchits et al., 2011).

results presented shows that permeability is main factor in rock-fluid interactions and these results, now calibrated against laboratory experiments, can now be applied to larger scale systems such as enhanced geothermal systems. They are calibration of our model for further developments and applications.

3.8 Acknowledgments

We thank Dr. Georg Dresen for personal communication during the preparation of this manuscript. We thank the German Research Foundation, Deutsche Forschungsgemeinschaft (DFG) for the financial support through the project no. MI 1237/2-1.

Chapter 4

Simulation of fluid induced seismicity accelerated in GPU. Application to Enhance Geothermal Systems

4.1 Abstract

Injection of high pressure fluids into the earth is an important aspect of the future of Green Energy. This includes Enhanced geothermal systems, CO2 sequestration, extraction of gas-shales and nuclear wast isolation. Here I apply a numerical model of a pore-elastic plastic rheology coupled to non-linear diffusion to compare simulate a generic EGS system and a direct application to the Basel, Switzerland, fluid injection experiment. Results of the simulation show that the usual assumption of keeping fluid pressure below sigma 3 is not an adequate constraint to restrict hydrofracture, because local heterogenity due to pore elastic effects and the evolving fracture network result in local stress states permit hydrofracture by overcoming the local sigma 3 and not the far-field sigma 3. Once hydrofracture occurs even at a small scale, the hydro-mechanical consequences of this local phenomenon, perturb the overall future evolution the system and therefore its long-term viability.

4.2 Introduction

Geothermal energy is one of the candidates for a sustainable clean energy source for the future. Thermal energy of the Earth is enough to satisfy the present and future energy needs of the society (Duffield and Sass, 2003).

In natural conditions, economically viable geothermal reservoirs must be located at drillable depths, in water-saturated rocks with high porosity and conductivity at temperature high enough to produce steam or hot water at high enough flow rates. The places fulfilling these conditions are not widespread. However, hot-rock is avail-

able almost everywhere at drilling depths.

New techniques have been develop to use hot dry rock for the production of energy. For example, Enhanced Geothermal Systems (EGS) that are fractured, hot-rock reservoirs engineered to extract heat by the circulation of water (U.S.D.E, 2008). Permeability of poor geothermal systems could be enhanced by pumping water at pressure high enough to activate pre-existing fractures or creating new ones. EGS projects has been implemented in the Geysers geothermal field in the U.S.A, Cooper Basin in Australia, Berlín geothermal field in El Salvador, Soultz-sous-Forêts in France and Basel in Switzerland (Majer et al., 2007). EGS are projected as a main energy source in the near future(U.S.D.E, 2008).

However, the induced microseismicity linked to the activation of fractures, is a main issue for EGS projects as well as reservoirs exploitation (Ohtake, 1974; Majer et al., 2007; Häring et al., 2008; Shapiro and Dinske, 2009; Phillips et al., 2002; Audin et al., 2002). Generally, EGS projects are situated near to cities to avoid unnecessary loss of heat during transportation and distribution of hot water. The public response to induced seismicity, due to its frequency or magnitude, is a main factor in EGS project operation. The last two EGS projects, Soultz-sous-Forêts in France and Deep Heat Mining in Basel, Switzerland, have been either suspended or even canceled due to public unrest caused by high seismicity. In the case of Soultz-sous-Forêts high seismicity, with a large event of magnitude of 2.9 M, produced its temporal suspension and in Basel high levels of seismicity, the largest even with a magnitude 3.4 M_L, caused it cancellation (Majer et al., 2007; Häring et al., 2008). Is interesting that in both cases the largest event occurred after injection shut-in.

The last case, the Basel Deep Heat Mining (DHM) project deserve special attention. In the DHM project the "safe" pumping fluid pressure was calculated to be 74 MPa based in the inferred regional stress. However, pumping was stopped at a pressure of approximately 29.6 MPa due to high seismicity. Computer simulation of fractured geothermal systems might be a important tool to improve EGS planning and operation.

During the last years, many reports has been published about modeling of poro-elasto-plastic media and applications to geothermal systems (Chin et al., 2000; Taron et al., 2009; Taron and Elsworth, 2010), fluid induced seismicity,since pioneering work of (Maillot et al., 1999) to (Shapiro et al., 2006; Baisch et al., 2010; Lupi et al., 2011) and CO_2 sequestration (Xu et al., 2006; Rutqvist et al., 2007; Rutqvist et al., 2008; Cappa and Rutqvist, 2011).

Currently different fluid flow-heat flow-rock deformation simulators are available. For example GEOCRACK is a 2D simulator of fluid flow through fracture media. It couples deformation/fluid flow/heat flow. UDEC is 2D simulator that couples deformation and fluid flow, ROCMAS is a 3D finite element simulators of two phase flow (Rutqvist and Tsang, 2003), poroelasticity and thermoelasticity. FRACture is a fi-

nite elements poroelastic-thermoelastic simulator (Kohl et al., 1995). GeoSys/Rockflow and its upgrade OpenGeoSys (Kolditz et al.,) are among the more complex simulators nowadays . They are finite element 3D, multiphase flow, fracture flow, heat transport, chemical process, poroelastic, thermoelastic and elasto-plastic simulator (Wang and Kolditz, 2007). MOTIF (Model Of Transport In Fractured porous media) is a 3D finite element thermomechanical-groundwater flow-heat flow simulator (Guvanasem and Chan, 1995), FRANCON is finite element based 3D simulator of thermo and poroelasticity and TOUGH-FLAC a heat flow-fluid flow-mechanical simulator with capabilities for elasto-plastic deformation. A more comprehensive list with a brief description of the aforementioned codes is presented in (Rutqvist, 2011).

In most of these codes, fractures are treated as static or just small changes are possible. For EGS and fracking, the description of the networks evolution is desirable. A realistic simulator, meant for these applications, must be able to create fractures that follow the regional stress conditions and the fractures must be able to change the background stress introducing stress localization. Stress localization enhance the probability of failure. Critically stressed fractures might yield even if just a very low fluid pore pressure in injected. If fractures are introduced using stochastic methods and they are not allow to evolve, the local stress field might be very different as the irregular stress field resulting from fracture evolution. This might lead to a wrong estimation of the threshold for the injection pressure needed to control microseismicity.

Fractures change also the hydraulic parameters of the rock, mainly the permeability, that can increase orders of magnitude above the background rock permeability (David et al., 1994; Zhang et al., 1999; Mitchell and Faulkner, 2008). Fluids localize in fractures resulting in a highly inhomogeneous pore fluid pressure profile. Gradients of pore fluid pressure introduces significant seepage forces that might promote more failure (Rozhko et al., 2007).

In our numerical model, fractures are develop naturally from the local stress state and they are free to evolve during the simulation. Complex networks and heterogeneous stress fields are produced as a consequence.

To follow the fracture network evolution a very high numerical resolution is used. This process by itself would not give too much advantage because it represent longer computational times and higher computer power. Using Graphics Processor Units (GPU) technology it is possible to reduce computation times and deal with large data matrices (NVIDIA, 2011). GPU's are highly parallel computation devices and have been proven to be a solution for physical modeling when high resolution is required.We develop and efficient, high resolution poro-elasto-plastic simulator in GPU that allows fracture creation and evolution.

This paper is organized as following: in section 4.3 we review the equations of poro-elasto-plastic media. In section 4.4 we give a brief explanation of the GPU parallel architecture and programming. In 4.5 we present simulation of fluid injection in

fractured rock in the vecinity of the borehole and in 4.6 a real world case is modeled: the Basel DHM project. Finally section 4.7 present the conclusions.

4.3 Poro-elasto-plastic model

Stresses in fluid infiltrated rock are described by Biot poroelastic theory (Biot, 1941). The poroelastic stress tensor is defined as

$$\sigma_{ij} = 2G\epsilon_{ij}^{pe} + 2G\epsilon_{kk}^{pe}\frac{\nu}{1-2\nu}\delta_{ij} + \alpha P_f \delta_{ij} \tag{4.1}$$

where α is the Biot-Willis constant, G is the shear modulus and ν is Poisson's ratio. If an effective stress is defined as

$$\sigma_{ij}^{eff} = \sigma_{ij} - P\delta_{ij} \tag{4.2}$$

equation 4.1 is identical to the stress equation for dry rock. Elastic strains are derived from equation 4.1 and force equations

$$\frac{\partial V_x}{\partial t} = \frac{1}{\rho}\left(\frac{\partial \sigma_{xx}^{eff}}{\partial x} + \frac{\partial \sigma_{xz}}{\partial z}\right) \tag{4.3}$$

$$\frac{\partial V_z}{\partial t} = \frac{1}{\rho}\left(\frac{\partial \sigma_{zz}^{eff}}{\partial z} + \frac{\partial \sigma_{xz}}{\partial x} + \rho g\right) \tag{4.4}$$

$$\tag{4.5}$$

with ρ is the density, v_x and v_z is the velocity vector and σ_{xx}^{eff}, σ_{zz}^{eff}, τ_{xz} are the effective stresses.
Plastic yield of rocks can be modeled using Mohr-Coulomb and Griffith yield criteria

$$F_{tension} = \tau - \sigma_m - \sigma_t \tag{4.6}$$

$$F_{shear} = \tau - \sigma_m \cdot sin(\varphi) - C \cdot cos(\varphi) \tag{4.7}$$

$$F = max(F_{tension}, F_{shear}) \tag{4.8}$$

where F is the yield function, φ is the frictional angle, τ is the stress deviator, σ_m is the mean stress, σ_t is the tensile strength of the rock. The plastic strain rates are given by

$$\dot{\epsilon}_{ij}^{pl} = 0 \text{ for } F < 0 \text{ or } F = 0 \text{ and } \dot{F} < 0 \tag{4.9}$$

$$\dot{\epsilon}_{ij}^{pl} = \lambda\frac{\partial q}{\partial \sigma_{ij}} \text{ for } F = 0 \text{ and } \dot{F} = 0. \tag{4.10}$$

where q are the so called flow rules that describe the deformation of the material in the plastic regime (Vermeer and Borst, 1984). Fluid pore pressure diffusion in the crust can be model using a nonlinear diffusion equation with stress dependent

permeability (Gutierrez et al., 2000; Zhang et al., 1999; David et al., 1994; Rice, 1992; Miller et al., 2004)

$$\frac{\partial P_f}{\partial t} = \frac{1}{\phi(\beta_f + \beta_\phi)} \left[\nabla \frac{\kappa_o \cdot \exp\left(-\frac{\bar{\sigma_n}}{\sigma^*}\right)}{\eta} \nabla P_f + \dot{\Gamma}(P_f, T) \right] \tag{4.11}$$

where $\bar{\sigma_n}$ is the normal stress, P_f is the pore fluid overpressure, ϕ is the porosity, β_f is the fluid compressibility, β_ϕ is the pore compressibility, ρ_f is the fluid density, κ_o is the permeability at zero normal stress, σ^* is a scaling constant related to the degree of fracturing of the rock, η is the viscosity. The last term in the right hand side of the equation 4.11 is the source term. For example, (Maillot et al., 1999) related this term to changes in the pore pressure due to compaction or extension of the solid matrix. For the sake of simplicity we take the source term equal to zero in this report.

4.4 GPU implementation

In this Section we present a brief description of GPU's architecture and programming. Refer to (NVIDIA, 2011) for more information.
During the last 12 years Graphics Processor Units (GPU's) have been used as a computing platform for a manifold of physical models: fluid dynamics ((Griebel and Zaspel, 2010),(Zaspel and Griebel, 2011)), geophysics ((Michéa and Komatitsch, 2010),(Lastra et al., 2009)), quantum chemistry (Vogt et al., 2008), molecular dynamics (Yang et al., 2007) to name some. GPU's development is boosted by the video game industry that requires rendering of high definition images at high speed frame rates, i.e. massive number of floating point operations per video frame. GPU's are designed to execute massive number of threads. The company NVIDIA launched in year 2006 the CUDA massive parallel architecture, together with its own programing language (NVIDIA, 2011). The CUDA language is C-like based and offers an easier programing tool than former GPU graphic languages as OpenGl.
GPU's are composed of an array of *streaming multiprocessor* which of them containing eight scalar processors (SP's). In this report we use a GeForce GTX 590 NVIDIA GPU which has two graphic cards with 32 streaming multiprocessor in total. Beside scalar processor, each multiprocessor includes a multi-threaded instruction unit and cached memory. When a program calls a GPU kernel or function, many copies of this kernel are generated, called threads, and are passed to the GPU to be executed. The GPU distributes the threads among the available multiprocessors for execution. The multi-threaded instruction unit within each multiprocessor distribute, manage, schedule and execute threads using the so called *single instruction multiple threads* (SIMT) mode, i.e. the multiprocessor maps multiple threads, all of them representing the same instruction, to the scalar processors to be execute. Threads are executed independently by the scalar processors. GPU's can manage thousands of

threads simultaneously. Last generation GPU's, as the GTX 590, can run 1536 simultaneous threads for multiprocessor. This allows to crush large data set in pieces, accelerating operations over them. This approach is called *single instruction multiple data* (SIMD) parallelization.
Threads are organized in blocks. Threads are accessible using a block index and a thread index. Blocks are subdivided in groups of 32 threads called warp. When the GPU distributes the threads, it passes them to the multiprocessors as warps. Then all threads within a warp execute the same instruction. The multiprocessor waits until the execution of all threads of the current warps has been done before getting the next warp. If one of the threads diverges, the multiprocessor will wait until that one is ready introducing a penalty in the efficiency.
GPU's have different memories types available to threads. Every thread in a block has access to its own memory register and to a cached memory shared by all threads of the block. Reading and writing of the shared memory is very fast. There is a non-cached global memory available to all threads, of the same block or not, but its access is very slow compared to shared memory (it access latency is approximately 600 clocks cycles). To increase kernels efficiency most of the computation must be perform using shared memory. The register memory, shared memory and global memory are write/read memories. There are other read-only memories available for the threads called constant memory and texture memory.
Finite differences methods are well suited to parallelization in GPU's. We implement a first order in time, fourth order in space finite difference scheme to solve the nonlinear diffusion equation couple to a staggered grid scheme with centered cells for the elastodynamics equations. In both cases the central part of the domain is computed using shared memory and the boundary conditions using global memory.
To implement the poro-elasto-plastic model in GPU we use a modular approach. We subdivide the problem in different kernels that can work independently of the others. We subdivide the problem in six main kernels: computation of nonlinear permeability, computation of nonlinear diffusion 4.11, computation of effective stresses 4.2, computation of velocities 4.3. The computation of poro-elastic stresses 4.1 , yield function 4.6 and plastic strains 4.9 and plastic stresses is realized in one kernel. Finally a last kernel updates the rheological constants, porosity and σ^* constant. Using this modular programing maintenance and further improvements of the code could be implemented easier. Future improvements of our simulation include explicit calculation of porosity and implementation of Gassmann equations for the rheological constants (Gassmann, 1951).

4.5 Fluid injection in heterogeneous fractured rock

First, the effect fluid injection in the vicinity of the borehole in highly fractured rock was modeled. The model is an horizontal rock layer at 5 Km depth with a borehole in the middle. Maximum and minimum principal stresses act horizontal We model a 5 m×5 m squared layer with a borehole in the middle with a diameter of 30 cm.

The numerical grid had 500 × 500 elements for numerical resolution of 1 cm. The pressure of the borehole is increased at rate of 1 MPa per hour from 1 MPa until 99 MPa. Model parameters are presented in Table 4.1.

Parameter	Value	Units	Definition
ρ_r	2540	kg m^{-3}	Rock density
ρ_w	971.8	kg m^{-3}	Water density
K_d	35	GPa	
K_u	41	GPa	
ν_d	0.3		
ν_u	0.27		
φ	30	degrees	Frictional angle
G	18.9	GPa	Shear modulus of the rock
C	20	MPa	Cohesion of the rock
σ_t	10	MPa	Tensile strength of the rock
κ_o^d	10^{-19}	m^2	Intrinsic background permeability for drained rock
κ_o^u	10^{-18}	m^2	Intrinsic background permeability for undrained rock
κ_o^s	10^{-17}	m^2	Intrinsic permeability of shear fractures
κ_o^t	10^{-16}	m^2	Intrinsic permeability of tensile fractures
ϕ_d	0.01		Drained porosity
ϕ_u	0.1		Undrained porosity
ϕ_f	0.1		Fracture porosity
σ_d^*	35	MPa	σ^* for drained rock
σ_u^*	33	MPa	σ^* for undrained rock
σ_f^*	33	MPa	σ^* for fractures
β_f	10^{-10}	Pa^{-1}	Fluid compressibility
β_{phi}	10^{-8}	Pa^{-1}	Pore compressibility

Table 4.1: Parameters, symbols, values and units used for the numerical models. Taken from (Jaeger et al., 2007) and (Miller et al., 2004)

Rock anisotropy was modeled introducing a random variation on the frictional angle around 30 and on the cohesion around 20 MPa. Fracture network creation is achieved by compression applied at the left and right edges. Once the network is formed the stresses are relaxed towards the initial conditions. Figure 4.1 presents some stages in the evolution of the fracture network. Upper row in Figure 4.1 presents the yield function or closeness to failure (dark red is closer to failure). Black dots represent failing points at snapshot time. White circle represents the borehole position. Figure (a), (b) and (c) presents the initial, intermediate and final state of the network during stress relaxation time. Activation of different fractures can be observed. In figure (a) activation of a non-optimal oriented fracture due to heterogeneity is appreciated at the top left side of the borehole. In figure (b) and

(c) this fracture deactivates and new optimally oriented fractures are responsible for the deformation. Highly damaged zone appears between close adjacent fractures. Figures (d), (e) and (f) presents the final state of the stresses σ_{xx}, σ_{zz} and σ_{xz} respectively (here x is the direction of the maximum horizontal stress σ_H and horizontal to the reader and z is the directions of the minimum horizontal stress σ_h and vertical to the reader). Compression was take as negative. The final stress fields are very inhomogeneous but their overall mean values are close to the initial stress states. Localized stressed points with very high compressive stress, up to 350 MPa for σ_{xx}, can be appreciated.These stresses might be too high to be sustained by natural rock. Is important to mention that the influence of damage on the elastic properties of the material was not included in this model. Neither plasticity hardening or softening. This mechanisms could limit the range of the stresses to more realistic ones. Future developments of this code will include these effects.

Figure 4.2 shows the fluid pressure profile (P_f), permeability (κ) and yield function (F) for fluid injection in fractured rock. Snapshot at 10, 30, 50, 70 and 99 MPa injection fluid pressure are presented. At 10 and 30 MPa fluid flow occurs mainly through the adjacent fractures. At 50 MPa, 50% of the initial value of σ_h, hydrofracturing near to the borehole can be appreciated. The damage zone increases the permeability near to the borehole. At lower injection pressures (10 and 30 MPa) the seismic events are more distributed over the whole domain. Many unconnected events occurs within and outside the fractures. At high injection pressures, seismic events circumscribe mainly to the fractures. This can be interpreted as shear failure of the fractures. Figure 4.3 shows stress state at 10, 30, 50, 70 and 99 MPa fluid injection pressure. First row is the stress in the direction of the maximum horizontal stress, σ_{xx}, second row is the stress in the direction of the minimum horizontal stress σ_{zz} and third row is the shear stress σ_{xz}. Diminish of the compressive stresses near to the borehole due to fluid injection are clearly shown.

4.6 Modeling the Deep Heat Mining Project in Basel

The Basel Deep Heat Mining project is latest EGS project brought to operation. It is located in the middle of the city of Basel. Its case is important because is an example of how the induced seismicity drives the operation of an EGS project. The DHM project encompass different factors that make it an example for future EGS projects.

The city of Basel is located in a seismic zone, the Upper Rhein Graben, and suffers from constant seismic events of low magnitude $M_L \leq 2$. A mayor earthquake , magnitude M_L between 6.4-6.9, destructed large part of the city in 1356 (Majer et al., 2007; Häring et al., 2008). Another important factor is location of the project, in this case in the middle of a major city. Although is economically advantageous to place and EGS project near to large populations, it is a risky because the public

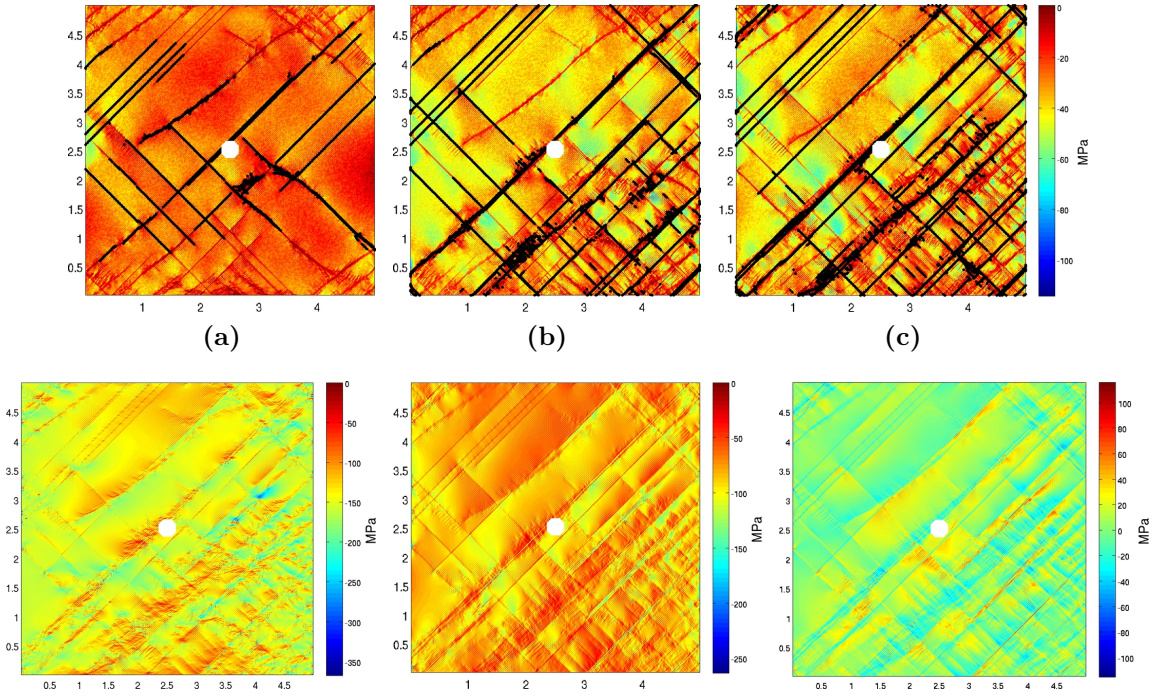

Figure 4.1: Evolution of the fracture network and final stress states. X and Z axis in meters. Resolution 500×500, 1cm. Upper row presents the yield function or closeness to failure (dark red is closer to failure). Black dots represent failing points at snapshot time. We relate these failing points to seismic events. White circle represents the borehole position. Figures (a), (b) and (c) presents initial, intermediate and final state of the network during stress relaxation time. Activation of different fractures can be observed. In figure (a) activation of a non-optimal oriented fracture due to heterogeneity is appreciated at the top left side of the borehole. In figure (a) and (a) this fracture deactivates and new optimally oriented fractures are responsible for the deformation. Highly damaged zone appears between close adjacent fractures. Figures (d), (e) and (f) presents the final state of the stresses σ_{xx}, σ_{zz} and σ_{xz} respectively (here x is the direction of the principal horizontal stress σ_H and horizontal to the reader and z is the directions of the minimum horizontal stress σ_h and vertical to the reader). Compression was take as negative. The final stress fields are very inhomogeneous but their overall mean values are close to the initial stress states. Localized stressed points with very high compressive or extensive stresses can be appreciated.

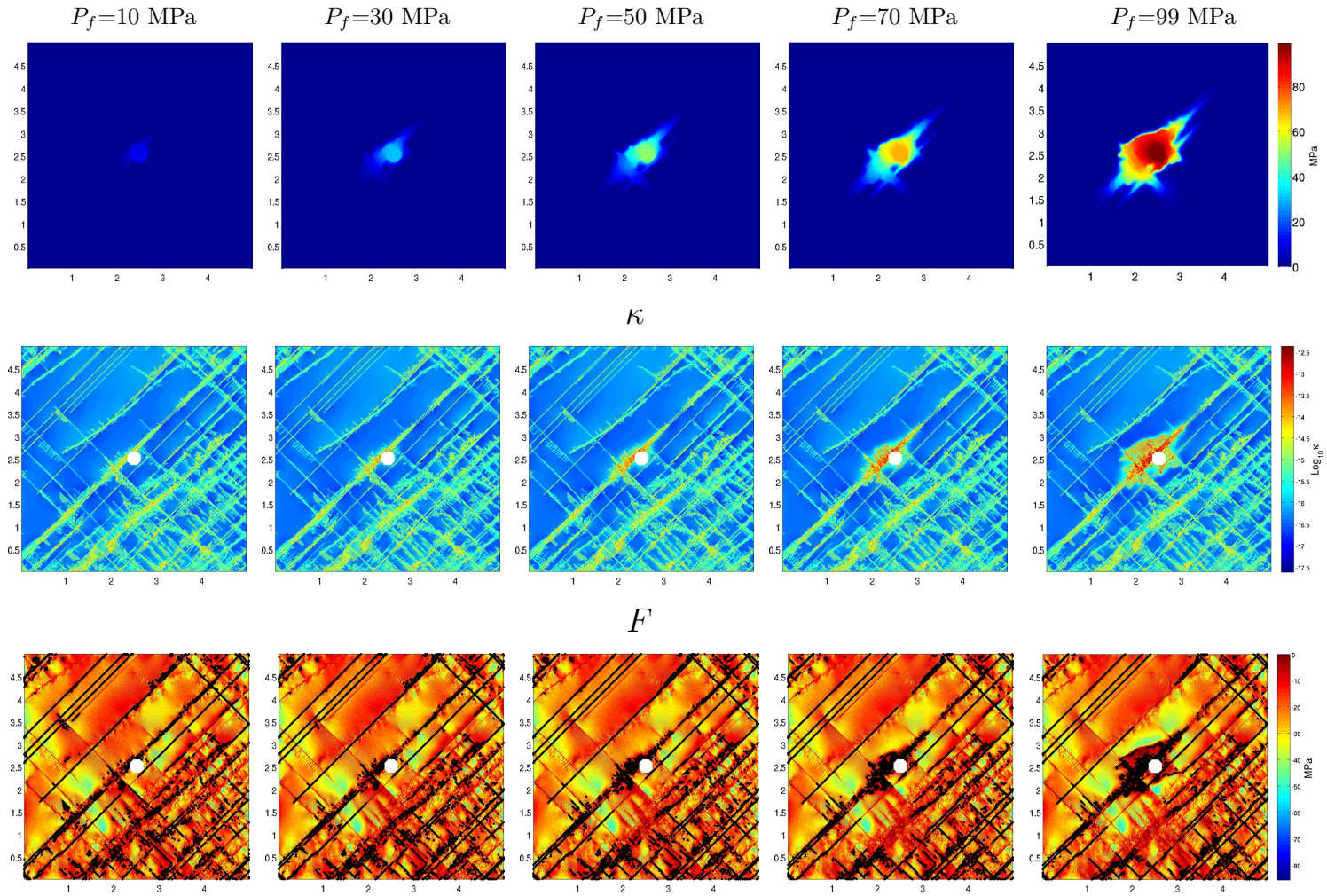

Figure 4.2: Fluid injection pressure (P_f), permeability (κ) and yield function (F)for fluid injection in fractured rock. X and Z axis in meters. Snapshot at 10, 30, 50, 70 and 99 MPa injection fluid pressure are presented. At 10 and 30 MPa fluid flow occurs mainly through the adjacent fractures. At 50 MPa, 50% of the initial value of σ_h, hydrofracturing near to the borehole can be appreciated. The damage zone increases the permeability near to the borehole. At lower injection pressures (10 and 30 MPa) the seismic events are more distributed over the whole domain. Many unconnected events occurs within and outside the fractures. At high injection pressures, seismic events circumscribe mainly to the fractures. This can be interpreted as shear failure of the fractures.

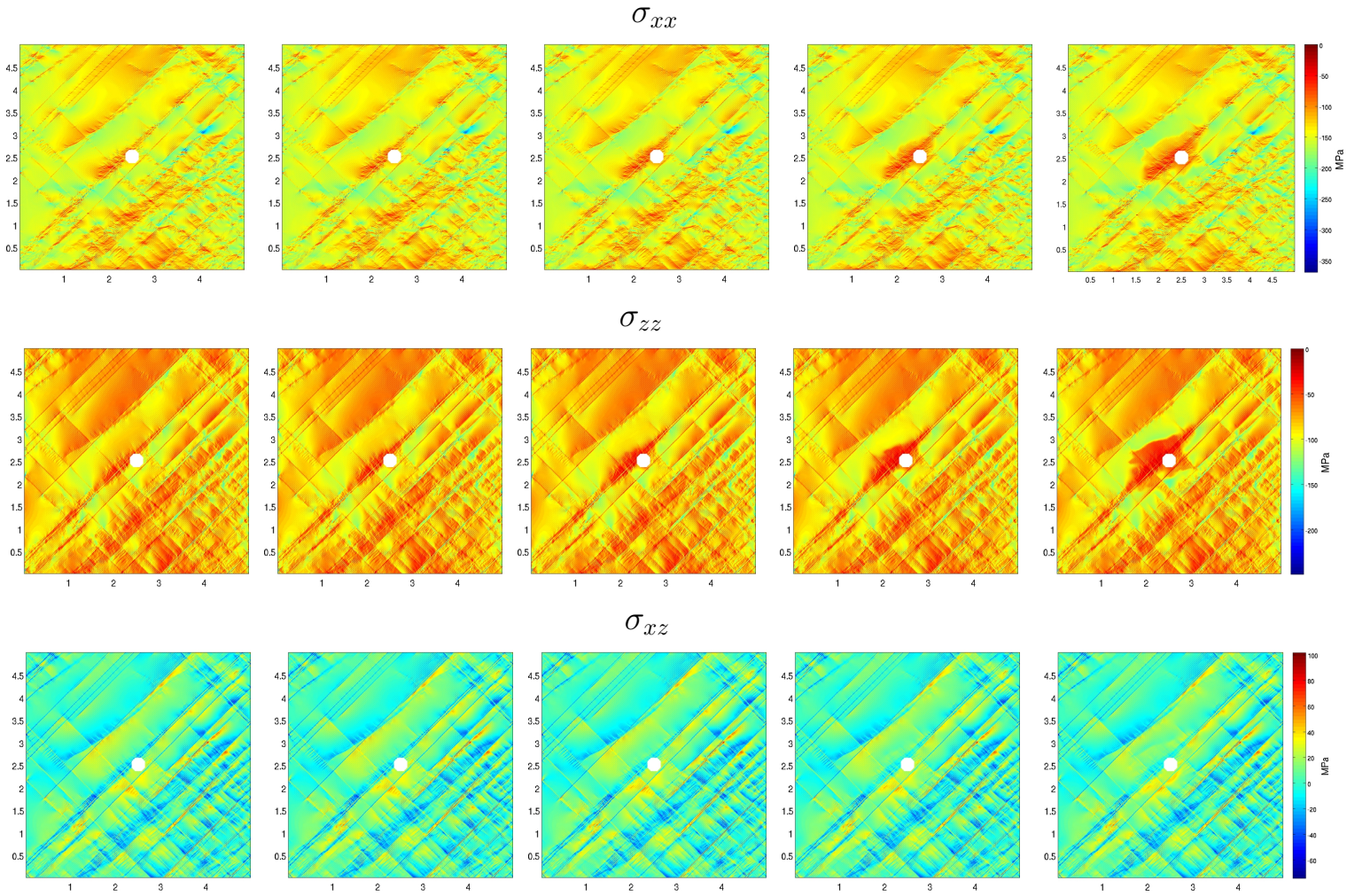

Figure 4.3: Stress state at 10, 30, 50, 70 and 99 MPa fluid injection pressure.X and Z axis in meters. First row is the stress in the direction of the maximum horizontal stress, σ_{xx}, second row is the stress in the direction of the minimum horizontal stress σ_{zz} and third row is the shear stress σ_{xz}.

might be unrested by seismicity. For a large city as Basel, where other industries settle, population might be alarm about the effects of seismicity in other economical activities. Besides, if the population is not directly dependent on the geothermal energy its willingness to accept ground shaking will be low. It is necessary to inform the public about the seismicity risk and expected ground movement. Realistic numerical models might give answers to these questions allowing an more accurate planing and seismic risk management as well as presenting to the public information easy to visualize and understand.

The DHM project gain relevance in December 2006 during it test time due to the triggering of seismic events felt by the population, during approximately two months after it operation start. In fact, the high levels of the seismicity lead the authorities to stop the project just 6 days after the initiation of the water injection. The biggest event had a magnitude of M_L =3.4. The project was canceled in the year 2009.
The Basel 1 well was drilled through 2507 m of sedimentary rocks and 2493 m of granite basement to a maximum depth of 5000 m, with the open hole section beginning at 4629 meters. The diameter of the well in the open section is 8.5 inches or 21.6 cm. We model a layer of 500×500 m at 4800 meters depth.

In Basel area the maximum and minimum principal compressional stresses lays on a plane almost horizontal, i.e., $\sigma_1 = \sigma_H$ and $\sigma_3 = \sigma_h$. The intermediate compressional stress is the overburden, $\sigma_2 = \sigma_V$. The stress ratio $R = \dfrac{\sigma_H - \sigma_2}{\sigma_H - \sigma_2} = 0.36$ was inferred by (Terakawa et al., 2012). With this R value one can choose the initial value of the stresses $\sigma_H = 160$ and $\sigma_h = 65$ at 4800 m depth. Heterogeneities are introduced in the frictional coefficient taking normally distributed values around 0.7 and varying from $0.58<\mu<0.83$ and similarly for the cohesion, taking values around 20 MPa. We model a layer of $500m^2$ because most of the microseismic activity happen within this radius surrounding the free section of the injection well. All other elastic and hydraulic parameters are the same as the ones presented in Table 4.1.

The numerical grid has dimensions 2000×2000 for a numerical resolution of 25 cm. This very high resolution allows us to follow the evolution of the fractured network very accurately. This was near to the maximum resolution possible in our GPU card.

We create a fractured network by compressing the layer till fracturing. Figure shows some snapshot of the fracturing creation process. Figure shows the stress patters after the fracture creation time and the yield function signalizing closeness to fracturing. Initial stresses are recover by relaxing the stresses back to the initial values. During the relaxation time further fracturing is produced. FIGURE shows the fractured network and stresses after the relaxation time. The resulting stress is very inhomogeneous showing fracture localization and critically stressed fractures. However, the mean value of R is around 0.36 fulfilling the initial stress conditions.
round 0.36 fulfilling the initial stress conditions.

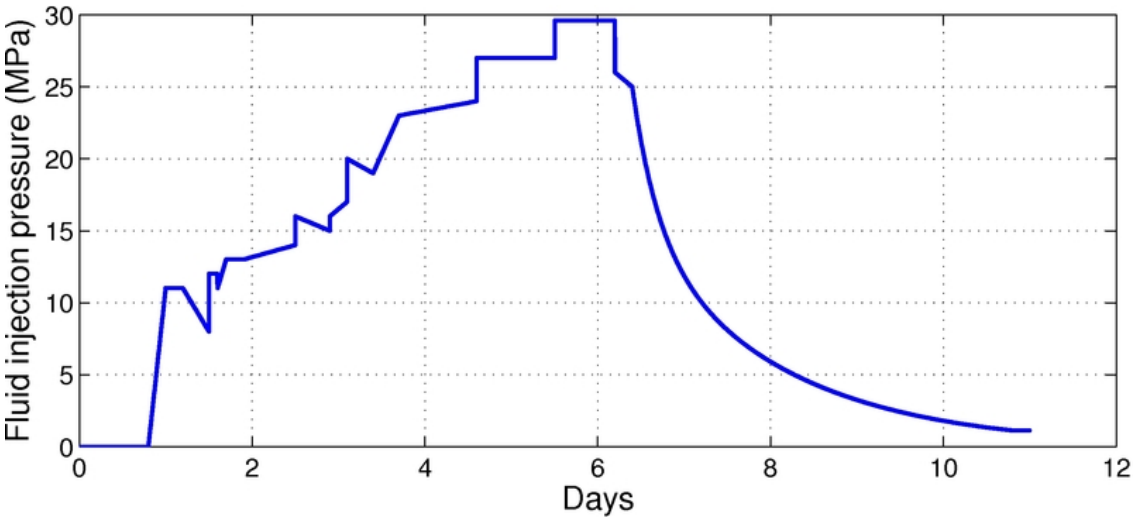

Figure 4.4: hola.

This fractured network with stresses near to initial stresses values is used as the initial condition for the fluid injection model. The injection pressure history for the DHM project is presented in Figure 4.4.

4.7 Discussion and Conclusion

The fact that hydrofracturing is reached at less than 50% of the initial minimum horizontal stress shows that estimations of "safe" fluid injection pressures based in poor fractured or no fractured models might overestimate the injection pressure threshold to avoid seismicity. The Basel DHM project is an example of it where the final planned injections pressure was 79 MPa but the project was suspended 29 MPa.

Even when the induced seismicity in the DHM project could be considered as low magnitude for other seismic zones, for the population as the Base one, its surpassed the tolerable limits. It is worth to notice that if clear information about the disadvantages, triggered seismicity for example, is not share with the population it will be more reluctant to it. Estimates of the induced seismicity limits could come from realistic models as the one presented before.

4.8 Acknowledgments

We thank the German Research Foundation, Deutsche Forschungsgemeinschaft (DFG) for the financial support through the project no. MI 1237/2-1.

Chapter 5

A poro-elasto-plastic model to simulate earthquake-volcano interaction dynamics in Central Chile

5.1 Abstract

The mechanism by which volcanoes respond to large magnitude earthquakes is still standing as one of the main question marks in geosciences. One possible explanation is a link to megathrust earthquakes whereby co- and post seismic volumetric expansion of the upper plate facilitates the vertical migration of deep fluids. To study how the 2010 M8.8 Maule earthquake, Chile, affected the nearby volcanic arc, we developed a poro-elasto-plastic model of the upper continental crust. The model includes the dependence of the permeability on the normal stresses in which each seismic phase affects the fluid mobilization. Our simulations show how the post-seismic volumetric expansion of the upper crust alters the overall geological system, inducing creation and unclogging of fractures and promoting vertical migration of deep fluids. We provide an explanation of the time lap between megathrust earthquakes and volcanic eruptions base on the constrains that poro-elasto-plastic effects impose on the crust permeability and the fluid mobilization through fractures.
In this study we use the new GPU based code named eFrackTurbo to simulate the fluid-rock interactions related to earthquakes triggered volcanic eruptions.

5.2 Introduction

Volcanic response to seismic activity is a very well know phenomenon. Charles Darwin described activity of different volcanoes following the 1835 M8.5 Conception earthquake, Chile (Darwin, 1840) . Cases of seismically induced volcanic activity with varying time- and space-scales has been reported around the globe (Eggert and

Walter, 2009). Examples of volcanic activity induced by large magnitude earthquakes occurred in the USA (Sanchez and McNutt, 2004), Kamchatka (Walter, 2007), Japan (Koyama, 2002), and Italy (Sharp et al., 1981; Nostro et al., 1998; Nercessian et al., 1991). Volcanic activity can be triggered by dynamic or static stress variations. The first operate over short (hours to days) timescales while the second over long (months to years) timescales. The perturbation of the system induced by dynamic and stress triggering can reach $1/r^{1.66}$ and $1/r^3$, respectively, where r is the distance from the earthquake epicenter (Hill et al., 2002).

Cases of induced volcanism over short timescales are, for example, documented in Kamchatka and Chile. Following the 1952 M9.0 Kamchatka earthquake (Johnson and Satake, 1999) the Karpinsky and the Tao-Rusyr volcanoes began to erupt one and seven days after the main shock, respectively (Walter and Amelung, 2007). Evidence of volcanic activity following the M8.1 1835 Concepción, earthquake (Darwin, 1840; Lara et al., 2004) includes eruptions of the Minchinmavida and Cerro Yanteles volcanoes less than 24 hours after the main shock (Darwin, 1840). Similarly, the Cordon Caulle volcano erupted less than two days following the M9.5 1960 Valdivia earthquake (Lara et al., 2004). Other examples are the volcanoes Talang, Frafatoa and Tangkubanparahu in Indonesia that erupted two days after a M6.7 aftershock approximately three months after the December 26, 2004, M9.3 Sumatra earthquake(Manga and Brodsky, 2006). Several mechanism have been suggested to explain the dynamic propagation of stress. For instance, (Walter and Amelung, 2007) suggest that at short (elastic) timescales, large slip on the subduction interface induces volumetric expansion in the upper plate, leading to magma mobilization (Amelung et al., 2007). Moreover, the passage of body and surface seismic waves (Hill et al., 2002; Walter and Amelung, 2007) can induce processes such as rectified gas diffusion (Manga and Brodsky, 2006), which will ultimately enhance upwelling of deep fluids and volatile exsolution (Sparks and Sigurdsson, 1977; Manga and Brodsky, 2006).

However, the time lap between earthquakes and volcanic activity can extend to years dependent on the hypocentral distance to the volcanic system (Eggert and Walter, 2009). For example, a M8.3 subduction earthquake in 1923 in Far East Russia triggered volcanic activity in Kamchatka with many different volcanoes erupting: two in 1923, one in 1925, two in 1926, and one each in 1927, 1928, 1929 and 1930. Similarly, (Eggert and Walter, 2009) points out that the 1928 M7.6 Talca earthquake, Chile, was followed by large eruptions of the Quizapu-Cerro Azul (1932) and Dezcabezado Grande (1933) volcanoes, which reside along the arc directly behind the Talca earthquake epicenter.

These megathrusts earthquakes induce static stress variations that can lead to crustal deformation that relax the pre-earthquake regime (Eggert and Walter, 2009) and initiate long-duration extensional or transtensional tectonic regimes (Walter and Amelung, 2007) finally leading to permanent changes in the state of the volcanic systems. This would explain the time gap of months to years between earthquake and

volcanic eruption. This mechanism is generally acknowledged and state-of-the-art modeling uses Coulomb stress transfer analysis to investigate post-seismic stress distribution (Toda et al., 2005; Walter and Amelung, 2007). When Coulomb stress analysis is performed in these settings, normally the effects of overpressured fluids is "included" using very low frictional angles, around 20 (Toda et al., 2005; Walter and Amelung, 2007). However, fluid-rock effects, hydrofracturing for example, cannot be taken into account using Coulomb stress transfers. These effects will ultimately affect the volcanic plumbing system. We use a poro-elasto-plastic model that includes fracture formation and propagation and stress dependent permeability to simulate earthquake-volcano interaction in Central Chile.

5.3 Geodynamic setting

The M8.8 Maule earthquake of February 27, 2010 ruptured the Concepción-Constitucion gap. Figure Figure 5.1 shows the volcanic arc, the main regional faults, and the direction of subduction of the Nazca plate underneath the South American plate. It also shows the epicenter, the slip, and the focal mechanism (strike = 18°S, dip = 18°S (USGS, 2010)) of the Maule earthquake as well as the reference point that we assumed for calibrating our model with the GPS surface velocities. It stroke at 35 km depth and ruptured laterally for more than 100 km and extended approximately 500 km parallel to the coast. Preliminary analysis performed with Coulomb (Toda et al., 2005) showed that Coulomb stress variation of up to 1 MPa can be reached for optimum-oriented fault planes (i.e. direction N25 that is approximately the direction of the arc in this region, dip 90°, rake 180 °, source depth 35 km and friction 0.40) in the arc. The ongoing seismic activity in the arc is dominated by a transpressional component with the direction of σ_1 subparallel to the direction of subduction (Cembrano and Lara, 2009).

5.4 Two-dimensional model

5.4.1 Conceptual model

Figure 5.2 shows the conceptual model that simulates the long-term earthquake-volcano interaction in the South American plate. We consider the continental crust underneath the volcanic arc from 1 km to 11 km depth and used eFrackTurbo to simulate the evolution of this region during the loading (inter-seismic) and relaxing (post-seismic) state of the Maule earthquake. Our simulations are calibrated with the GPS velocities recorded at approximately S36° (blue square in Figure 5.1 during inter-seismic (Moreno et al., 2010; Vigny, 2011), and post-seismic times (SEO20011, 2011). At 10.75 km depth, the model domain is divided by a transition which represents the limit between the upper crust (9.75 km thick white area in the squares of Figure 5.2) where fluids are pressurized at hydrostatic pressures and the lower crust (0.25 km thick black area at the base of the squares of Figure 5.2) with overpressurized fluids at pressure equal to lithostatic. We also assume that the system

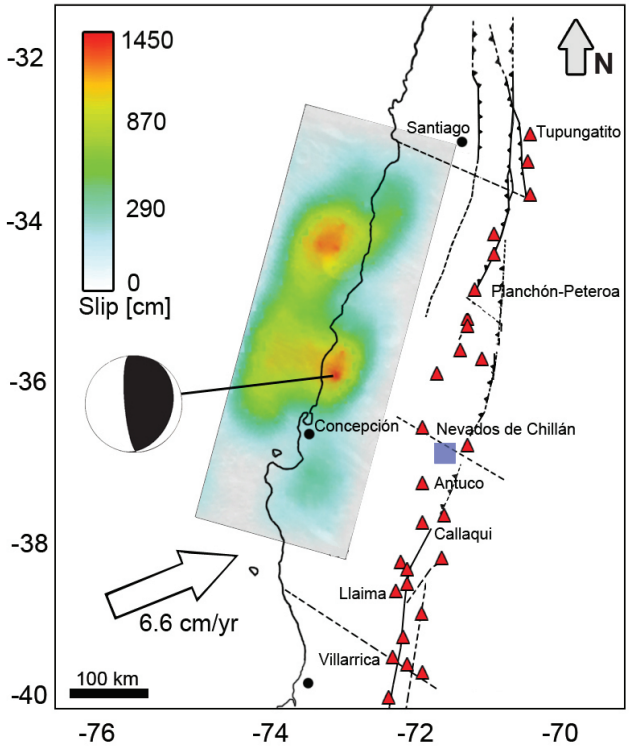

Figure 5.1: Geodynamic setting of Chile between 32°S and 40°S. The colour bar indicates the magnitude of the slip of the Maule earthquake and the arrow shows the subduction direction of the Nazca plate underneath the South American plate. The epicenter of the M8.8 Maule earthquake was located along the plate interface offshore of the Maule region (35.909°S, 72.733°W, 35 km depth) (USGS, 2010). The rupture exceeded 100 km in width and spread northwards and southwards simultaneously for more than 500 km. The maximum slip along the fault was as large as 9 m. The triangles mark the position of volcanic systems and the blue square indicate the reference point for the surface GPS velocities. Reverse, strike slip and ancient (inherited) faults are marked by jagged, solid, and dashed lines, respectively.

is compressional with σ_1 horizontal and σ_3 is given by the overburden.
Figure 5.2 illustrates the conceptual model of this study. The right column shows the geodynamic state of the subduction zone and the left one shows the variation of the far field stress states during the model. In particular, Figures 5.2a and 5.2b refer to the inter-seismic state during which the system is in compression and the subduction is locked. This convergent setting is simulated to reproduce the approximately 175 years that separate two different megathrust earthquakes. At this time, the GPS surface velocities in the arc point Westwards and are approximately 1.125 cm yr^{-1} (Moreno et al., 2010). As the subduction goes on, σ_1 can locally increase leading to rock fracturing and fault failure (Figure 5.2b). Figure 5.2c shows the co-seismic state during which the Nazca plate suddenly slides underneath the South American plate. The maximum horizontal displacements recorded at the time of the earthquake nearby Concepcion is 4.7 m while in the arc it reached ∼50 cm (Vigny, 2011). This translates to a sudden reduction of σ_1 and to a general relaxation of the system 5.2e. This volumetric expansion in the upper lithosphere underneath the volcanic arc that leads to a permeability increase and fracture uncloging or creation which ultimately facilitates the upwelling of deep fluids. Upwelling of fluids will increase the fluid pressure at depth, reducing the normal effective stress required to failure then promoting further failure, 5.2f.

5.4.2 Numerical model

We use a new GPU based software named eFrackTurbo. eFrackTurbo is a poro-elasto-plastic simulator for lithostatic models that includes nonlinear stress dependent permeability and is specially designed to allow creation of fractures and to follow their evolution. eFrackTurbo solves the elastodynamics equations in their velocity-stress representation coupled with a nonlinear diffusion equation for the pore fluid pressure using explicit finite difference methods. It make use of the GPU parallel architecture to do high resolution computing in a very fast and efficient way. In our particular case, the model domain of 10×10 km is subdivided in a grid of 300×300 elements given a resolution of 33 meters for each finite difference cell.

We model the continental crust below the volcanic arc as a heterogeneous fractured rock. heterogeneities are introduced in the inital values of the frictional angle using values normally distributed around 35 and in the cohesion taking random values around 10 MPa. The elastic parameters are allow to change due to saturation or fracturing. In order to simulate strain weakening, the cohesion of the fractures is set to zero. The elastic properties, bulk modulus and Poisson radius evolve between the prescribed values for the drained and undrained cases. Here the drained values refers hydrostatic pore fluid pressure. For the bulk modulus we use K_d= 35 GPa and K_u=41 for the drained and undrained rock and Poisson's ratio ν_d=0.3 and ν_u=0.27. Crust density is 2700 kg m^{-3}. The value of porosity was 1% for undrained rock and 10% for undrained. The fluid pressure equation is similar to (Miller et al., 2004) (see appendix). The values of the intrinsic permeability, permeability at zero normal stress, are set to $\kappa_o^d = 10^{-19}$ m^2 for the drained rock, $\kappa_o^u = 10^{-18}$ m^2 for undrained

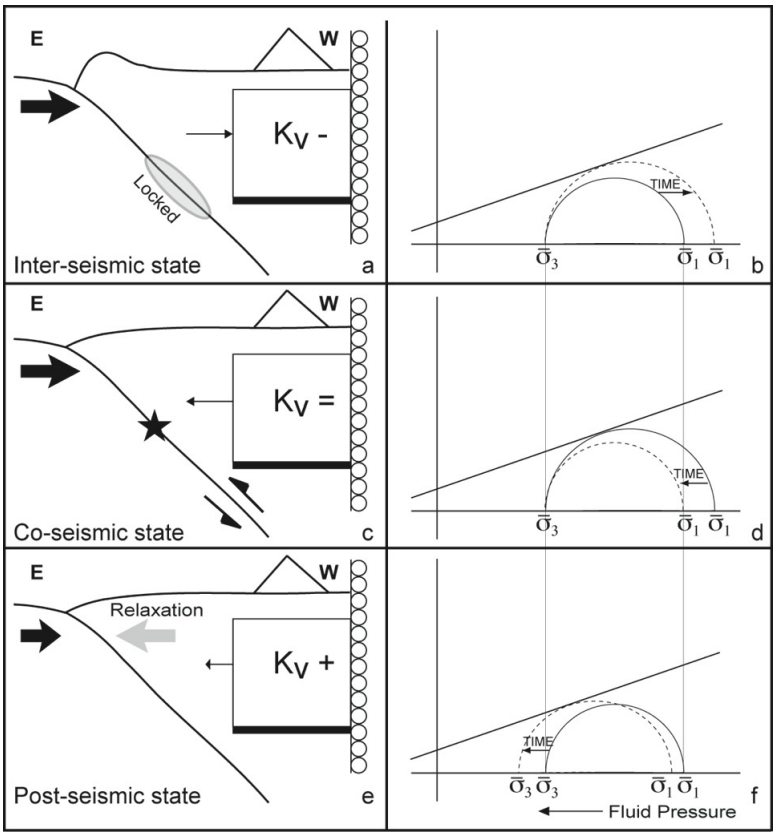

Figure 5.2: Conceptual model (not to scale) of the simulation cycle. First, second, and third row show the inter-seismic, co-seismic, and post-seismic state, respectively, undergone by the upper crust of the South American plate over approximately two centuries. The squares in the left column represent the region of continental crust simulated in this study. K_v indicates the increase or decrease of permeability throughout the simulations. The vertical line of circles indicates that the right boundary is fixed while the left black arrows on the left boundary indicate whether the system is in compression or extension. The length of the arrow is proportional to the GPS surface velocities.

rock, $\kappa_o^s = 10^{-17}$ m^2 for shear fractures and $\kappa_o^t = 10^{-16}$ m^2 for tensile fractures. The permeability is a strong increasing function of the normal stress weighted by a constant related to the degree of fracturing of the rock σ^* that takes values of 90 MPa and 87 MPa for the drained and undrained case. Fluid and pore compressibilities are $\beta_f = 10^{-10}$ and $\beta_{phi} = 10^{-8}$ respectively.

The boundary conditions for the diffusion equations are zero flux boundary conditions at top, right and left edges and P_f= lithostatic at the bottom. The initial value of the far filed stresses are σ_3 = overburden and $\sigma_1 = 2.3\sigma_3$ representing an compressive environment.

The velocity boundary conditions are adjusted according tho the GPS velocities for the inter-seismic and post-seismic times given by 1.125 cm·year^{-1} in compression and 20·cm year^{-1} in extension. These velocities are apply at left edge of the domain as the boundary condition of the horizontal velocity profile, i.e. v_x^l =GPS velocities, while the horizontal velocity in the right side is kept constant and equal to zero $v_x^r = 0$.

First a fracture network is generated by compressing the domain with a velocity of v_x^l =25 cm·year^{-1} and v_x^r =2.5cm·year^{-1}. This network develop following the far-field stress and the local stresses. During the fracture network creation stage the compressive stresses rises at values far from the initial conditions. To regain stresses near to the initial values, stresses are relaxed by stopping the fast compression and imposing the initial stress values at the boundaries. During the relaxation time the rock suffers further fracturing leading to formation of complex fracture networks.

In these way we introduce multiscale fracturing to simulate the complex faulting developed during millions of years. During the fracture creation and relaxation stages the fluid pressure diffusion is kept locked. At the end of the relaxation time the cohesion of the fractures is set to 10% of the background cohesion to model the healing of fractures. This fracture network and its correspondent inhomogeneous stress field were used as the initial condition for the simulation of the inter-seismic regime.

Figure 5.3 shows different stages of the fracture network development and relaxation time. The first row Figure 5.3 presents the yield function, F, and the seismic events. The yield function F represent the clossnes to failure. Failure occurs when F=0 (dark red is closer to failure). Black dots represent the failing point at snapshot time. Creation of new fractures and activation of preexisting ones can be appreciated. Second, third and fourth row represent the stresses in the horizontal direction (σ_{xx}), vertical direction (σ_{zz}) and shear stress (σ_{xz}). Stress relaxation can be appreciated. The complex fracture networks create areas with high localized stresses in the verge of failure. The dark red layer at the bottom represent the overpressurized fluids at lihostatic pressure in the lower crust

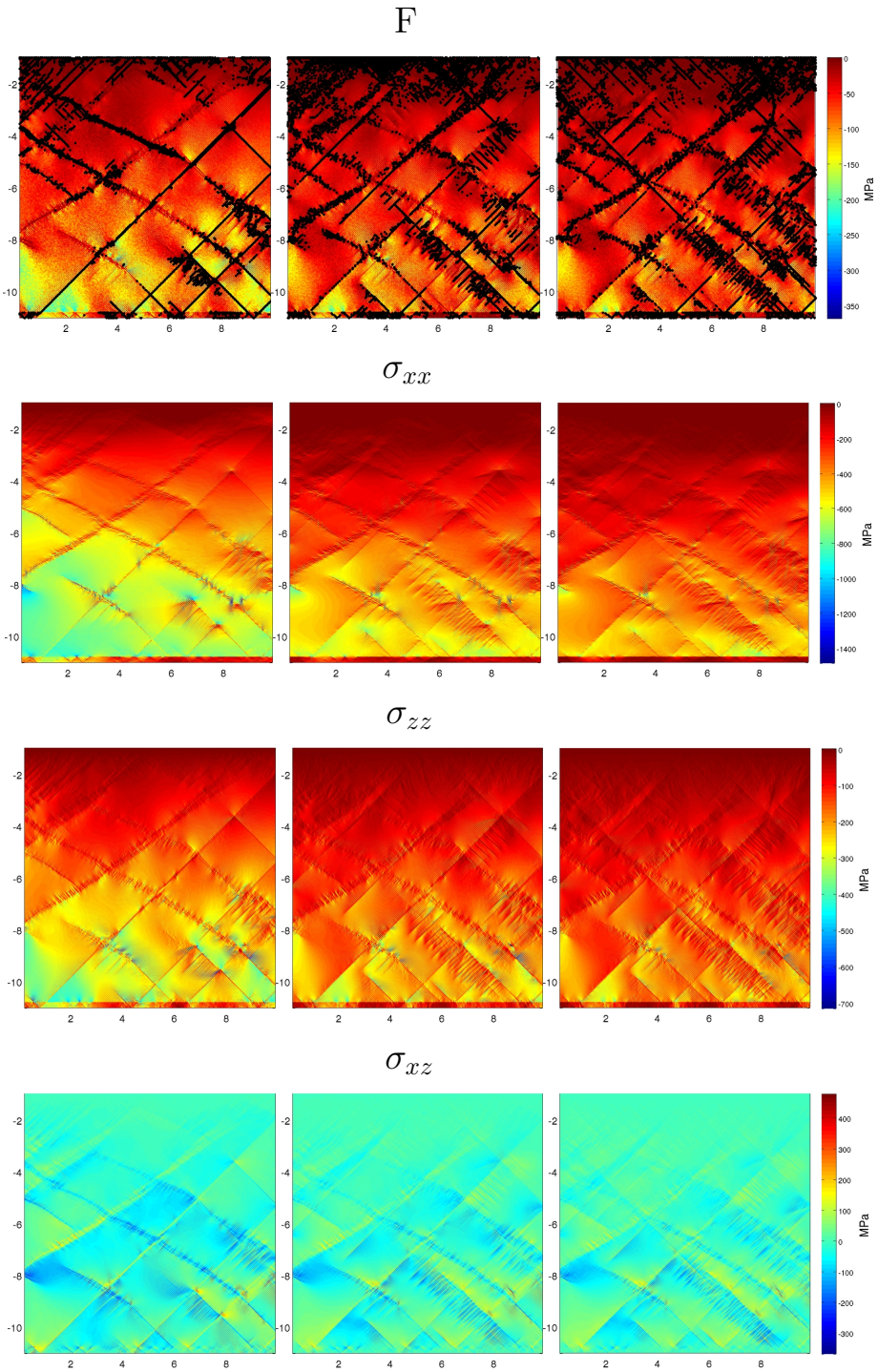

Figure 5.3: Yield function F, seismic events and stress tensor at the initial, intermediate and final stage or the relaxation time. Yield fundtion F represent the clossnes to failure. Failure occurs when F=0 (dark red is closer to failure). Black dots represent the failing point at snapshot time. Creation of new fractures can be appreciated. Second, third and fourth row represent the stresses in the horizontal direction (σ_{xx}), vertical direction (σ_{zz}) and shear stress (σ_{xz}). Stress relaxation can be appreciated. The complex fracture networks create areas with high localized stresses in the verge of failure. The dark red layer at the bottom represent the overpressurized fluids at lihostatic pressure in the lower crust.

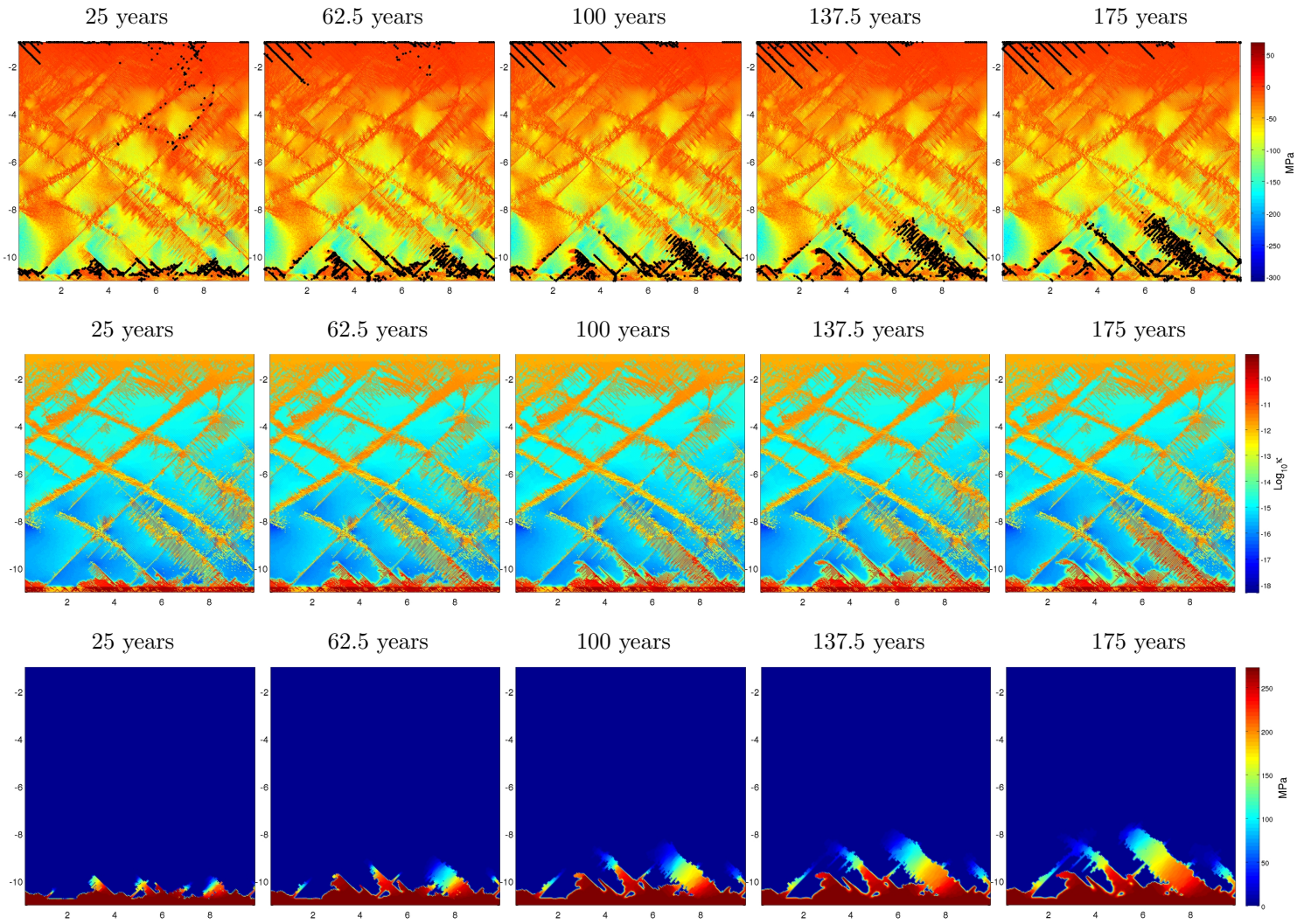

Figure 5.4: compression

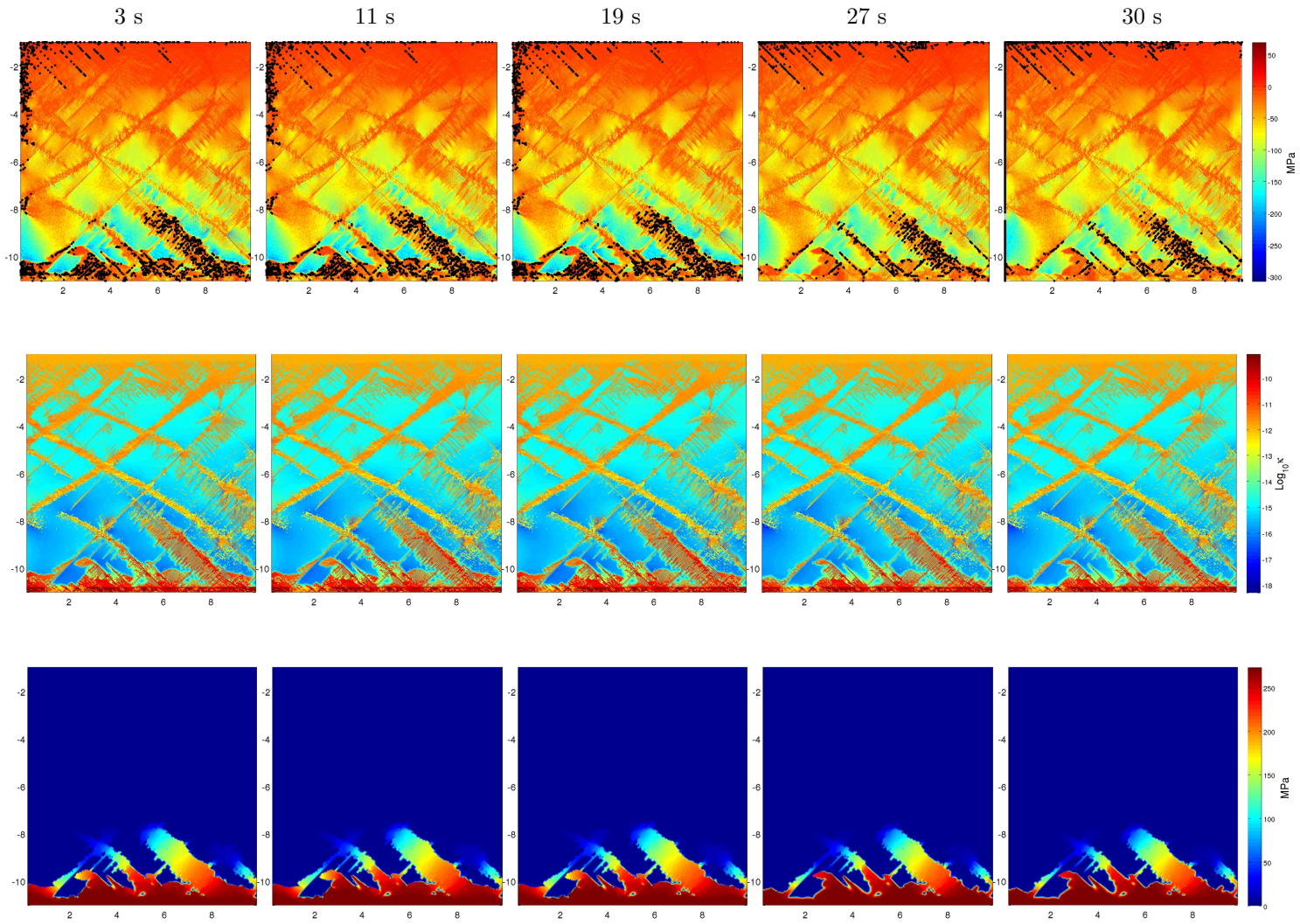

Figure 5.5: earthquake

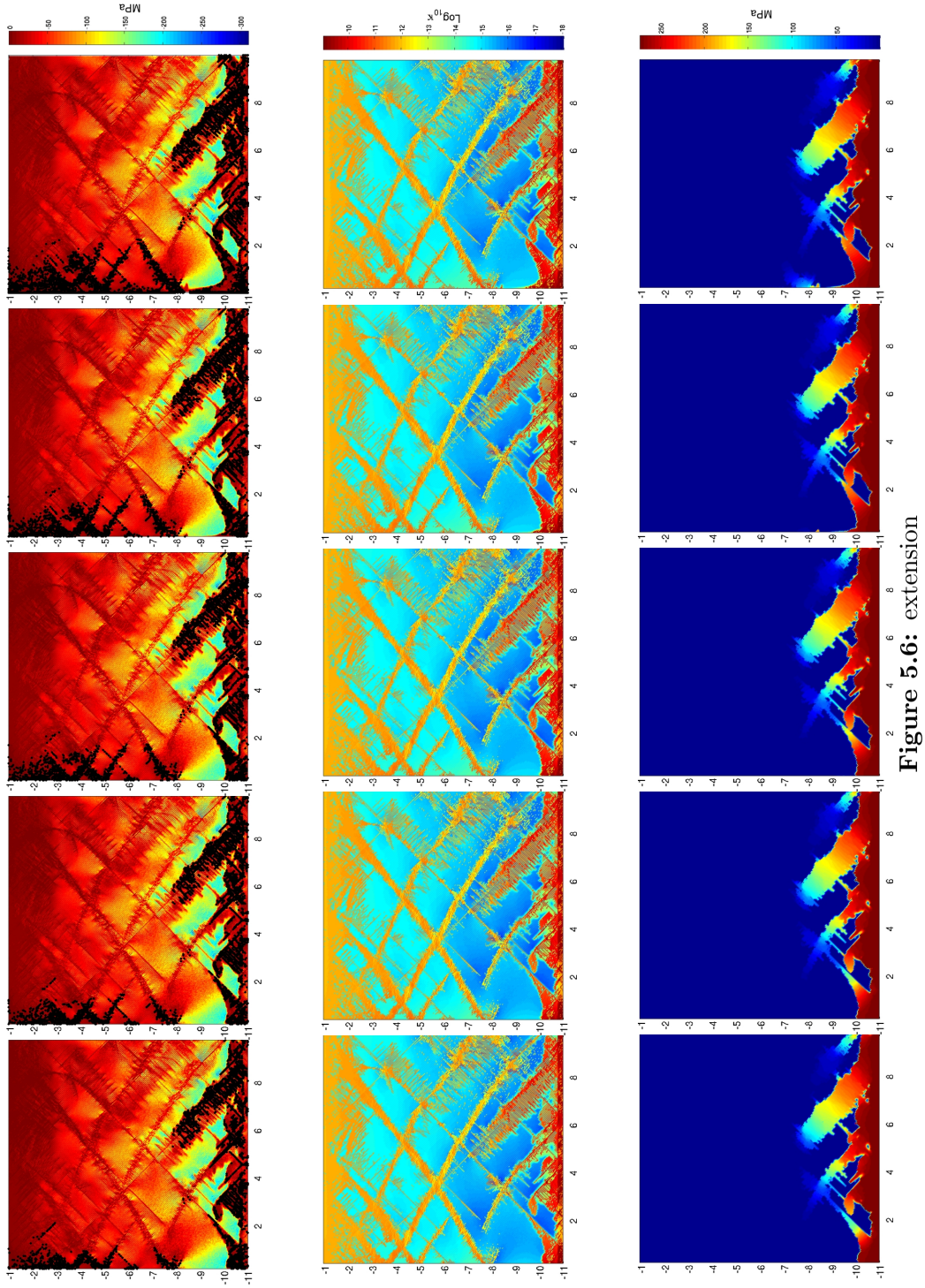

Figure 5.6: extension

5.5 Conclusions

Earthquake volcano interactions in the central part of Chile were modeled using a poro-elasto-plastic model with stress dependent permeability for the pore fluid pressure difusion equation. The results shows that post seismic expasion enhance fluid mobilization through fracture channels. The reduction in the normal stress leads to a increase in the permeability of the fractures. Fluid promotes more fracturing allong the low paths which induce more fluid mnobilization. The sudden increase of the permeability coupled to further fracturing results in very fast upwards flow.

Future developments of this model will include the simulation of the co-seismic regime and the effects of seismic waves and dynamic stresses. These effects of the slipping are significant because fracture aperture and faster fracture grow are realted to it.

5.6 Acknowledgments

I thank Dr. Matteo Lupi for it help in discussion and geology remarks used in the present work. We thank the German Research Foundation, Deutsche Forschungsgemeinschaft (DFG) for the financial support through the project no. MI 1237/2-1.

Part III

CONCLUDING REMARKS

Chapter 6

Concluding Remarks and Future Work

Many different phenomena of lithospheric geodynamics can be described by fluid-rock interactions. These interactions are complex across multiple scales in time and space, and powerful numerical techniques must be developed to capture this multi-scaled problem. However, these techniques demand equally expensive computational resources, limiting in many cases their widespread application. CPU clusters have been the main tool to deal with high resolution simulations introducing another limiting factor as the high level of expertise required to program these complex numerical models in a physically correct way on this architecture. Despite the vast improvement of CPU technology, most of the current numerical models are still simulated in relatively low resolution. From the point of view of CPU computing, there has not been a significant advancement in routine scientific modeling in the last 20 years. Low resolution models, even when they encompass sufficient physics, may lead to inaccurate results because of the numerical limitations. Limited resolution of numerical models have similarly limited application to real world problems, and high resolution computing is regarded by many as merely and optimization issue.

I have presented simulations of hydro-mechanically coupled systems with very different time and space scales from numerical simulation of laboratory experiments, applications to geothermal systems and for larger scales models of fluid mobilization related to aftershocks triggering, with time scales ranging from some minutes to months and years. The multiscality problem can be handle at high resolutions in an efficient way. For the laboratory experiments simulation length scales in the range of tenths of millimeters were achieved while in the fluid mobilization experiments, where the total scales is in the range of kilometers, resolutions of meters were possible. The range of possible length scales is up to three orders of magnitude. In time scales a difference up to six orders of magnitude is possible. This large range of resolutions allows to develop software tools that have a real applicability for real world problems and it allows to study very complex dynamics in details.

The numerical codes were benchmarked comparing the results of shear fracture for-

mation experiments with other elastoplastic codes. The Method of Manufactured Solutions (MMS) was used to benchmark the non-linear diffusion model. Solutions for the elasto-plastic part of the code shows excellent agreement with other reports (Poliakov et al., 1994; Kaus, 2010; Popov and Sobolev, 2008; Hansen, 2003). Using MMS for the nonlinear diffusion part the GPU code gives exactly the same solution as the CPU code. The results presented in this thesis are the first implementation of Poro-elasto-plastic media in GPU and, to the best of our knowledge, this is one of the few numerical codes that can follow the creation and evolution of fracture networks in geo-materials. Due to the increment in speed and resolution of GPU based codes is possible to model a manifold of systems with the same code without any major change.

The baseline code presented here sets the basis for many future improvements and developments, including its extension the 3D. In terms of physics, an improved treatment of porosity creation and destruction, and changes in hydraulic and elastic properties is to be explored. Damage effects on elastic properties have so far been ignored, while thermo-elasticity should be introduced to extend this model to a more realistic simulator of geo-thermal systems.

A future and systematic and focused study should be performed to investigate the optimal approach to handling the complex properties of permeability in relation to porosity, strain, frictional or tensional failure, or how permeability is influenced by effective normals stresses or crack aperture. The results of these studies will establish the optimal algorithmic approach for computational efficiency and physical accuracy.

The source term in the nonlinear pore fluid diffusion equation might be important for large earthquake modeling. Heating of the fault plane may induce decarbonization reactions in the fault and trapping high pressure fluids that promote additional slip (Madariaga, 2007; Paola et al., 2011). In geothermal and volcanic systems the heat effects are essential. To model this is necessary to introduce thermal effects using the advection diffusion equation of heat. The effect of heat on the fluid and on the rock will be introduced in future versions of our code. A full thermo-poro-elasto-plastic GPU model is envisioned.

Another necessary improvement is the 3D implementation of the code. For real applications in EGS or fracking the 3D modeling of the fracture networks is very appealing. Developing a 3D code at the high resolution desired will likely incorporate a GPU cluster in the future, and we are currently working making developments in this direction. The simulation of the Basel geothermal systems presented in this work was computed on a single GPU card. However, we present results with a very high resolution, of just 25cm per cell, and a large simulation domain of 500 m, i.e. a grid of 2000×2000. The utilization of GPU cluster to compute a the 3D model promises very high resolutions too.

Further, calibration of the model and quantitative comparisons to experiments is

necessary.
Visualization of high resolution results, in particular for the 3D implementation, will require a graphical interface. Part of our future work is to complement this code with pre-processing and a post-processing tools. The goal in to have a fast and easy to use software for thermo-hydro-mechanical modeling.

High resolution modeling opens the possibility of following the evolution of the coupled systems and accurate modeling can be performed. Faster numerical models that include all of the underlying physics has always been the goal in geodynamical numerical model. GPU technology allows faster simulations at higher resolution, while not sacrificing the physical processes being simulated. The work presented here is another step in the development of such numerical codes.

My personal view is that the future in scientific numerical modeling, irrespective of the area under study, will require faster and high resolution codes, where resolution and speed are not just optimization issues but limiting factors in unveiling the underlying physics. GPU technology might provide a solution for this problem.

Appendix

Geology

High-pressure fluid at hypocentral depths in the L'Aquila region inferred from earthquake focal mechanisms

Toshiko Terakawa, Anna Zoporowski, Boris Galvan and Stephen A. Miller

Geology 2010;38;995-998
doi: 10.1130/G31457.1

Notes

High-pressure fluid at hypocentral depths in the L'Aquila region inferred from earthquake focal mechanisms

Toshiko Terakawa*, Anna Zoporowski, Boris Galvan, and Stephen A. Miller
Geodynamics/Geophysics, Steinmann-Institute, University of Bonn, Nußallee 8, D-53115 Bonn, Germany

ABSTRACT

We apply a new analysis technique using earthquake focal mechanisms to infer the 3-D fluid pressure field at depth in the source region of the A.D. 2009 L'Aquila earthquake/aftershock sequence. The technique, termed focal mechanism tomography, inverts for fluid pressure by examining the fault orientation relative to the regional tectonic stress pattern. We identify three large-scale pockets of high fluid pressure (up to 50 MPa above hydrostatic pressure) at depths of 7–10 km that strongly correlates with an independent data set of well-located foreshocks and aftershocks. The shape of overpressured regions and the evolution of seismicity indicate a plausible scenario that this sequence is being driven in part by the poro-elastic response of trapped reservoirs of high-pressure fluid, presumably CO_2, and postseismic fluid flow initiated by the main shock.

INTRODUCTION

A subducting carbonate platform beneath Italy provides a continuous supply of deeply derived CO_2 to the region (Frezzotti et al., 2009). This CO_2 is likely transported from depth via ductile flow mechanisms (Connolly, 1997), and escapes via volcanism or diffuse degassing, or is trapped at depth. Diffuse degassing is observed over large regions of Italy (Chiodini et al., 2004; Rogie et al., 2000), with the Apennines representing an approximate boundary separating regions of diffuse degassing in the west and regions of nondegassing in the east. Large earthquakes and extensive seismic sequences have correlated with this boundary, including the 6 April 2009 L'Aquila intraplate earthquake (M_w = 6.3) in the central Apennines (Anzidei et al., 2009; Walters et al., 2009; Cirella et al., 2009) and the 1997 Colfiorito earthquake sequence to the north (Collettini and Barchi, 2002). The Colfiorito sequence was shown through modeling to be driven by degassing of a high-pressure fluid source at depth (Miller et al., 2004), indicating that similar fluid-driven processes are also acting in the tectonically and geologically analogous L'Aquila region.

The focal mechanism (Fig. 1) of the L'Aquila earthquake, with a hypocentral depth of ~9.5 km, is close to pure normal type with a strike of 135°, a dip of 55°, and a rake angle of –95°, consistent with the extensional tectonics active in the central Apennines since the Pliocene (Walters et al., 2009). The main shock was preceded by a long sequence of foreshocks beginning in December 2008, including the largest foreshock with M_w 4.0 on 30 March 2009, and followed by more than 10,000 aftershocks.

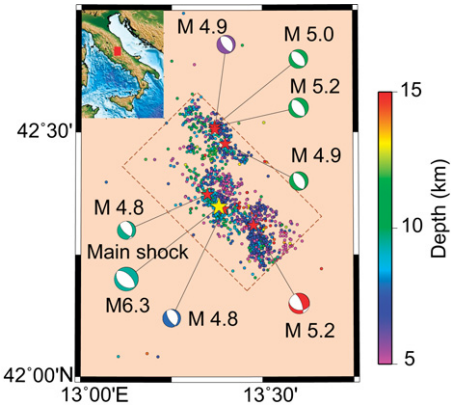

Figure 1. Seismicity in the source region of the A.D. 2009 L'Aquila earthquake (Jan–July 2009). Hypocenters are shown as colored dots. Focal mechanisms of the main shock and large aftershocks are shown with the lower-hemisphere projection of focal spheres. Color of focal spheres and dots indicate depths of hypocenters. Model region is shown by the dashed rectangle.

In the present study, we develop a new data analysis technique, termed focal mechanism tomography, to directly estimate the three-dimensional (3-D) fluid pressure distribution at depth by examining focal mechanisms of seismic events. Here we describe the method and its application to the L'Aquila earthquake sequence and show the 3-D fluid pressure distribution at depth. The results provide strong evidence that this sequence is being fluid-driven.

FOCAL MECHANISM TOMOGRAPHY

The assumptions of focal mechanism tomography (FMT) are (1) that seismic slip occurs in the direction of the resolved shear traction acting on preexisting faults (Wallace, 1951; Bott, 1959), (2) that the fault strength is controlled by the effective normal stress and Coulomb failure criterion with the standard friction coefficient, 0.6 (Byerlee, 1978), and (3) that seismic slip on optimally oriented faults relative to the prevailing regional stress pattern occurs under hydrostatic fluid pressure. Typical studies of stress inversion (e.g., Gephart and Forsyth, 1984; Michael, 1984, 1987) determine a stress pattern from a variety of focal mechanisms based on assumption 1, and attribute focal mechanism variations to different friction coefficients of preexisting faults (e.g., Kubo and Fukuyama, 2004). In our method, we attribute focal mechanism variations to the degree of fault overpressure acting on faults. That is, the orientation of the fault plane (e.g., strike and dip) within the prevailing stress field reflects fault strength (assumption 2), such that

$$\tau_s = \mu(\sigma_n - P_f) \quad (1)$$

where τ_s is the shear strength, σ_n is the normal stress, P_f is the fluid pressure, and μ is the friction coefficient (taken as 0.6). The theory can be explained using a 3-D Mohr diagram (Fig. 2A). The normal and shear stress acting on any plane within a uniform stress field is represented by a point in the region surrounded by the three Mohr circles. The relative position in the Mohr diagram shows the fault orientation relative to the stress pattern. Since seismic slip occurs when shear stress reaches the fault strength, the intersection of the line passing through this point and the normal stress axis shows the fluid pressure P_f. Assumption 3 means that the Mohr-Coulomb failure line under hydrostatic fluid pressure must connect with the largest Mohr circle. In two dimensions, hydrostatic fluid pressure results in slip on optimally oriented faults at 30° from the direction of σ_1 with μ = 0.6. Normal faults have a dip angle of 60°, while unfavorably oriented faults slip at shallower dip angles. Shallowly dipping faults in extensional tectonics have been shown to be reactivated by elevated fluid pressure (e.g., Collettini and Barchi, 2002; Sibson, 1990, 2000; Micklethwaite and Cox, 2006; Cox, 1995).

In three dimensions, orientation is determined from both the strike and the dip, so the strike and the dip determined from focal mechanisms is a measure of misorientation relative to the regional stress pattern (e.g., fluid overpressure). To arrive at fluid pressure, we must first constrain the diameter (deviatoric stress levels) of all circles, the center of the largest

*Current address: Research Center for Seismology, Volcanology and Disaster Mitigation, Nagoya University, Nagoya 464-8601, Japan

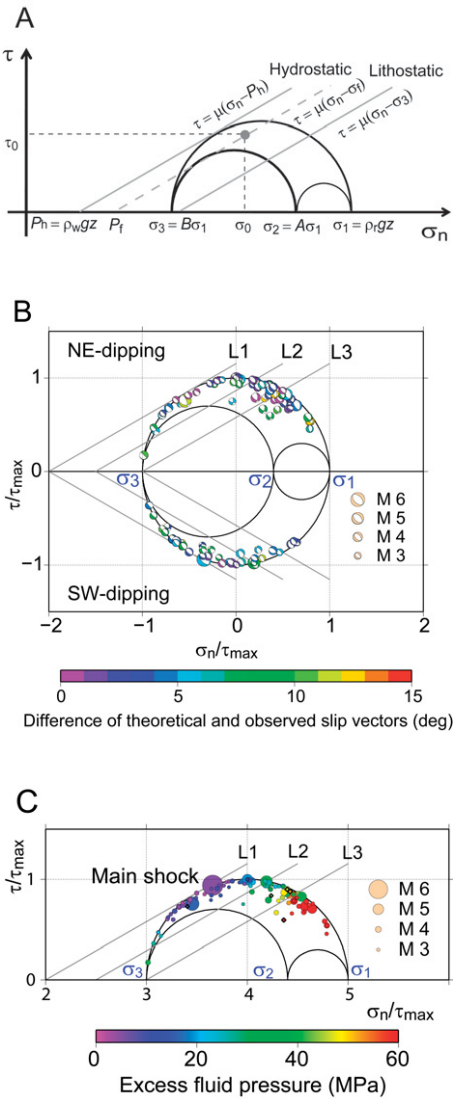

Figure 2. Focal mechanism tomography (FMT) analysis. A: Theory of FMT. Horizontal and vertical axes show normal and shear stresses acting on fault planes. This is an example of extensional stress regime where σ_1, σ_2, and σ_3 are the maximum, intermediate, and minimum compressive principal stresses, respectively. Gray lines show fault strength for hydrostatic, intermediate, and lithostatic fluid pressures. B: Consistency of observed focal mechanisms (CT > 0.975) with the stress pattern. Focal mechanisms are shown in the Mohr diagram (normalized by the maximum shear stress with the lower-hemisphere projection of focal spheres, whose color indicates the misfit angle between the observed and theoretical slip vectors for events. Lines L1, L2, and L3 indicate fault strength under hydrostatic, intermediate, and lithostatic fluid pressures. C: Excess (above hydrostatic) fluid pressure associated with each event. Size of symbol (circles and diamonds represent aftershocks and foreshocks, respectively) scales with magnitude, and color indicates excess fluid pressure. Largest symbol shows the main shock. L1, L2, and L3 are the same as in B.

circle (isotropic stress levels), and the stress pattern. For the extensional central Apennines and the moment tensor solutions of the main shock, we assume that the pattern of the regional stress field is uniformly characterized by normal faulting with $\sigma_1 = \rho g z$ (vertical), $\sigma_2 = A\sigma_1$ (NW-SE), and $\sigma_3 = B\sigma_1$ (NE-SW), where ρ is crustal density (2700 kg m^{-3}), g is gravity acceleration, z is depth, and A and B are coefficients less than 1.0. B is determined by constraining σ_1 as the overburden and using assumptions 2 and 3 to find $\sigma_3 = 0.6\sigma_1$ (B = 0.6). We determine A by performing a series of stress inversions (with a grid-search method) by varying the ratio of the principal stresses, $R = (\sigma_1 - \sigma_2)/(\sigma_1 - \sigma_3)$, to find the most optimal R value that maximizes the sum of the closeness of observed and theoretical moment tensors for the given stress tensor. The closeness of two tensors (e.g., Michael, 1987), which we call CT, ranges from $-1 \le CT \le +1$, with –1 indicating slip in the direction opposite to that expected within the stress pattern, and +1 representing an exact correspondence between observed and expected slip directions. The optimal R value from the inversion is 0.3, from which we find that $\sigma_2 = 0.88\sigma_1$ (A = 0.88). The inversion also discriminates between the true and auxiliary fault planes if we assume that the true fault plane solution is that with the higher CT value. With the stress tensor now constrained, we can determine the shear and normal stresses acting on any plane through Cauchy's relation, $\sigma_n = \boldsymbol{\sigma}\mathbf{n}\cdot\mathbf{n}$, and $\tau = \|\boldsymbol{\sigma}\mathbf{n} - (\boldsymbol{\sigma}\mathbf{n}\cdot\mathbf{n})\mathbf{n}\|$, where $\boldsymbol{\sigma}$ is the (absolute) stress tensor and $\mathbf{n}$ is the normal vector of the fault, and thus the fluid pressure by Equation 1.

RESULTS

We applied FMT to 158 focal mechanisms for the 2009 L'Aquila earthquake sequence (http://www.eas.slu.edu/Earthquake_Center/MECH.IT/). The fault plane for the main shock is constrained by geodetic measurements to be the southwest-dipping fault plane (Anzidei et al., 2009; Walters et al., 2009). Most events in the data set are well explained by reactivation of pre-existing faults under this simple regional stress pattern because the average CT in this data set is 0.945, which corresponds to an average misfit angle of 11.2° between the observed and theoretical slip vectors (Fig. 2B). Our selection criteria for inclusion in the fluid pressure analysis required CT greater than 0.975, which corresponds to an average misfit angle between the two slip vectors of only 5.1°. Focal mechanisms of 122 events (77.2% of the data) have CT greater than 0.975 and fall predominantly on the largest Mohr circle. This indicates that slip occurred at relatively high shear stress levels. Events with low CT values tend to be triggered by significantly lower shear stress (Fig. DR1 in the GSA Data Repository[1]), indicating that slip was not controlled by the regional stress field but more likely by local stress perturbations or very weak fault strength due to over-pressured fluids.

The fluid pressures calculated by Equation 1 (Fig. 2C) show that the main shock occurred at near-hydrostatic fluid pressure, while most of the foreshocks and larger aftershocks occurred at significantly elevated fluid pressures. Moreover, a majority of events occurred below the hydrofracture condition $P_f \le \sigma_3$, consistent with the observed double-couple focal mechanisms. Some events indicate $P_f \ge \sigma_3$, so it would not be surprising if a more detailed determination of focal mechanisms reveals some non-double-couple component. Figure 2C also shows that many of the smaller events occur on optimally oriented faults under hydrostatic pore pressure. However, these events are mostly observed at shallower depths where the generation and maintenance of high-fluid-pressure compartments is more difficult to attain. Events at deeper levels are primarily overpressured, although some lower-pressure events are also observed.

THREE-DIMENSIONAL FLUID PRESSURE FIELD IN THE L'AQUILA REGION

The preceding analysis resulted in 117 discrete measurements of fluid pressure within the model volume. Our interest is their 3-D distribution, so we interpolated between these points by applying the Yabuki-Matsu'ura inversion formula (Yabuki and Matsu'ura, 1992). This formula incorporates a prior constraint on the roughness of fluid pressure field to discrete fluid pressures at points determined from the relocated hypocenters (Chiarabba et al., 2009).

Using this method, we obtained a fluid pressure field as a continuous function defined in 3-D space (Figs. 3A and 3B; Video DR1 in the Data Repository) with estimation errors (in the range of 5–10 MPa, Fig. DR2). Figure 3A shows the calculated excess fluid pressure field as tomographic slices at different depths, superposed on the hypocenters of 467 relocated foreshocks and aftershocks (M ≥ 2.5) within 1 km of each plane. We observe overpressured fluid reservoirs (>40 MPa) at depths between 7.5 km and 10 km, and a very strong correlation between the calculated fluid pressure field and the relocated hypocenters. Because most events do not have focal mechanisms and are therefore not included in the analysis (Fig. DR3), the hypocenters of aftershocks within the calculated

[1]GSA Data Repository item 2010277, Figures DR1–DR5 and Video DR1, is available online at www.geosociety.org/pubs/ft2010.htm, or on request from editing@geosociety.org or Documents Secretary, GSA, P.O. Box 9140, Boulder, CO 80301, USA.

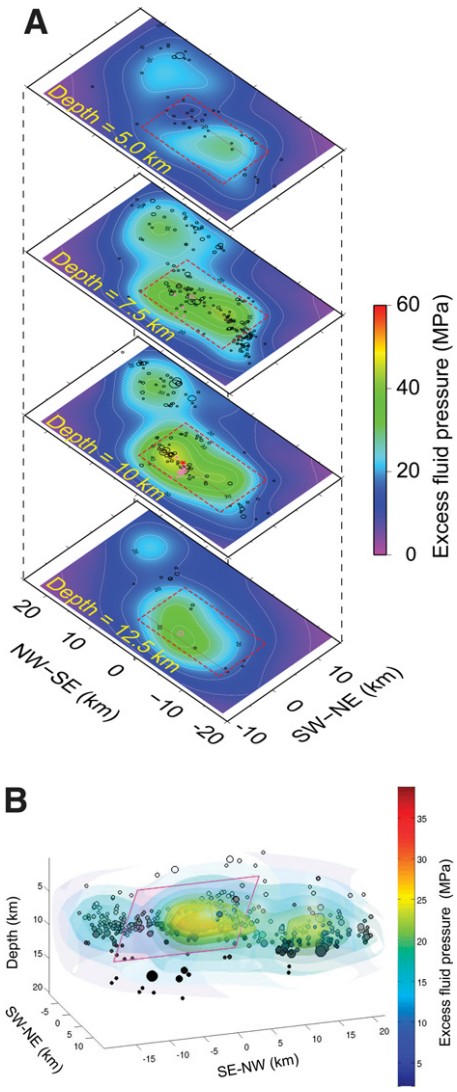

Figure 3. A: Map view of the excess fluid pressure distribution at depths of 5 km, 7.5 km, 10 km, and 12.5 km. All foreshocks and aftershocks (Chiarabba et al., 2009) with M ≥ 2.5 within 1 km of each plane (shown with pink and black circles, respectively) are superposed on the fluid pressure field. Red star indicates hypocenter of the main shock. Fault of the main shock (Cirella et al., 2009) is projected onto each plane. B: Three-dimensional image of the excess fluid pressure field with the hypocenters of foreshocks and aftershocks. View is from the northeast toward southwest.

fluid pressure field are an independent data set. A separate analysis where we chose the auxiliary plane instead of the true fault plane shows a much weaker visual correlation between aftershock locations and the mapped fluid pressure field (Fig. DR4). Interestingly, the foreshocks and the main shock are located in the region with the highest excess fluid pressure of 50 MPa (Figs. 3A and 3B) even though the average fluid pressure obtained through FMT is ~5 MPa above hydrostatic pressure (Fig. 2C). This is entirely consistent with a proposed poro-elastic model for the development of steeply dipping shear zones in response to poro-elastic stresses arising from an overpressured source at the base of an extensional system (Rozhko et al., 2007).

Figure 4A shows the excess fluid pressure distribution on the cross section (northeast-southwest) at the hypocenter of the main shock with the evolution of seismicity within 5 km of the plane. Foreshocks correlate with the highest fluid pressure (Fig. 4A-I), and most early aftershocks occurred at and around the high-pressure reservoir in the hanging wall (Fig. 4A-II). Subsequent events within one week of the main shock (Fig. 4A-III) appear to migrate upward along the main-shock fault and within the footwall.

Aside from narrow regions to the southeast of the fault strike, the change in Coulomb failure stress (ΔCFS) has little correlation with aftershock locations at individual depths (Fig. DR5), or in profile (Fig. 4B). The locations of early aftershocks appear to be related to regions of volumetric compression due to the main shock (Figs. 4B and DR5), indicating a mechanism where compression of high-fluid-pressure reservoirs initiates fluid flow toward dilatant zones (Nur and Booker, 1972). This increases the fluid pressure down-gradient and generates poro-elastic shear stresses in response to that flow (Nur and Booker, 1972; Bosl and Nur, 2002; Rozhko et al., 2007). The migration of seismicity along the main-shock fault (Fig. 4A-III) is consistent with the expectation from the fluid pressure diffusion model (Miller et al., 2004).

A SCENARIO FOR THE 2009 L'AQUILA EARTHQUAKE SEQUENCE

Our results lead to a scenario for the L'Aquila earthquake quite similar to that proposed for the 1997 Colfiorito sequence (Miller et al., 2004). A continuous supply of deeply derived CO_2 provides a source of high-pressure fluid to the region. In areas where diffuse degassing is observed, the CO_2 remains at hydrostatic pressure because of connectivity between the source and the free-surface boundary condition. Where CO_2 is supplied from below but cannot escape, fluid pressures build over the earthquake recurrence timescale. An analysis of the foreshock activity of this earthquake (Fig. 4A-I) shows evidence for invading high-pressure fluids near the hypocenter, which may have locally weakened the fault through the slow reduction (on the scale of months) of the effective normal stress acting on the fault plane. Such a high-pressure source at the base of the fault can initiate faulting on an optimally oriented fault (Rozhko et al., 2007), consistent with our result of a mildly overpressured main shock. Uranium anomalies prior to the L'Aquila earthquake, (Plastino et al., 2010), and changing Vp/Vs ratios prior to the earthquake (Di Luccio et al., 2010) are consistent with the scenario discussed here. In addition

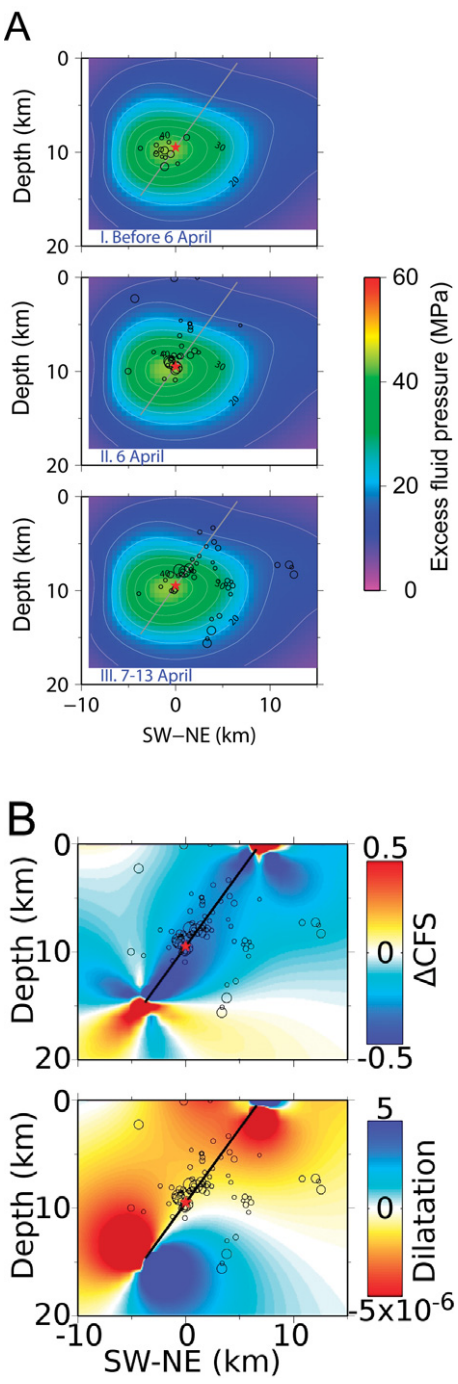

Figure 4. Evolution of seismicity, and static stress and strain changes due to the main shock on the cross section (NE-SW) at the hypocenter. A: Seismicity superposed on the estimated fluid pressure field (I) before main shock, (II) on 6 April, and (III) on 7–13 April. Events (M > 2.5) within 5 km of the cross section are plotted. B: ΔCFS (upper panel) and dilatation (lower panel) due to main shock, assuming 0.25 m uniform slip on the main-shock fault (Cirella et al., 2009) in an elastic halfspace. Plotted events are the same in A.

to other transient mechanisms such as dynamic triggering that are very effective in fluid-rich environments (Hill et al., 1993), the main shock volumetrically compressed the surrounding overpressured poro-elastic medium, initiating fluid flow. One possible explanation for the extensive aftershock activity is postseismic fluid flow triggered by perturbing an extensive and overpressured reservoir at depth. Importantly, since the main shock and each aftershock also correspond to the creation of a fresh fracture (Miller and Nur, 2000), the network has evolving hydraulic properties that significantly influence fluid flow and thus contribute to the complexity of this sequence.

This analysis provides important constraints on the shape and magnitude of the deep fluid pressure field, and therefore provides an important boundary condition for forward modeling and mechanistic hazard assessment. That both the Omori and Gutenberg-Richter laws are satisfied makes this sequence indistinguishable from other earthquake/aftershock sequences, suggesting that similar processes may be acting elsewhere.

ACKNOWLEDGMENTS

We thank Robert Herrmann for providing the focal mechanism data and Lauro Chiaraluce for discussions and for providing the relocated hypocenter data catalogue. This study was supported in part by DFG Project MI 1237/2-1.

REFERENCES CITED

Anzidei, M., Boschi, E., Cannelli, V., Devoti, R., Esposito, A., Galvani, A., Melini, D., Pietrantonio, G., Riguzzi, F., Sepe, V., and Serpelloni, E., 2009, Coseismic deformation of the destructive April 6, 2009 L'Aquila earthquake (central Italy) from GPS data: Geophysical Research Letters, v. 36, L17307, doi: 10.1029/2009GL039145.

Bosl, W.J., and Nur, A., 2002, Aftershocks and pore fluid diffusion following the 1992 Landers earthquake: Journal of Geophysical Research (Solid Earth), v. 107, 2366, doi: 10.1029/2001JB000155.

Bott, M.H.P., 1959, The mechanics of oblique slip faulting: Geological Magazine, v. 96, p. 109–117, doi: 10.1017/S0016756800059987.

Byerlee, J., 1978, Friction of rocks: Pure and Applied Geophysics, v. 116, p. 615–626, doi: 10.1007/BF00876528.

Chiarabba, C., and 29 others, 2009, The 2009 L'Aquila (central Italy) M_w 6.3 earthquake: Main shock and aftershocks: Geophysical Research Letters, v. 36, L18308, doi: 10.1029/2009GL039627.

Chiodini, G., Cardellini, C., Amato, A., Boschi, E., Caliro, S., Frondini, F., and Ventura, G., 2004, Carbon dioxide Earth degassing and seismogenesis in central and southern Italy: Geophysical Research Letters, v. 31, L07615, doi: 10.1029/2004GL019480.

Cirella, A., Piatanesi, A., Cocco, M., Tinti, E., Scognamiglio, L., Michelini, A., Lomax, A., and Boschi, E., 2009, Rupture history of the 2009 L'Aquila (Italy) earthquake from non-linear joint inversion of strong motion and GPS data: Geophysical Research Letters, v. 36, L19304, doi: 10.1029/2009GL039795.

Collettini, C., and Barchi, M.R., 2002, A low-angle normal fault in the Umbria region (Central Italy): A mechanical model for the related microseismicity: Tectonophysics, v. 359, p. 97–115, doi: 10.1016/S0040-1951(02)00441-9.

Connolly, J.A.D., 1997, Devolatilization-generated fluid pressure and deformation-propagated fluid flow during prograde regional metamorphism: Journal of Geophysical Research (Solid Earth), v. 102, p. 18,149–18,173, doi: 10.1029/97JB00731.

Cox, S.F., 1995, Faulting processes at high fluid pressures: An example of fault valve behavior from the Wattle Gully Fault, Victoria, Australia: Journal of Geophysical Research (Solid Earth), v. 100, p. 12,841–12,859, doi: 10.1029/95JB00915.

Di Luccio, F., Ventura, G., Di Giovambattista, R., Piscini, A. and Cinti, F.R., 2010, Normal faults and thrusts activated by deep fluids: The 6 April 2009 Mw 6.3 L'Aquila earthquake, Central Italy: Journal of Geophysical Research, doi:10.1029/2009JB007190.

Frezzotti, M.L., Peccerillo, A., and Panza, G., 2009, Carbonate metasomatism and CO_2 lithosphere-asthenosphere degassing beneath the Western Mediterranean: An integrated model arising from petrological and geophysical data: Chemical Geology, v. 262, p. 108–120, doi: 10.1016/j.chemgeo.2009.02.015.

Gephart, J.W., and Forsyth, D.W., 1984, An improved method for determining the regional stress tensor using earthquake focal mechanism data: Application to the San Fernando earthquake sequence: Journal of Geophysical Research, v. 89, p. 9305–9320, doi: 10.1029/JB089iB11p09305.

Hill, D.P., and 30 others, 1993, Seismicity remotely triggered by the magnitude 7.3 Landers, California, earthquake: Science, v. 260, p. 1617–1623, doi: 10.1126/science.260.5114.1617.

Kubo, A., and Fukuyama, E., 2004, Stress fields and fault reactivation angles of the 2000 western Tottori aftershocks and the 2001 northern Hyogo swarm in southwest Japan: Tectonophysics, v. 378, p. 223–239, doi: 10.1016/j.tecto.2003.09.009.

Michael, A.J., 1984, Determination of stress from slip data: Faults and folds: Journal of Geophysical Research, v. 89, p. 1517–1526, doi: 10.1029/JB089iB13p11517.

Michael, A.J., 1987, Use of focal mechanisms to determine stress: A control study: Journal of Geophysical Research (Solid Earth and Planets), v. 92, p. 357–368, doi: 10.1029/JB092iB01p00357.

Micklethwaite, S., and Cox, S.F., 2006, Progressive fault triggering and fluid flow in aftershock domains: Examples from mineralized Archaean fault systems: Earth and Planetary Science Letters, v. 250, p. 318–330, doi: 10.1016/j.epsl.2006.07.050.

Miller, S.A., and Nur, A., 2000, Permeability as a toggle switch in fluid-controlled crustal processes: Earth and Planetary Science Letters, v. 183, p. 133–146, doi: 10.1016/S0012-821X(00)00263-6.

Miller, S.A., Collettini, C., Chiaraluce, L., Cocco, M., Barchi, M., and Kaus, B.J.P., 2004, Aftershocks driven by a high-pressure CO_2 source at depth: Nature, v. 427, p. 724–727, doi: 10.1038/nature02251.

Nur, A., and Booker, J.R., 1972, Aftershocks caused by pore fluid flow?: Science, v. 175, p. 885–887, doi: 10.1126/science.175.4024.885.

Plastino, W., Povinec, P.P., De Luca, G., Doglioni, C., Nisi, S., Ioannucci, L., Balata, M., Laubenstein, M., Bella, F., and Coccia, E., 2010, Uranium groundwater anomalies and L'Aquila earthquake, 6th April 2009 (Italy): Journal of Environmental Radioactivity, v. 101, p. 45–50, doi: 10.1016/j.jenvrad.2009.08.009.

Rogie, J.D., Kerrick, D.M., Chiodini, G., and Frondini, F., 2000, Flux measurements of nonvolcanic CO_2 emission from some vents in central Italy: Journal of Geophysical Research (Solid Earth), v. 105, p. 8435–8445, doi: 10.1029/1999JB900430.

Rozhko, A.Y., Podladchikov, Y.Y., and Renard, F., 2007, Failure patterns caused by localized rise in pore-fluid overpressure and effective strength of rocks: Geophysical Research Letters, v. 34, L22304, doi: 10.1029/2007GL031696.

Sibson, R.H., 1990, Rupture nucleation on unfavorably oriented faults: Bulletin of the Seismological Society of America, v. 80, p. 1580–1604.

Sibson, R.H., 2000, Fluid involvement in normal faulting: Journal of Geodynamics, v. 29, p. 469–499, doi: 10.1016/S0264-3707(99)00042-3.

Wallace, R.E., 1951, Geometry of shearing stress and relation of faulting: Journal of Geology, v. 59, p. 118–130, doi: 10.1086/625831.

Walters, R.J., Elliott, J.R., D'Agostino, N., England, P.C., Hunstad, I., Jackson, J.A., Parsons, B., Phillips, R.J., and Roberts, G., 2009, The 2009 L'Aquila earthquake (central Italy): A source mechanism and implications for seismic hazard: Geophysical Research Letters, v. 36, L17312, doi: 10.1029/2009GL039337.

Yabuki, T., and Matsu'ura, M., 1992, Geodetic data inversion using a Bayesian information criterion for spatial distribution of fault slip: Geophysical Journal International, v. 109, p. 363–375, doi: 10.1111/j.1365-246X.1992.tb00102.x.

Manuscript received 8 June 2010
Revised manuscript received --
Manuscript accepted 15 June 2010

Printed in USA

Bibliography

Amelung, F., Yun, S., Walter, T., Segall, P., and Kim, S. (2007). Stress control of deep rift intrusion at Mauna Loa volcano, Hawaii. *Science*, 316, No.5827:1026.

Arthur, J., Dunstan, T., Al-Ani, Q., and Assadi, A. (1977). Plastic deformation and failure of granular media. *Geotechnique*, 27:53–74.

Audin, L., Avouac, J., Flouzat, M., and Plantet, J. (2002). Fluid-driven seismicity in a stable tectonic context: The Remiremont fault zone, Vosges, France. *Geophysical Research Letters*, 29, No.0:1091.

Backers, T. (2004). Fracture toughness determination and micromechanics of rock under mode i and mode ii loading. Technical report, Institut für Geowissenschaften. Mathematisch-Naturwissenschaftlichen Fakultät der Universität Potsdam.

Baisch, S., Vöorös, R., Rothert, E., Stang, H., Jung, R., and Schellschmidt, R. (2010). A numerical model for fluid injection induced seismicity at Soultz-sous-Forêts. *International Journal of Rock Mechanics and Mining Sciences*, 47:405–413.

Bardet, J. (1990). A comprehesive review of strain localization in elastoplastic soils. *Computers and Geotechnics*, 10:163–188.

Biot, M. (1941). General theory of three-dimensional consolidation. *Journal of Applied Physics*, 12:155–164.

Bols, W. and Nur, A. (2002). Aftershocks and pore fluid diffusion following the 1992 Landers earthquake. *Journal of Geophysical Research*, 107, no.B12, 2366:17–1,17–9.

Bond, R., Knupp, P., and Ober, C. (June, 2004). A manufactured solution for verifying CFD boundary conditions. In *Procs. 34th AIAA Fluid Dynamics Conference and Exhibit. Portland, Oregon*, pages AIAA. 2004–2629.

Cappa, F. and Rutqvist, J. (2011). Modeling of coupled deformation and permeability evolution during fault reactivation induced by deep underground injection of CO_2. *International Journal of Greenhouse Gas Control*, 5:336–346.

Cembrano, J. and Lara, L. (2009). The link between volcanism and tectonics in the southern volcanic zone of the Chilean Andes: A review. *Tectonophysics*, 471:96–113.

Chin, L., Raghavan, R., and Thomas, L. (2000). Fully coupled geomechanics and fluid-flow analysis of wells with stress-dependent permeability. *SPE Journal*, 5 No.1:32–457.

Cundall, P. (1982). Adaptive density scaling for time-explicit calculations. In *Procs. 4th. International Conference on Numerical Methods in Geomechanics. Edmonton, Canada*, volume 1, pages 23–26.

Darwin, C. (1840). On the connexion of certain volcanic phenomena in South America; and on the formation of mountain chains and volcanos, as the effect of the same powers by which continents are elevated. *Transactions of the Geological Society of London*, 5:601–631.

David, C., Wong, T., Zhu, W., and Zhang, J. (1994). Laboratory measurement of compaction-induced permeability change in porous rocks: Implications for the generation and maintenance of pore pressure excess in the crust. *Pure and Applied Geophysics*, 143, No.1-3:425–456.

Detournay, E. and Cheng, A. (1993). Fundamentals of poroelasticity. In J.A., H., editor, *Comprehensive rock engineering. Vol.2*, page 113–171. Pergamon.

Duffield, W. and Sass, J. (2003). Geothermal Energy- Clean Power from Earth's Heat. Technical Report C1249, U.S. Geological Survey.

Eggert, S. and Walter, T. (2009). Volcanic activity before and after large tectonic earthquakes: Observations and statistical significance. *Tectonophysics*, 471:14–26.

Famin, V., Nakashima, S., Boullier, A., Fujimoto, K., and Hirono, T. (2008). Earthquakes produce carbon dioxide in crustal faults. *Journal of Structural Geology*, 265:487–497.

Gassmann, F. (1951). Elasticity of porous media. *Vierteljahresschrift der Naturforschen den Gesselschaft 96, 1–23 (in German)*, 96:1–23.

Gerya, T. (2011). Future directions in subduction modeling. *Journal of Geodynamics*, 52:344– 378.

Glowacka, E., Gonzalez, J., and Fabriol, H. (1999). Recent vertical deformation in Mexicali valley and its relationship with tectonics, seismicity, and the exploitation of the Cerro Prieto geothermal field, Mexico. *Pure and applied geophysics*, 156:591–614.

Griebel, M. and Zaspel, P. (2010). A multi-GPU accelerated solver for the three-dimensional two-phase incompressible Navier-Stokes equations. *Computer Science- Reseach and Development*, 25:65–73.

Gutierrez, M., Øino, L., and Nygård, R. (2000). Stress-dependent permeability of a de-mineralised fracture in shale. *Marine and Petroleum Geology*, 17:895–907.

Guvanasem, V. and Chan, T. (April 10-14, 1995). A new three-dimesional finite-element analysis of hysteresis thermohydromechanical deformation of fractured rock mass with dilatance in fractures. In *Procs. of the second conference on Mechanics of jointed and faulted rocks. Vienna, Austria*, pages 347–442.

Hansen, D. (2003). A meshless formulation for geodynamic modelling. *Journal of Geophysical Research*, 108 No.B11:2549.

Häring, M., Schanz, U., Ladner, F., and Dyer, B. (2008). Characterisation of the Basel 1 enhanced geothermal system. *Geothermics*, 37:469–495.

Harris, M. and Buck, I. (2005). GPU flow control idioms. In *GPU Gems 2*, pages 547–555. Addison-Wesley.

Hill, D., Pollitz, F., and Newhall, C. (2002). Earthquake-volcano interactions. *Physics Today*, 55, No.11:41–47.

Jaeger, J., Cook, N., and Zimmerman, R. (2007). *Fundamentals of rock mechanics*. Blacwell Publishing, 4th, edition.

Johnson, J. and Satake, K. (1999). Asperity distribution of the 1952 great Kamchatka earthquake and its relation to future earthquake potential in Kamchatka. *Pure and Applied Geophysics*, 154, No.3-4:541–553.

Kaus, B. (2010). Factors that control the angle of shear bands in geodynamic numerical models of brittle deformation. *Tectonophysics*, 484, No.1-4:36–47.

Kaus, B., Gerya, T., and Schmid, D. (2008). Recent advances in computational geodynamics: Theory, numerics and applications. *Physics of the Earth and Planetary Interiors*, 171. No.1-4:2–6.

Kohl, T., Evans, K., Hopkirk, R., and Rybach, L. (1995). Coupled hydraulic, thermal and mechanical considerations for the simulation of hot dry rock reservoirs. *Geothermics*, 24, No.3:345–359.

Kolditz, O., Bauer, S., Bilke, L., Böttcher, N., Delfs, J., Fischer, T., Görke, U., Kalbacher, T., Kosakowski, G., McDermott, C., Park, C., Radu, F., Rink, K., Shao, H., Shao, H., Sun, F., Sun, Y., Singh, A., Taron, J., Walther, M., Wang, W., Watanabe, N., Wu, Y., Xie, M., and Zehner, B. OpenGeoSys: An open source initiative for numerical simulation of thermo-hydro-mechanical/chemical (THM/C) processes in porous media, environmental earth sciences. Enviromental Earth Science.

Kolditz, O. and Chen, C. (2005). Geosys/RockFlow – Tutorial i 2D Groundwater Modeling. Technical report, GeoSys.

Koyama, M. (2002). Mechanical coupling between volcanic unrests and large earthquakes: A review of examples and mechanisms. *Journal of Geography*, 111, No.2:222–232.

Lara, L., Naranjo, J., Moreno, H., and Schellart, W. (2004). Rhyodacitic fissure eruption in Southern Andes (Cordón Caulle; 40.58s) after the 1960 (Mw:9.5). Chilean earthquake: a structural interpretation. *Journal of Volcanology and Geothermal Research*, 138:127–138.

Lastra, M., Mantas, J., Urena, C., Castro, M., and García-Rodríguez, J. (2009). Simulation of shallow-water systems using graphics processing units. *Mathematics and Computers in Simulation*, 182:598–618.

Lockner, D. and Byerlee, J. (1977). Hydrofracture in Weber sandstone at high confining pressure and differential stress. *Journal of Geophysical Research*, 82, No.14:2018–2026.

Lupi, M., Geiger, S., and Graham, C. (2011). Numerical simulations of seismicity-induced fluid flow in the Tjörnes fracture zone, Iceland. *Journal of Geophysical Research*, 116:B07101.

Madariaga, R. (2007). Slippery when hot. *Science*, 316, No.5826:842–843.

Maillot, B., Nielsen, S., and Main, I. (1999). Numerical simulation of seismicity due to fluid injection in a brittle poroelastic medium. *Geophysical Journal International*, 139:263–272.

Majer, E., Baria, R., Stark, M., Oates, S., Bommere, J., Smith, B., and Asanuma, H. (2007). Induced seismicity associated with enhanced geothermal systems. *Geothermics*, 36:185–222.

Manga, M. and Brodsky, E. (2006). Seismic triggering of eruptions in the far field: Volcanoes and geysers. *Annual Review of Earth and Planetary Sciences*, 34:263–291.

Mayr, S., Stanchits, S., Langenbruch, C., Dresen, G., and Shapiro, S. (2011). Acoustic emission induced by pore-pressure changes in sandstone samples. *Geophysics*, 76:MA21–MA32.

Michéa, D. and Komatitsch, D. (2010). Accelerating a three-dimensional finite-difference wave propagation code using GPU graphics cards. *Geophysics Journal International*, 182:389–402.

Miller, S., Collettini, C., Chiaraluce, L., Cocco, M., Barchi, M., and Kaus, B. (2004). Aftershocks driven by a highpressure CO_2 source at depth. *Nature*, 427:724–727.

Miller, S. and Nur, A. (2000). Permeability as a toggle switch in £uid-controlled crustal processes. *Earth and Planetary Science Letters*, 183:133–146.

Mitchell, T. and Faulkner, D. (2008). Experimental measurements of permeability evolution during triaxial compression of initially intact crystalline rocks and implications for fluid flow in fault zones. *Journal of Geophysical Research-Solid Earth*, 113:B11412.

Moreno, M., Rosenau, M., and Oncken, O. (2010). 2010 maule earthquake slip correlates with pre-seismic locking of andean subduction zone. *Nature*, 467:198–202.

Nageswarana, J., Dutt, N., Krichmar, J., Nicolau, A., and Veidenbaum, A. (2009). A configurable simulation environment for the efficient simulation of large-scale spiking neural networks on graphics processors. *Neural Networks*, 22:791–800.

Nercessian, A., Hirn, A., , and Sapin, M. (1991). A correlation between earthquakes and eruptive phases at Mt. Etna: an example and past occurrences. *Geophysical Journal International*, 105, No.1:131–138.

Nostro, C., Stein, R., Cocco, M., Belardinelli, M., , and Marzocchi, W. (1998). Two-way coupling between Vesuvius eruptions and Southern Apennine earthquakes, italy, by elastic stress transfer. *Journal of geophysical research*, 103, No.24:487–24.

Nur, A. (1971). Effects of stress on velocity anisotropy in rocks with cracks. *Journal of Geophysical Research*, 76 No.8:2022–2034.

NVIDIA (2011). *NVIDIA CUDA C Programming Guide Version 4.0, NVIDIA Corporation*.

Ohtake, M. (1974). Seismic activity induced by water injection at Matsushiro, Japan. *Journal of Physics of the Earth*, 22:163–176.

Paola, N. D., Hirose, T., Mitchell, T., Toro, G. D., Viti, C., and Shimamoto, T. (2011). Fault lubrication and earthquake propagation in thermally unstable rocks. *Geology*, 39, No.1316:35–38.

Phillips, W. S., Rutgledge, J., House, L., and Fehler, C. (2002). Induced microearthquake patterns in hydrocarbon and geothermal reservoirs: Six case studies. *Pure and Applied geophysics*, 159:345–369.

Poliakov, A., Herrmann, H., and Podladchikov, Y. (1994). Fractal plastic shear bands. *Fractals*, 2:567–581.

Popov, A. and Sobolev, S. (2008). SLIM3D: A tool for three-dimensional thermomechanical modeling of lithospheric deformation with elasto-visco-plastic rheology. *Physics of the Earth and Planetary Interiors*, 171:55–75.

Rice, J. (1992). Fault stress states, pore pressure distributions, and the weakness of the San Andreas fault. In *Fault Mechanics and Transport Properties in Rocks (eds. B. Evans and T.-F. Wong)*, pages 475–503. Academic Press.

Roy, C., Nelson, C., Smith, T., and Ober, C. (2004). Verification of Euler/-Navier–Stokes codes using the method of manufactured solutions. *International Journal for Numerical Methods in Fluids*, 44:599–620.

Rozhko, A., Podladchikov, Y., and Renard, F. (2007). Failure patterns caused by localized rise in pore-fluid overpressure and effective strength of rocks. *Geophysical Research Letters*, 34:L22304.

Rutqvist, J. (2011). Status of the TOUGH-FLAC simulator and recent applications related to coupled fluid flow and crustal deformations. *Computers and Geociences*, 37:739–750.

Rutqvist, J., Birkholzer, J., Cappa, F., and Tsang, C. (2007). Estimating maximum sustainable injection pressure during geological sequestration of CO_2 using coupled fluid flow and geomechanical fault-slip analysis. *Energy Conversion and Management*, 48:1798–1807.

Rutqvist, J., Birkholzer, J., and Tsang, C. (2008). Coupled reservoir–geomechanical analysis of the potential for tensile and shear failure associated with CO_2 injection in multilayered reservoir–caprock systems. *International Journal of Rock Mechanics and Mining Sciences*, 45:132–143.

Rutqvist, J. and Tsang, C.-F. (13-15 October, 2003). A fully coupled three-dimensional THM analysis of the FEBEX in situ test with the rocmas code: Prediction of THM behavior in a bentonite barrier. In *Conference: GEOPROC 2003 , Stockholm (SE),*.

Salari, K. and Knupp, P. (2000). Code verification by the method of manofactured solutions. Technical Report SAND2000-1444, Sandia National Laboratories.

Sanchez, J. and McNutt, S. (2004). Intermediate-term declines in seismicity at mt. wrangell and mt. veniaminof volcanoes, Alaska, following the 3 november 2002 m_w 7.9 Denali fault earthquake. *Bulletin of the Seismological Society of America*, 94, No.6B:S370.

SEO20011 (2011). `http://supersites.earthobservations.org/chile.php`.

Shapiro, S. and Dinske, C. (2009). Fluid-induced seismicity: Pressure diffusion and hydraulic fracturing. *Geophysical Prospecting*, 57:301–310.

Shapiro, S., Kummerow, J., Dinske, C., Asch, G., Rothert, E., Erzinger, J., Kümpel, H.-J., and Kind, R. (2006). Fluid induced seismicity guided by a continental fault: Injection experiment of 2004/2005 at the German Deep Drilling Site (KTB). *Geophysical Research Letters*, 33:L01309.

Sharp, A., Lombardo, G., and Davis, P. M. . (1981). Correlation between eruptions of Mount Etna, Sicily, and regional earthquakes as seen in historical records from AD 1582. *Transactions of the Geological Society of London*, 65:507–523.

Shunn, L. and Ham, F. (2007). Method of manufactured solutions applied to variable-density flow solvers. Technical report, Center for Turbulence Research Annual Research Briefs 2007.

Sibson, R. (2007). An episode of fault-valve behavior during compressional inversion? The 2004 MJ 6.9 Mid-Niigata Prefecture, Japan, earthquake. *Earth and Planetary Science Letters*, 257:188–199.

Sorensen, T. and Mosegaard, J. (2006). Haptic feedback for the GPU-based surgical simulator. *Medicine Meets Virtual Reality*, 14:523–528.

Sparks, S. and Sigurdsson, H. (1977). Magma mixing: a mechanism for triggering acid explosive eruptions. *Nature*, 267:315–318.

Stanchits, S., Mayr, S., Shapiro, S., and Dresen, G. (2011). Fracturing of porous rock induced by fluid injection. *Tectonophysics*, 503:129–145.

Stivala, A., Stuckey, P., and Wirth, A. (2010). Fast and accurate protein substructure searching with simulated annealing and GPUs. *BMC Bioinformatics*, 11:446.

Taron, J. and Elsworth, D. (2010). Coupled mechanical and chemical processes in engineered geothermal reservoirs with dynamic permeability. *International Journal of Rock Mechanics and Mining Sciences*, 47:1339–1348.

Taron, J., Elsworth, D., and Min, K. (2009). Numerical simulation of thermal-hydrologic-mechanical-chemical processes in deformable, fractured porous media. *International Journal of Rock Mechanics and Mining Sciences*, 46:842–854.

Terakawa, T., Miller, S., and Deichmann, N. (2012). High fluid pressure and triggered earthquakes in the enhanced geothermal system in Basel, Switzerland. In preparation.

Terakawa, T., Zoporowski, A., Galvan, B., and Miller, S. (2010). High-pressure fluid at hypocentral depths in the L'Aquila region inferred from earthquake focal mechanisms. *Geology*, 38, no.11:995–998.

Terzaghi, K. (1923). Die berechnung des durchlassigkeitsziffer des tones aus dem verlauf der hydrodynamischen spannungserscheinungen. *Sitz. Akad. Wiss. Wien, Abt. IIa*, 132:125–138.

Toda, S., Stein, R., Richards-Dinger, K., , and Bozkurt, S. (2005). Forecasting the evolution of seismicity in Southern California: Animations built on earthquake stress transfer. *Journal of Geophysical Research*, 110, No.10:1029.

U.S.D.E (2008). An evaluation of Enhanced Geothermal Systems technology, Geothermal Technologies Program. Technical report, U.S. Department of Energy.

USGS (2010). Technical report, 2010. Technical report, US Geological Survey.

Vermeer, P. and Borst, R. (1984). Non-associative plasticity for soils, concrete and rock. Technical report, Heron.

Vigny, C. (2011). The 2010 mw 8.8 maule megathrust earthquake of central chile, monitored by gps. *Science*, 332:1417.

Vogt, L., Olivares-Amaya, R., Kermes, S., Shao, Y., Amador-Bedolla, C., and Aspuru-Guzik, A. (2008). Accelerating resolution-of-the-identity second-order Møller-Plesset quantum chemistry calculations with graphical processing units. *Journal of Physical Chemistry*, 112:2049–2057.

Walter, T. (2007). How a tectonic earthquake may wake up volcanoes: Stress transfer during the 1996 earthquake–eruption sequence at the Karymsky Volcanic Group, Kamchatka. *Earth and Planetary Science Letters*, 264:347–359.

Walter, T. and Amelung, F. (2007). Volcanic eruptions following M $\geq$ 9 megathrust earthquakes: Implications for the Sumatra-Andaman volcanoes. *Geology*, 35:539–542.

Wang, W. and Kolditz, O. (2007). Object-oriented finite element analysis of thermo-hydro-mechanical (THM) problems in porous media. *International Journal for Numerical Methods in Engineering*, 69, No.1:162–201.

Wong, T., Ko, S.-C., and Olgaard, D. (1997). Generation and maintenance of pore pressure excess in a dehydrating system, 2, Theorical analysis. *Journal of Geophysical Research*, 102:841–852.

Xu, T., Sonnenthal, E., Spycher, N., and Pruess, K. (2006). TOUGHREACT- a simulation program for non-isothermal multiphase reactive geochemical transport in variably saturated geologic media: Applications to geothermal injectivity and CO_2 geological sequestration. *Computers and Geosciences*, 32:145–146.

Yang, J., Wang, Y., and Chen, Y. (2007). GPU accelerated molecular dynamics simulation of thermal conductivities. *Journal of Computational Physics*, 221:799–804.

Zang, A., Wagner, C., and Dresen, G. (1996). Acoustic emission, microstructure, and damage model of dry and wet sandstones stressed to failure. *Journal of Geophysical Research*, 101, No. B8:17,507–17,521.

Zaspel, P. and Griebel, M. (2011). Solving incompressible two-phase flows on massively parallel multi-GPU clusters. *Computers and Fluids*, Submitted:INS Preprint no.1113.

Zhang, S., Tullis, T., and Scruggs, V. (1999). Permeability anisotropy and pressure dependency of permeability in experimentally sheared gouge materials. *Earth and Planetary Science Letters*, 21:795–806.

List of Figures

1.1 Mohr-Coulomb diagram. The blue line represent the Mohr-Coulomb failure envelop (shear failure). Green line is the Griffith cut off (tensile failure). (a) Homogeneous fluid pressure decreases the normal stress, moving the circle from initial position *I* to failure position *II*. (b) Localized pore fluid pressure changes the radius of the Mohr circle while shifting it near to the failure surface (position II). Lower pore fluid pressures might cause failure. 15

1.2 CPU architecture is designed for serial computations. For this reason it dedicates more chip space to flow control and memory operations. GPUS architecture gives priority to arithmetic intensive operations. Much more Arithmetic Logic Units (ALUs) are build in GPU chips.Cache memory for memory operations and flow control units are limited causing GPUs to be inefficient in comparison to CPUs for serial processes. From (NVIDIA, 2011). 17

1.3 Comparison of the floating point operations (FLOPs) per second and memory band width for GPUs and CPUs. From (NVIDIA, 2011) . . 18

1.4 Every thread (yellow rectangles) has it own local (red squares). A warp is a set of 32 threads. All threads within a warp execute the same commands. Warp are grouped in Blocks. All threads of the same block have access to a common fast cached shared memory. All threads, independently of their block, have simultaneous access to global memory. 20

2.1 Initial data matrices (a) of size $nx \times nz$, are grouped together in large one dimensional vectors (b) of size *number of matrices* $\cdot nz \cdot nx$ to be passed to GPU. 29

2.2 $log_{10}(L_2)$ vs. grid points per axis. Numerical resolution is grid points per axis squared, i.e. $nx = nz$. L_2 error norm decrease when the number of grid points is increased. GPU results correspond to CPU ones. 33

2.3 Second invariant of strain tensor (si) showing shear bands formation and dip angles θ for elasto-plastic media under compression with internal frictional angles (a) $\varphi = 20°$, (b) $\varphi = 30°$ and (c)$\varphi = 40°$. For all numerical experiments dilation angle was set equal to zero, $\psi = 0$. Pink lines are the Coulomb angles and green lines are Rosco angles. In all cases θ is very close to the Coulomb value. Numerical resolution: 300×300. 34

2.4 Shear band formation and dip angles θ for elasto-plastic media under extension cases. Dilation angle $\psi = 0$ and frictional angles (a) $\varphi = 20°$, (b) $\varphi = 30°$ and (c)$\varphi = 40°$. For all cases, dip angle θ lays between Roscoe (green line) and Coulomb (pink line) angles. In the upper part of the domain tensile fracturing is appreciated. Numerical resolution: 300×300. 35

2.5 Permeability (a), yield function (b) and fluid pressure profile (c), (d), (e) at time =30, 60 and 180 days after the diffusion release for the compressional case. Numerical resolution: 300×300, 33m. Maximum values of the fractures permeability is around $1e^{-8}$ m/s^2 in the overpressurized layer. However, permeability drops in the hydrostatic layer locking the fluid pressure. Even for high permeabilities in the overpressurized part, the contrast of the permeability between the overpressurized layer at the bottom and the hydrostatic layer produces "lock up" of the fluids. Yield function (b) shows the closeness to failure (dark red). Fractures are critically stressed and about to fail. High resolution allows development of complex fracture networks with damage zone surrounding the main faults. 37

2.6 Permeability (a) and yield function (b) and fluid pressure profiles (c) ,(d),(e) at time=30, 90 and 180 days after the diffusion release for the extensional case. Numerical resolution: 300×300, 33m. Beside shear bands, non-localized tensile fractures can be appreciated. Extension enhance fluid pressure migration through the fractures on the hydrostatic pressurized layer. Large damage zones are appreciated developing from the edges of the domain. The reason of these damage is the fast extensional velocity applied during the fracture creation time. Tensile failure, vertical faults, are present in the overpressurized and the hydropressurized sections of the domain. 38

3.1 Setup for numerical hydrofracture experiments. Confining stress is set at 50 MPa for both numerical experiments. The borehole in numerical experiment NFb20 is designated by the white lines. Axial stress for NFb20=261.31 MPa and pore fluid pressure P_f=5 MPa. For numerical experiment NFb24: axial stress was 266.166 MPa and fluid injection pressure P_f=5.5 MPa. Samples are considered frictionless at the top and bottom edges and at left and right edges are free to deform. 47

3.2 Results of the numerical experiment NFb24 with fracture permeability one order of magnitude higher than background permeability. First row shows the yield function or closeness to failure. Failure occurs at yield function=0. Black dots are the acoustic emissions (AE's). Second row is the pore fluid pressure profile. At time=30 s , AE's (black dots) of microcracks formation (a). At time=240-360 s shear cracks develop and AE's occur around them (b)-(c). After 500 s there is no total failure but 5 long cracks are appreciable(d). 49

3.3 Numerical experiment NFb24 with fracture permeability two order of magnitude higher than background permeability. At time= 30s microcracks develop in the sample . At time=240 s a clear long fracture and three small fractures developed . Total failure of the sample occurred at approximately 360 seconds after injection is started 50

3.4 Numerical experiment NFb20. Fracture permeability two orders of magnitude higher that background permeability. tensile fractures develop from the walls of the borehole (a). At time=240 s a clear shear fracture develop from the top of the borehole (b). Different secondary fractures can be appreciated at time=360 s (c). These fractures develop form the walls of the borehole and the corners of the sample. The sample fails at between time=420-500 s (d). For comparison (e) shows the final state of the laboratory sample. From (Stanchits et al., 2011). 51

4.1 Evolution of the fracture network and final stress states. X and Z axis in meters. Resolution 500×500, 1cm. Upper row presents the yield function or closeness to failure (dark red is closer to failure). Black dots represent failing points at snapshot time. We relate these failing points to seismic events. White circle represents the borehole position. Figures (a), (b) and (c) presents initial, intermediate and final state of the network during stress relaxation time. Activation of different fractures can be observed. In figure (a) activation of a non-optimal oriented fracture due to heterogeneity is appreciated at the top left side of the borehole. In figure (a) and (a) this fracture deactivates and new optimally oriented fractures are responsible for the deformation. Highly damaged zone appears between close adjacent fractures. Figures (d), (e) and (f) presents the final state of the stresses σ_{xx}, σ_{zz} and σ_{xz} respectively (here x is the direction of the principal horizontal stress σ_H and horizontal to the reader and z is the directions of the minimum horizontal stress σ_h and vertical to the reader). Compression was take as negative. The final stress fields are very inhomogeneous but their overall mean values are close to the initial stress states. Localized stressed points with very high compressive or extensive stresses can be appreciated. 61

4.2 Fluid injection pressure (P_f), permeability (κ) and yield function (F)for fluid injection in fractured rock. X and Z axis in meters. Snapshot at 10, 30, 50, 70 and 99 MPa injection fluid pressure are presented. At 10 and 30 MPa fluid flow occurs mainly through the adjacent fractures. At 50 MPa, 50% of the initial value of σ_h, hydrofracturing near to the borehole can be appreciated. The damage zone increases the permeability near to the borehole. At lower injection pressures (10 and 30 MPa) the seismic events are more distributed over the whole domain. Many unconnected events occurs within and outside the fractures. At high injection pressures, seismic events circumscribe mainly to the fractures. This can be interpreted as shear failure of the fractures. 62

4.3 Stress state at 10, 30, 50, 70 and 99 MPa fluid injection pressure.X and Z axis in meters. First row is the stress in the direction of the maximum horizontal stress, σ_{xx}, second row is the stress in the direction of the minimum horizontal stress σ_{zz} and third row is the shear stress σ_{xz}. 63

4.4 hola. 65

5.1 Geodynamic setting of Chile between 32°S and 40°S. The colour bar indicates the magnitude of the slip of the Maule earthquake and the arrow shows the subduction direction of the Nazca plate underneath the South American plate. The epicenter of the M8.8 Maule earthquake was located along the plate interface offshore of the Maule region (35.909°S, 72.733°W, 35 km depth) (USGS, 2010). The rupture exceeded 100 km in width and spread northwards and southwards simultaneously for more than 500 km. The maximum slip along the fault was as large as 9 m. The triangles mark the position of volcanic systems and the blue square indicate the reference point for the surface GPS velocities. Reverse, strike slip and ancient (inherited) faults are marked by jagged, solid, and dashed lines, respectively. 70

5.2 Conceptual model (not to scale) of the simulation cycle. First, second, and third row show the inter-seismic, co-seismic, and post-seismic state, respectively, undergone by the upper crust of the South American plate over approximately two centuries. The squares in the left column represent the region of continental crust simulated in this study. K_v indicates the increase or decrease of permeability throughout the simulations. The vertical line of circles indicates that the right boundary is fixed while the left black arrows on the left boundary indicate whether the system is in compression or extension. The length of the arrow is proportional to the GPS surface velocities. . . . 72

5.3 Yield function F, seismic events and stress tensor at the initial, intermediate and final stage or the relaxation time. Yield fundtion F represent the clossnes to failure. Failure occurs when F=0 (dark red is closer to failure). Black dots represent the failing point at snapshot time. Creation of new fractures can be appreciated. Second, third and fourth row represent the stresses in the horizontal direction (σ_{xx}), vertical direction (σ_{zz}) and shear stress (σ_{xz}). Stress relaxation can be appreciated. The complex fracture networks create areas with high localized stresses in the verge of failure. The dark red layer at the bottom represent the overpressurized fluids at lihostatic pressure in the lower crust. 74
5.4 compression 75
5.5 earthquake 76
5.6 extension 77

List of Tables and Listings

2.1 Model parameters 36

3.1 Model parameters for numerical experiments. Young's modulus are the same as in (Stanchits et al., 2011). Drained Poisson's ratio for Flechtingen sandstone is taken from (Backers, 2004). Undrained parameters are taken form Ruhr sandstone (Jaeger et al., 2007). The drained parameter of Ruhr and Flechtingen sandstones are very similar to each other. We introduce an undrained porosity ϕ_u to account for expansion of the pores and changes due to fracturing. Flechtingen sandstone tensile strength $\sigma_t = 6$ MPa. Cohesion was set to 20 MPa . 46

4.1 Parameters, symbols, values and units used for the numerical models. Taken from (Jaeger et al., 2007) and (Miller et al., 2004) 59

Acknowledgments

Ok, now is the moment to thank everybody. Thank you everybody.

Publikationen

Terakawa, T., Zoporowski, A., Galvan, B., Miller, S.A., 2010. High-pressure fluid at hypocentral depths in the L'Aquila region inferred from earthquake focal mechanisms. Geology 38(11), 995-998, doi:10.1130/G31457.1.

Galvan B. Simulation of Nonlinear Excitable Media with Cellular Nonlinear Networks. Diplom Arbeit. Universität Bonn
Galvan B. The Theory of Relativity Like Theory of the Absolutism of Physics Laws. Bachelor Arbeit. Universidad de Panama
Galvan B. Some Electromagnetic Properties of the Complex Scalar Field. Bachelor Arbeit. Universidad de Panama